

Measurement Techniques for Transfer Lines and Beam Instrumentation

P. Forck

GSI Helmholtz-Zentrum für Schwerionenforschung, Darmstadt, Germany

Abstract

The determination of beam parameters is essential for the operation and development of any accelerator facility. The working principle of beam instrumentation for electron and proton beams, with a focus on transfer line diagnostics and for injection and extraction matching, is discussed. This comprises beam instrumentation for beam current determination, beam loss monitors, methods for transverse profile and emittance diagnostics, and the usage of beam position monitors for bunched beams. Some examples of such measurements are also presented.

Keywords

Beam instrumentation; transformer; profile and position monitor; emittance.

1 Demands for beam diagnostics

Beam diagnostics form an essential constituent of any accelerator, as they make up the sensory organ showing the properties and the behaviour of the beam. Beam diagnostics deals with the real beam, including all possible imperfections of a real technical installation. There is a very wide range of diagnostic applications, resulting in quite different demands for the beam instruments and the related display of the measurement results.

- Reliable, quick measurements to determine the basic parameters of a machine setting are used as a fast check of the general functionality of the accelerator. The readings from the instrumentation give a single number or simple plots. These devices should be non-destructive for the beam, yielding online information. A prominent example is current measurement by a current transformer, as discussed in Section 2.
- Instruments are installed for a daily check of performance and stability, or for the control of wanted parameter changes in the accelerator setting. They are also used for solving simpler machine problems in the case of any device malfunction. An example is transverse profile determination, in most cases performed by a destructive device, as discussed in Section 4.
- Complex instrumentation for the commissioning of a new accelerator component, for the development of higher performance, and for solving more serious problems in the case of a malfunction must be available. The devices can be more complex to use and might be destructive for the beam. The importance is the creation of reliable information about the complex beam behaviour, allowing a clear interpretation. The determination of beam emittance is an important example, as discussed in Section 5.
- An additional application is the active control of device settings after the detection of the beam's properties, where the beam instrumentation serves as the sensor. This is generally called feedback of a given parameter to yield improved beam delivery. An example is reading of the beam position inside a synchrotron and correction of the orbit to its nominal value. A second example is determination of the beam current for slow extraction followed by active control of the extraction parameters to achieve current values as close as possible to a set value.

There is a large variety of beam parameters to be measured. For good alignment of the beam, all relevant parameters should be controllable. In this contribution, we focus on the instrumentation of

transfer lines and instrumentation within a synchrotron to determine injection and extraction parameters. Some parameters are controlled at transfer lines, but the results of such manipulations are better determined within the synchrotron. Moreover, relevant measurements are shown to describe the possibilities, limitations, and data quality delivered by the instruments. For general articles and books on beam diagnostics, see Refs. [1–7].

Most of the examples originate from the GSI facility, because the author is most familiar with these realizations. This does not mean that GSI has the most advanced systems; at other facilities, better installations might exist. The GSI accelerator facility consists of two pulsed linacs running at 36 MHz and 108 MHz, respectively, to accelerate all ions from different ion sources up to 18 MeV/u, corresponding to a velocity of $\beta = v/c = 0.19$. This energy is well above the so-called Coulomb barrier, where nuclear reactions are possible and performed at fixed targets. To achieve higher energies, up to 2 GeV/u, corresponding to $\beta = 0.95$, a synchrotron with 218 m circumference is used. The beam can be transferred to a storage ring with a single-bunch transfer (so-called fast extraction). Alternatively, it can be sent to fixed-target experiments using slow extraction, lasting from 1 to 10 s. The scientific investigations at these targets are related to nuclear, atomic, or plasma physics, as well as human cancer therapy.

The outline of this contribution is oriented on beam quantities. First, measurement of beam current at transfer lines for pulsed or slowly extracted beams and within a synchrotron is discussed. Section 3 deals with determination of beam losses; this can be used for alignment, because the fraction of beam that is lost can sometimes be determined more sensitively than the transmitted current. Moreover, the signal from such beam loss monitors can serve as an interlock generation in the case of device malfunction. Section 4 describes several methods for transverse profile measurements. There are methods that can be operated for all beams, but also quite different methods are used for electrons (which are, in most cases, relativistic) and protons (which require a large facility to reach relativistic velocities). Some of these methods are destructive for the beam and cannot, therefore, be applied at a synchrotron to monitor the beam properties of the circulating beam. Section 5 deals with the determination of transverse emittance in transfer lines, where the statistical description of the ensemble of beam particles is relevant. Section 6 describes very frequently used beam position monitors that determine the transverse centre of mass of a bunched beam. In nearly all facilities, these instruments are used for steering, focusing, and matching alignment at transfer lines and synchrotrons. Section 7 deals with the determination of longitudinal parameters, such as average beam energy, longitudinal bunch profile, and phase space distribution. Different devices are used as required for the quite different bunch lengths at electron and proton facilities.

The special beam instrumentation required for a linac-based fourth-generation light source with free electron laser application is not discussed in this contribution. Those accelerators are operated with very short bunches (down to the femtosecond range) and sometimes short beam pulses (down to single-bunch operation), as well as very high demands in terms of resolution and reproducibility; design considerations and recent achievements are discussed in e.g., Refs. [8–10], and references therein. Moreover, diagnostics for the novel laser-based plasma wakefield accelerators for electrons or ions are not covered; owing to their different installation schemes and related beam parameters, the instrumentation is partly based on modified methods to cover a very large dynamic range.

2 Measurement of beam current

The total electrical current is one of the most important parameters for the operation of a particle accelerator. In the daily operation of almost all accelerator laboratories, a first check concerns the current; in most cases, it is measured using a beam current transformer. Several types of current transformer are available to determine the current at electron and proton linacs and synchrotrons, even for short pulses, such as the transfer between synchrotrons, as well as for de-bunched beams, such as in a storage ring. These devices are commercially available [11], even though quite different types are used; a general overview of current measurement devices is presented in Ref. [12]. Current transformers are generally non-intercepting devices. Their principle is the detection of the magnetic field carried by the beam. For

currents below about 1 μA , transformers cannot be used, owing to noise limitations.

From the first days of accelerators, Faraday cups were used. The cup gives a direct measurement of the particle beam's charge because the particles are stopped in the cup. For large currents, this destructive method cannot be applied, because the total energy carried by the beam can destroy the intercepting material. For higher energetic particles, with energies above some 100 MeV/u for ions, the penetration depth reaches more than several centimetres and Faraday cups are no longer useful.

For low currents but higher energies, above about 100 MeV/u for ions, particles detectors are used. Here, the energy loss of the charged particle travelling through matter is detected. Either the particles are counted directly or the particle flux can be calculated with the help of a calibration. For most parameters, this is an intercepting method. Slow extraction from a synchrotron within a typical duration of some seconds is an example for such beam parameters.

Pulsed linacs or pulsed cyclotrons can be used as an injector to a synchrotron, where only a typical pulse length of 100 μs is needed for a multiturn injection. For a single-turn injection, the time is of the order of 1–10 μs . For other applications, such as atomic or nuclear physics, a continuous wave accelerator is used. Here, the bunches are delivered for an 'infinitely' long time, but the bunch structure still remains, owing to the RF acceleration by a linac or a cyclotron. There also exist types of accelerator that do not produce bunched beams, examples are the van de Graaff and Cockcroft–Walton types, based on electrostatic acceleration.

2.1 Current transformer for pulsed beams

2.1.1 General considerations and passive or fast current transformer

In an accelerator, the current is formed by N_{part} particles of charge state q per unit of time t or unit of length l and velocity $\beta = v/c$. The electrical current passing a given location is

$$I_{\text{beam}} = \frac{qeN_{\text{part}}}{t} = \frac{qeN_{\text{part}}}{l} \cdot \beta c, \quad (1)$$

where e is the elementary charge. The magnetic field B of a current can be calculated according to the Biot–Savart law

$$d\vec{B}(\vec{r}) = \mu_0 I_{\text{beam}} \cdot \frac{d\vec{l} \times \vec{r}}{4\pi r^3}, \quad (2)$$

where $\mu_0 = 4\pi \times 10^{-7}$ Vs/Am is the permeability of the vacuum, $d\vec{l}$ is the length in the direction of the beam and \vec{r} is the distance between the centre of the beam and the location of the field determination. Owing to the cylindrical symmetry outside of the beam, only the azimuthal component has to be considered along the unitary vector \vec{e}_φ , as shown in Fig. 1:

$$\vec{B} = \mu_0 \frac{I_{\text{beam}}}{2\pi r} \cdot \vec{e}_\varphi. \quad (3)$$

For a beam current of 1 μA and a distance of 10 cm, the magnetic field has a value of only 2 pT. To put this into perspective, the Earth's constant and homogeneous magnetic field has a value of about 50 μT .

The beam current can be determined by monitoring the accompanied magnetic field with a current transformer, as shown schematically in Fig. 2. The beam passes through a highly permeable torus as the 'primary winding'. An insulated wire, wound around the torus with N turns, serves as the 'secondary winding' of the transformer, with inductance L . The inductance L for a torus material of length l in the beam direction, inner radius r_i and outer radius r_o having a relative permeability μ_r and N windings is given by

$$L = \frac{\mu_0 \mu_r}{2\pi} \cdot l N^2 \cdot \ln \frac{r_o}{r_i}. \quad (4)$$

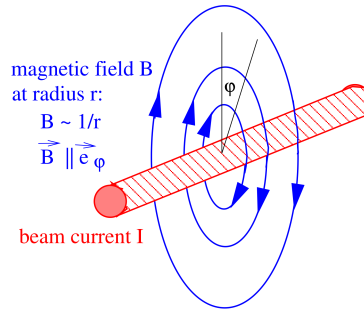


Fig. 1: Magnetic field of a current

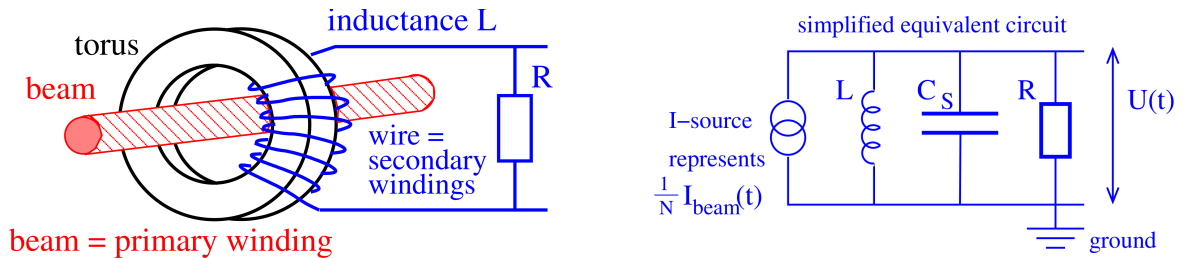


Fig. 2: Left: Scheme of a current transformer built as a ring-core (torus) around the beam. Right: Simplified equivalent circuit.

The value of the induction can be chosen by the core size (as given by r_i and r_o) and the number of windings N . A further reason for the torus is to guide the field lines, so only the azimuthal component is measured and the signal strength is nearly independent of the beam position inside the vacuum pipe.

Generally, for an ideal current transformer loaded with a low value of ohmic resistance R , the ratio between the primary current I_{prim} conducted in N_{prim} windings and the secondary current I_{sec} conducted in N_{sec} is given by

$$I_{\text{sec}} = \frac{N_{\text{prim}}}{N_{\text{sec}}} \cdot I_{\text{prim}} \implies I_{\text{sec}} = \frac{1}{N} \cdot I_{\text{prim}} \quad \text{as } N_{\text{prim}} = 1 \quad (5)$$

$N_{\text{prim}} = 1$ owing to the single pass of the beam through the torus. N_{sec} is the winding number on the secondary side; for simplicity, it is called N in the following.

For most practical cases, a measurement of a voltage U is preferred; therefore, the resistance R is introduced, leading to

$$U = R \cdot I_{\text{sec}} = \frac{R}{N} \cdot I_{\text{beam}} \quad (6)$$

The ratio between the usable signal voltage U and the beam current I_{beam} is called the sensitivity S (or transfer impedance; for a more stringent discussion, see Section 6.1)

$$U = S \cdot I_{\text{beam}} \quad (7)$$

The properties of a transformer can be influenced using different external electrical elements to match the response to a given time structure of the beam. We first consider the characteristics of a so-called passive transformer or fast current transformer, where the voltage at a 50Ω resistor is recorded. The equivalent circuit of the secondary transformer side is depicted in the right-hand side of Fig. 2. The beam current is modelled by a current source with a reduction given by the number of windings N , according to Eq. 5. One also has to take some stray capacitance C_S into account, which is caused by the capacitance between the windings and the torus and along the shielded cable to the resistor R . Generally,

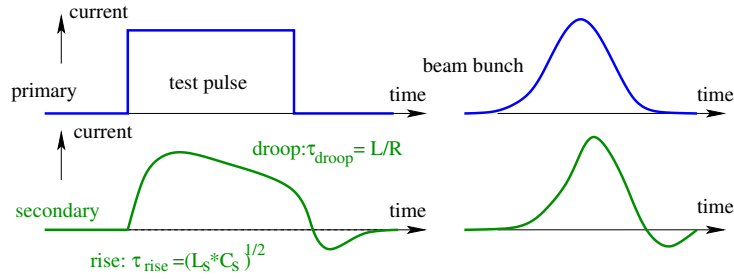


Fig. 3: Response of a.c. transformer to a rectangular pulse and a more realistic beam pulse

the voltage $U(t)$ of the parallel shunt of the three elements is measured. The response is influenced by the choice of elements, as discussed in Refs. [1–7, 12]; here, we state only the results.

For the following discussion, we are interested in the time response of the measurement device to a given beam pulse. Therefore, one frequently uses the rise time constant τ_{rise} and the droop time constant τ_{droop} , as depicted in Fig. 3. If the excitation is given by a step function, the signal amplitude A increases as $A \propto (1 - e^{-t/\tau_{\text{rise}}})$ and τ_{rise} corresponds to the time for an increase by $e^{-1} = 37\%$. It is linked to the upper cut-off frequency by

$$\tau_{\text{rise}} = \frac{1}{\omega_{\text{high}}} = \frac{1}{2\pi f_{\text{high}}} \quad . \quad (8)$$

Correspondingly, the droop time constant is linked to the lower cut-off frequency, as

$$\tau_{\text{droop}} = \frac{1}{2\pi f_{\text{low}}} \quad . \quad (9)$$

Both equations have a general meaning and will be used to transfer quantities, such as bandwidth, given in the frequency domain, into the corresponding description in the time domain

For the passive current transformer described by the equivalent circuit of Fig. 2, the rise and droop time constants are given by

$$\tau_{\text{rise}} = RC_S \quad \text{and} \quad \tau_{\text{droop}} = \frac{L}{R} \quad . \quad (10)$$

A more realistic schematic diagram of the passive transformer is shown in Fig. 4. The main difference is the additional loss resistivity in the cables, which is represented by a serial resistor R_L . Additionally, there is a stray inductance between the windings, which is best modelled by a serial insertion of an inductance L_S . With these two modifications, the rise and droop times are modified to yield

$$\tau_{\text{rise}} = \sqrt{L_S C_S} \quad \text{and} \quad \tau_{\text{droop}} = \frac{L}{R + R_L} \quad . \quad (11)$$

The specifications of the GSI device are listed in Table 1. Careful matching is necessary between the torus and the $50\ \Omega$ resistor R , where the voltage drop is measured.

An additional general point is that close to the transformer the electrical conductivity of the beam pipe has to be interrupted, as shown schematically in Fig. 5. This is done with an insulator, either a ceramic gap or a plastic vacuum seal. The reason is to prevent a flow of image current inside the transformer torus. This image current has the opposite sign; without the gap, the fields of the image current and beam current add up to zero. The image current must be bypassed outside of the transformer torus by some metallic casing. It is surrounded by high-permeability μ -metal, also used for the shielding of the transformer against external magnetic fields. A general review of transformers is presented in Refs. [12, 14].

Passive transformers are mainly used when beam pulses in a time range from nanoseconds to microseconds are to be observed. The observables for the beam are the actual bunch shape, the arrival

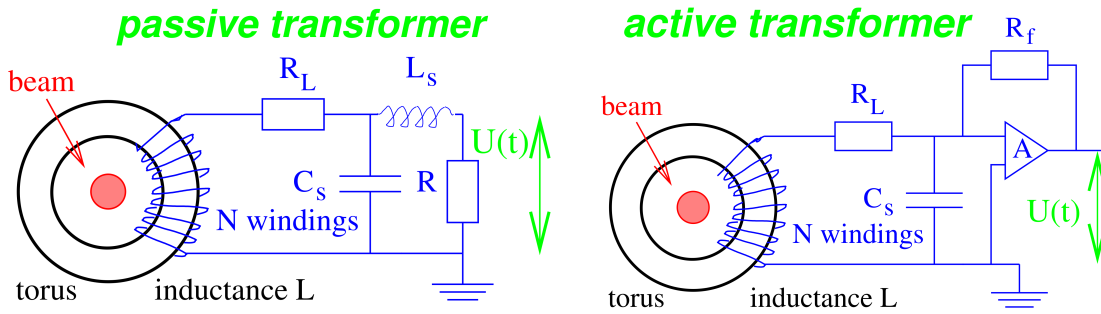


Fig. 4: Equivalent circuits. Left: Passive beam transformer. Right: Active transformer

Table 1: Basic specifications of GSI passive transformer [13]

Parameter	Value
Torus radii	$r_i = 70 \text{ mm}, r_o = 90 \text{ mm}$
Torus thickness, l	16 mm
Torus material	Vitrovac 6025: $(\text{CoFe})_{70\%}(\text{MoSiB})_{30\%}$
Torus permeability, μ_r	$\mu_r \approx 10^5$ for $f < 100 \text{ kHz}$, $\mu_r \propto 1/f$ for $f > 100 \text{ kHz}$
Number of windings, N	10
Sensitivity, S	4 V/A at $R = 50 \Omega$ (10^4 V/A with amplifier)
Current resolution, I_{\min} for $S/N = 1$	40 μA_{rms} for full bandwidth
Droop time constant, $\tau_{\text{droop}} = L/R$	0.2 ms, corresponding to 5% per 10 μs pulse length
Rise time constant, $\tau_{\text{rise}} = \sqrt{L_S C_S}$	1 ns
Bandwidth	$f_{\text{low}} = 0.75 \text{ kHz}$ to $f_{\text{high}} = 660 \text{ MHz}$

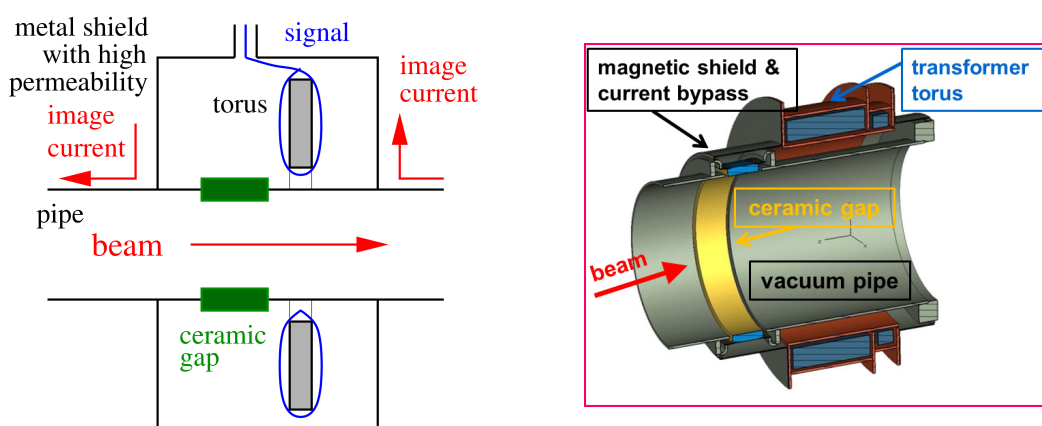


Fig. 5: Left: General scheme of beam pipe intersected by a ceramic gap and a transformer casing, as used as an image current pass and a shielding against external magnetic fields. Right: Technical drawing for a transformer arrangement surrounding a beam pipe, including the gap and magnetic shield.

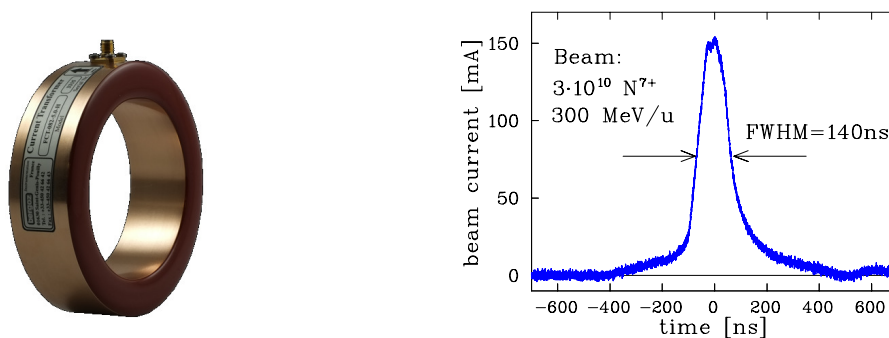


Fig. 6: Left: Commercially available passive transformer [11]. Right: Signal from passive transformer for single beam bunch extracted from GSI synchrotron at 300 MeV/u.

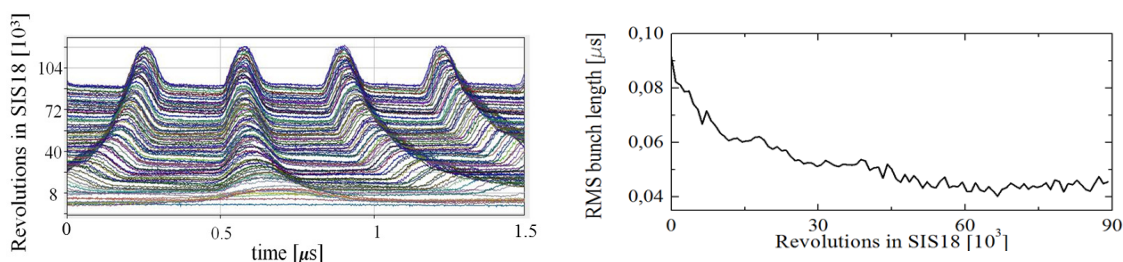


Fig. 7: Left: Signals from a passive transformer installed in the GSI synchrotron during the acceleration of a U^{73+} beam. The beam is injected at 11 MeV/u, corresponding to a velocity of $\beta = 15\%$; then four bunches are built and accelerated to 350 MeV/u, corresponding to $\beta = 69\%$, with an accelerating frequency swing from 0.85 MHz to 3.80 MHz within 0.3 s. A trace of the circulating bunches is shown for each 0.15 ms. Right: Width (one standard deviation) of the bunches during acceleration.

time with respect to an external reference (e.g., the acceleration frequency), and the total number of particles, gained by integration of the signal. A first example is shown in Fig. 6 for one bunch extracted from a synchrotron within one revolution, so-called fast extraction. For this case, the passive transformer is installed in the beam pipe outside the synchrotron. The beam pulse length is typically between 1 ns and 10 μ s. Moreover, with the passive transformer, the bunch structure can be observed in the time domain and a bandwidth, typically 1 GHz, corresponding to a rise time constant of $\tau_{\text{rise}} = 160$ ps, can be achieved [11, 13].

As a second example, the observation of the bunch structure during acceleration inside a synchrotron is shown in Fig. 7 for the acceleration of an ion beam injected at a non-relativistic velocity of $\beta = 15\%$ of the velocity of light and accelerated to $\beta = 69\%$. Owing to the increase of the velocity, the bunches approach each other and get smaller, as expected from the conservation of the normalized longitudinal emittance (see Section 7). Generally, observation of bunches during acceleration and of possible bunch merging or splitting is done by the fast current transformer and, eventually, a feedback system to control the acceleration frequency, amplitude, and phase is generated from the fast current transformer signal. For injection alignment and extraction timing, the bunch shape is recorded in connection with the kicker signal and eventually corrected to prevent for varying kicker angle during the bunch passage; some examples are discussed in other contributions to these proceedings.

2.1.2 Active a.c. transformer

To observe beam pulses longer than several microseconds, the droop of a passive transformer leads to a significant deformation of the measured signal, as shown schematically in Fig. 3. The droop time constant

Table 2: Some basic specifications of GSI linac active transformer

Parameter	Value
Torus radii	$r_i = 30$ mm, $r_o = 45$ mm
Torus thickness l	25 mm
Torus material	Vitrovac 6025: (CoFe) _{70%} (MoSiB) _{30%}
Torus permeability, μ_r	$\simeq 10^5$
Number of windings, N	2×10 , with opposite orientation
Maximal sensitivity, S	10^6 V/A (with operational amplifier)
Ranges of beam current	1 μ A to 100 mA
Current resolution, I_{\min} for $S/N = 1$	0.2 μ A _{rms} for full bandwidth
Droop	<0.5% for 5 ms pulse length
Upper cut-off frequency, f_{high}	1 MHz (as given by operational amplifier property)
Rise time constant, τ_{rise}	160 ns

can be made much longer by using an operational amplifier, with feedback resistor R_f and open-loop gain A , instead of a constant resistor to measure the voltage. The equivalent circuit is shown in the right-hand panel of Fig. 4. The effect is the reduction of the operational amplifier input resistance by a factor of R_f/A . This is the set-up of a so-called transimpedance amplifier or current-to-voltage converter. The remaining resistance is, in most cases, only given by the cable resistivity R_L , since $R_f/A \ll R_L$. The droop is now

$$\tau_{\text{droop}} = \frac{L}{R_f/A + R_L} \simeq \frac{L}{R_L}. \quad (12)$$

Droop time constants up to 1 s are possible. (Typical values of the cable resistance, R_L are of the order of 1 Ω .) An additional winding (not shown in the right-hand panel of Fig. 4) must be used to compensate for the ‘natural’, known, droop. In addition, the feedback resistor R_f of the operational amplifier can be used for range switching. A transformer that utilizes this principle is called an active transformer or alternating current current transformer.

The rise time τ_{rise} for this active type is much larger than for the passive type. This is mainly because of the choice of a low bandwidth (low value of the upper cut-off frequency) of the operational amplifier to obtain a significant reduction of the amplifier’s high-frequency noise. This results in the high sensitivity of an active transformer.

The specifications of a typical device [13] used at the heavy-ion linac at GSI with pulse lengths of 100 μ s (used when filling a synchrotron) and 5 ms (used directly in experiments) are given in Table 2; a photograph of the hardware is shown in Fig. 8. For a specification of the parameters of the commercially available type, see Ref. [11].

A measurement made with these types of transformer is shown in the left-hand panel of Fig. 9; one macroscopic pulse is recorded at three locations, starting at the ion source and ending at the exit of the first linac tank. A high-current ion beam is generated in the source with ~ 0.5 ms length. The slow rise of the beam current before the linac results from the build-up of the space charge compensation of the unbunched beam. A chopper in front of the linac is used to generate the necessary pulse length. Transformers are essential to determine and maximize the transmission through the accelerator, in particular if the ion source conditions are not very stable. A non-destructive method is needed to follow the beam pulse for its pass through the full accelerator. During the operation of the accelerator, these transformers are the most frequently used diagnostics tools.

To control the filling of a synchrotron by a pulse from a linac, transformers of the described type are used; one is mounted in the external beam line, measuring the delivered current, and the other is installed inside the synchrotron to determine the stored current. The used multiturn injection is done

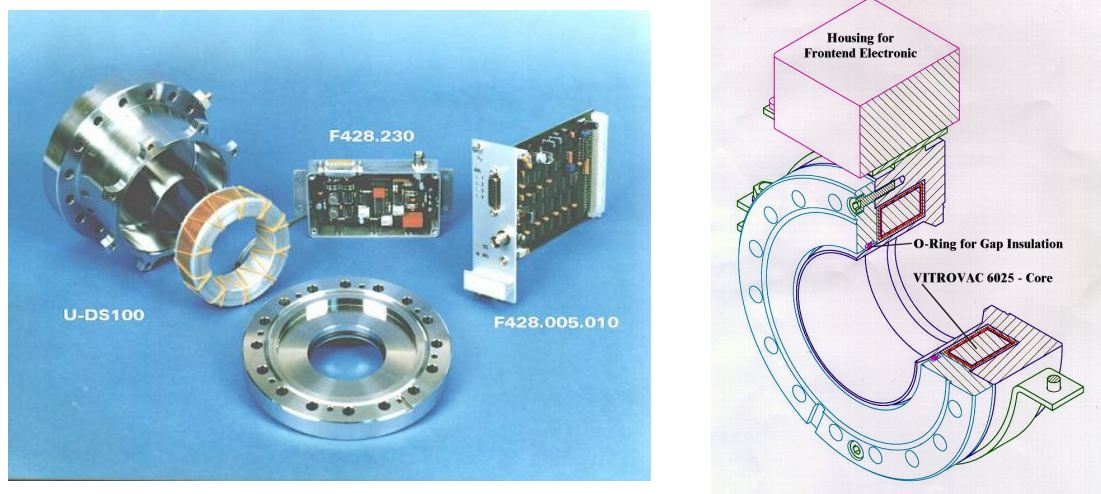


Fig. 8: Left: An a.c. current transformer used at the pulsed heavy-ion linac at GSI. The torus with the differential winding is shown, together with the electronic modules. Right: Technical drawing of same transformer.

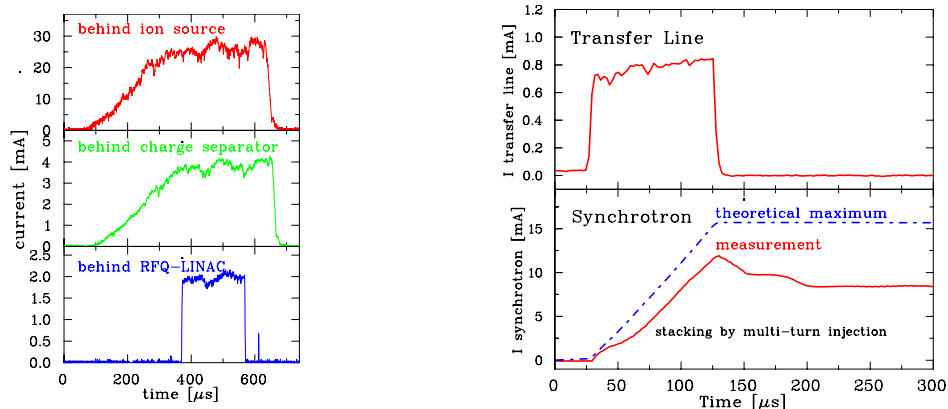


Fig. 9: Left: Transmission determination by a.c. transformers at three different locations at the GSI linac using a Ni^{2+} beam from a high-current source. The upper curve shows the current after the ion source, where all charge states are present. The middle curve shows the current behind a magnetic bend to filter the Ni^{2+} ionic state. The third curve shows the current after the first linac module. Right: Multiturn injection at GSI measured with two a.c. transformers. The upper curve is the current delivered by the linac and the lower curve is the current stored in the synchrotron. In this case, 20 turns are used and 70% efficiency is achieved for this Ni^{26+} beam.

with some bumper magnets to fill the large horizontal acceptance of the synchrotron by the linac pulse, which is much longer than the revolution period. Such a measurement at the GSI facility is shown in the right-hand panel of Fig. 9: the injection takes place over 20 turns and an accumulation by a factor of ~ 15 is achieved. For each beam setting, optimization of the injection process is an important task, in order to achieve maximal matching.

2.2 The d.c. transformer

An important task for beam diagnostics is the measurement of a coasting (or so-called direct current) beam current. The application is either a linac that permanently produces a beam (so-called continuous wave mode) or a synchrotron with storage times from seconds to many hours. The transformers discussed in the previous sections only work for a pulsed beam, even though the droop time constant can be made to be of the order of a second.

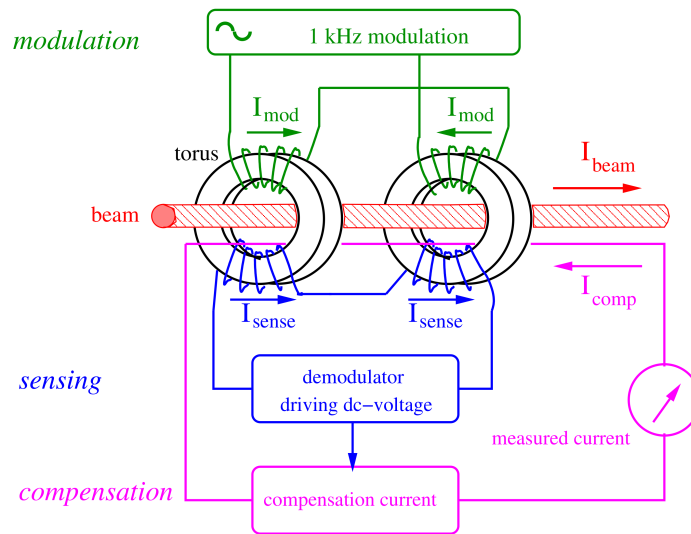


Fig. 10: Schematic of d.c. transformer (see text)

The principle of a d.c. transformer, the so-called direct current current transformer [11, 13, 15], is shown schematically in Fig. 10. It consists of two tori with three types of winding each. The first windings of each torus, with opposite orientation, are used as a modulator. The modulation frequency is typically 1–10 kHz. The amplitude of the modulation current is high enough to force the torus into a magnetic saturation of $B_{\text{sat}} \simeq 0.6$ T, for positive and negative azimuthal orientation each period. The secondary windings, with equal orientation, act as a detector for the modulated signal, see Fig. 11. Assuming perfectly identical magnetic characteristics of both tori, the detector signal, as shown in the scheme, should be exactly zero if there is no beam current flowing through the tori. However, an asymmetric shifting of the hysteresis curve results if a d.c. beam is fed through the tori, because of the additional magnetic field from the beam. The sum signal U_S is different from zero, with a modulation twice the modulation frequency. In the demodulator stage, this signal is rectified. The d.c. current is measured by means of the current generated in the feedback compensation circuit, which forces the output signal back to zero, flowing through the third windings of both tori. The detector can even be used at even harmonics of the modulation frequency, resulting in higher sensitivity and an improvement in the signal-to-noise ratio. Owing to the extremely specific requirements concerning the matching of the magnetic characteristics for a pair of tori, the design of a magnetic modulator with high resolution and d.c. stability is rather complex and depends very much on the selection and treatment of the core-material, as discussed in more detail in Ref. [15]. The applied feedback circuit for the zero flux compensation makes the device very sensitive and linear. To get a fast response, the signal from an a.c. transformer is added to the feedback circuit. With this enhancement, the time resolution of the full device is of the range of 20 μs .

The specifications of a typical d.c. transformer developed for the heavy-ion synchrotron at GSI are given in Table 3 and a photograph is given in Fig. 12. The resolution is about 1 μA . The offset drift, mainly caused by the magnetic properties of the tori, are of the order of 20 μA per day. The offset can be improved by an automatic zero compensation when the synchrotron does not contain any beam, e.g., after the ramp-down phase of the magnets. For the parameters of the commercially available type, see Ref. [11].

An example of a d.c. transformer measurement is shown in Fig. 13. The electrical current and the number of stored particles are shown. A $^{238}\text{U}^{73+}$ beam is injected in the synchrotron and acceleration starts shortly after the injection. A loss of particles is seen during the RF bunching process, owing to some misalignment. During the acceleration, the slope of the magnetic field $\text{d}B/\text{d}t = 1.3$ T/s is constant, resulting in a constant increase in the particle momentum. The current increases linearly only for non-

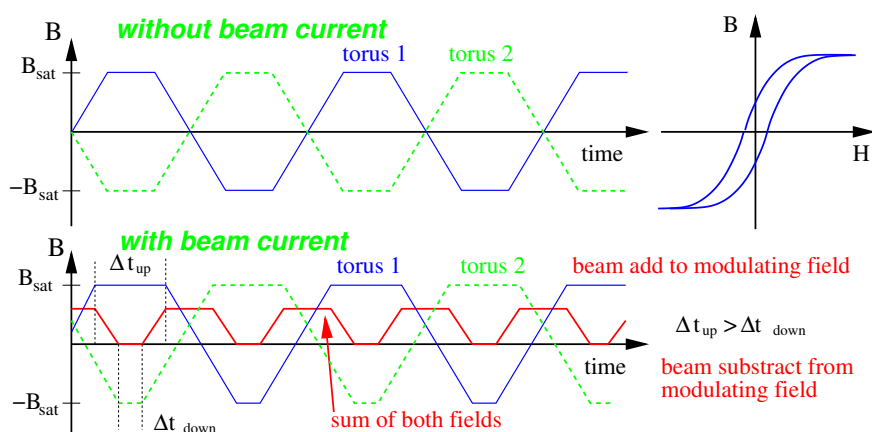


Fig. 11: Fluxes in the two tori of a d.c. transformer without and with a beam. The magnetic field of the beam adds to the modulated field for one modulation phase and 180° later it is subtracted. The sum of the maximum magnetization gives the measured signal. The scheme is drawn for a triangular-modulation; for a realistic sine modulation, the edges are smoother.

Table 3: Specifications of d.c. transformer installed at GSI synchrotron

Parameter	Value
Torus radii	$r_i = 135 \text{ mm}, r_o = 145 \text{ mm}$
Torus thickness, l	10 mm
Torus material	Vitrovac 6025: $(\text{CoFe})_{70\%}(\text{MoSiB})_{30\%}$
Torus permeability	$\mu_r \simeq 10^5$
Isolating gap	Al_2O_3
Number of windings, N	16 for modulation and sensing 12 for feedback
Ranges for beam current	300 μA to 1 A
Current resolution, I_{\min} for $S/N = 1$	2 μA
Bandwidth	d.c. to 20 kHz
Rise time constant, τ_{rise}	20 μs
Offset compensation	$\pm 2.5 \mu\text{A}$ in auto mode <15 $\mu\text{A/day}$ in free run
Temperature coefficient	1.5 $\mu\text{A}/^\circ\text{C}$

relativistic velocities, owing to the decrease in the revolution time, which is inversely proportional to the velocity. For the maximal energy of 750 MeV/u, corresponding to $\beta = 84\%$, the relativistic increase of the mass starts to be significant. After reaching the maximum energy, a ~ 0.5 s flat top is seen for the de-bunching phase. The slow extraction of several seconds is achieved by changing the tune using a fast quadrupole to get close to a $1/3$ resonance, to blow up the transverse beam dimension. The resonant beam particles are then separated from the circulating stable beam by an electrostatic septum and are extracted.

2.3 Energy loss and ranges of particles in matter

2.3.1 Material interaction of protons and ions

For the discussion for all intercepting diagnostics, such as Faraday cups, ionization chambers, wire scanners, etc., the energy loss, with the related range of the particles penetrating the matter, serves as the basic physical mechanism. The energy loss of a proton or an ion is mainly due to the collision of the projectile with the electrons of the stopping target, so-called electronic stopping. Owing to the different masses

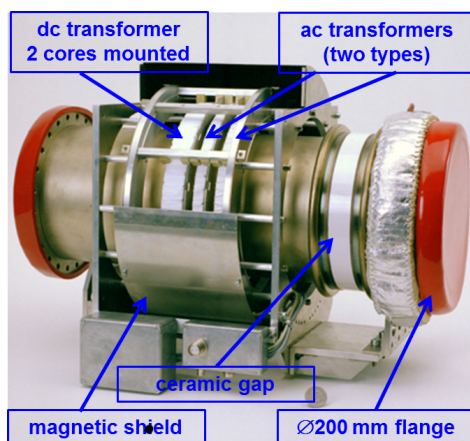


Fig. 12: The d.c. transformer installed at the GSI synchrotron. The left torus is the d.c. transformer (two tori mounted closely together), the middle is the a.c. transformer used for the feedback of the d.c. type and the right one is the a.c. transformer for injection control.

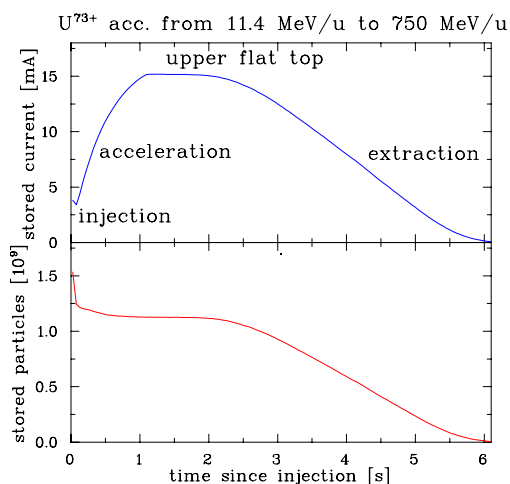


Fig. 13: Signal of a d.c. transformer for a $^{238}\text{U}^{73+}$ beam at the GSI synchrotron. The acceleration must be about 1 s. After a delay of about 0.5 s, the slow extraction for 4 s follows.

of the ion and the electron, the energy transfer to the electron per collision is, in most cases, <100 eV. The electronic stopping power dE/dx can be approximated by the semi-classical Bethe–Bloch formula, which is written in its simplest form as [16–18]

$$-\frac{dE}{dx} = 4\pi N_A r_e^2 m_e c^2 \cdot \frac{Z_t}{A_t} \rho \cdot \frac{Z_p^2}{\beta^2} \left[\ln \frac{2m_e c^2 \gamma^2 \beta^2}{I} - \beta^2 \right] \quad (13)$$

where N_A is the Avogadro constant, m_e and r_e are the mass and classical radius of an electron, respectively, and c is the velocity of light. The target parameters are ρ , the density of the target with nuclear mass A_t and nuclear charge Z_t ; the quantity $Z_t \rho / A_t$ corresponds to the electron density. I is the mean ionization potential for removing one electron from a target atom; a rough approximation for a target with nuclear charge Z is $I \simeq Z \times 10$ eV; more precise values are given, e.g., in Refs. [19,20]. The projectile parameters are Z_p , the nuclear charge of the ion, with velocity β and $\gamma = (1-\beta^2)^{-1/2}$. This formula must be modified because ions travelling through matter are not bare nuclei, but have some inner electrons. An effective charge is used instead of Z_p , calculated by, e.g., semi-empirical methods described for the

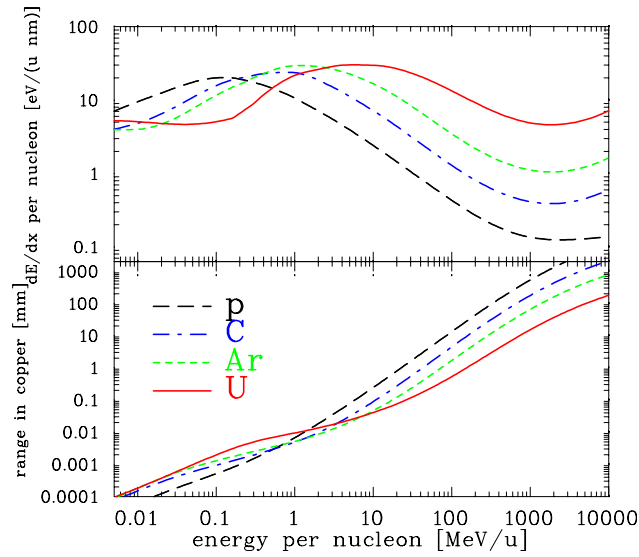


Fig. 14: Energy loss per nucleon at the surface and range in copper as a function of the kinetic energy for several ions. The energy range is plotted from 5 keV/u to 10 GeV/u and the range from 100 nm to 1 m. The calculation of the electronic and nuclear stopping uses the semi-empirical code SRIM [19, 20].

codes SRIM [19, 20] or LISE++ [21]. The result of such a semi-empirical calculation for the energy loss is shown in Fig. 14 for different ions into copper. The energy loss is maximal for ions with a kinetic energy around 100 keV/u to 7 MeV/u (corresponding to velocities $\beta \sim 1.5\%$ to 12%), depending on the ion species. These are typical energies of a proton or heavy-ion linac. Below 100 keV/u, the energy loss decreases and nuclear stopping becomes significant. Energies below 10 keV/u are typical for proton or heavy-ion sources mounted on a high-voltage platform. For relativistic energies above 1 GeV/u, the energy loss is nearly constant; these are typical energies of particles extracted from a synchrotron.

For the consideration of a Faraday cup (see Section 2.4), the range in material is important. Copper is often used for cups, owing to its high heat conductivity. For a particle accelerated to E_{kin} , the range R is calculated numerically from the stopping power via

$$R = \int_0^{E_{\text{kin}}} \left(\frac{dE}{dx} \right)^{-1} dE \quad (14)$$

and has an approximately scaling for ions above $\simeq 10$ MeV/u [16] of

$$R \propto E_{\text{kin}}^{1.75}. \quad (15)$$

The results are shown in Fig. 14. This range should be shorter than the mechanical dimension for a practical Faraday cup design; for energies below 100 MeV/u, the range is less than 1 cm. Or, in other words, cups are only useful at linacs or cyclotrons. For higher energies, the range is too large and other techniques, e.g., particle detectors, as described in Section 2.5, are applied. In addition, for particles above the nuclear Coulomb barrier, nuclear reactions are possible and charged particles might leave the material, resulting in an incorrect reading.

2.3.2 Material interaction of electrons

The stopping of electrons in matter differs from protons and ions; see Fig. 15, where the sum of the two relevant processes of collisional loss $dE/dx|_{\text{col}}$ and radiation loss $dE/dx|_{\text{rad}}$ is plotted. The collisional loss for electrons due to electronic stopping $dE/dx|_{\text{col}}$ is also described by a modified Bethe–Bloch

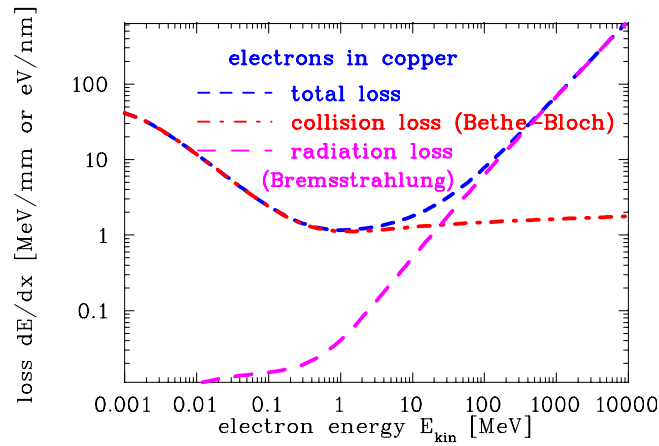


Fig. 15: Energy loss of electrons in copper for collision loss, as given by the Bethe–Bloch equation, and radiation losses, as dominated by the emission of Bremsstrahlung (data from Ref. [22]).

formula; the modification is caused by the equal mass of the projectile and the target electrons and their indistinguishability. This regime dominates only for energies below 1 MeV, as corresponding to a velocity of $\beta = v/c = 94\%$ and a Lorentz factor of $\gamma = (1 - \beta^2)^{-1/2} = 2.96$. Even a small electron accelerator attains larger final energies. For energies above a few tens of megaelectronvolts, the radiation loss by Bremsstrahlung, i.e., the emission of photons through the acceleration or deceleration of electrons in the vicinity of the target nucleus, is dominant, see, e.g., Ref. [16]. This radiation loss scales roughly linear to the electron energy and quadratically to the target charge Z_t as $dE/dx|_{\text{rad}} \propto E \cdot Z_t^2$. The trajectories of the primary electrons in the target are more curved than for ions, owing to the possible high energy and momentum transfer in a single collision; therefore, electrons have much larger lateral straggling than ions. Moreover, the longitudinal straggling is larger than for ions, resulting in a wider range distribution.

At electron accelerators, Faraday cups are mainly used behind the electron gun for electrons with typically 100 keV energy. In this case, the construction is comparable to the Faraday cups used for proton beams, see Section 2.4. At higher energies, the required amount of material to stop the electrons and to absorb secondary charged particles (e.g., e^+e^- pair production from the Bremsstrahlung) increases significantly, owing to this long range. An example of a Faraday cup used for high energies up to some gigaelectronvolts, including design considerations, can be found in Ref. [23].

2.3.3 Secondary electron generation

When a charged particle, either an ion or an electron, travels through matter, it interacts with the target electrons, as schematically depicted in the left-hand panel of Fig. 16. In a close primary collision, the target electron can be accelerated to high energies much larger than 100 eV; sometimes these electrons are called δ -rays. The energy distribution depends on the impact parameter and the energy of the incoming particle. In a metallic solid-state material, the fast δ -electrons collide with the surrounding electrons; because both collision partners have equal masses, the energy is transferred efficiently and more electrons are liberated, see Fig. 16. This so-called thermalization of the electrons inside the conduction band is performed in a typical scattering length of $L_s \simeq 10$ nm, i.e., within the distance of some 100 lattice planes. Owing to these many collisions, there is only a weak correlation between the direction of the incoming particle and the scattered electrons. If these electrons reach the surface and still have an energy greater than the work function (typically 1 to 5 eV), they have a high probability of escaping from the metal. The current of the secondary electrons is given by the so-called Sternglass formula [24]

$$I_{\text{sec}} = Y \cdot \frac{dE}{\rho dx} \cdot I_{\text{beam}} \quad (16)$$

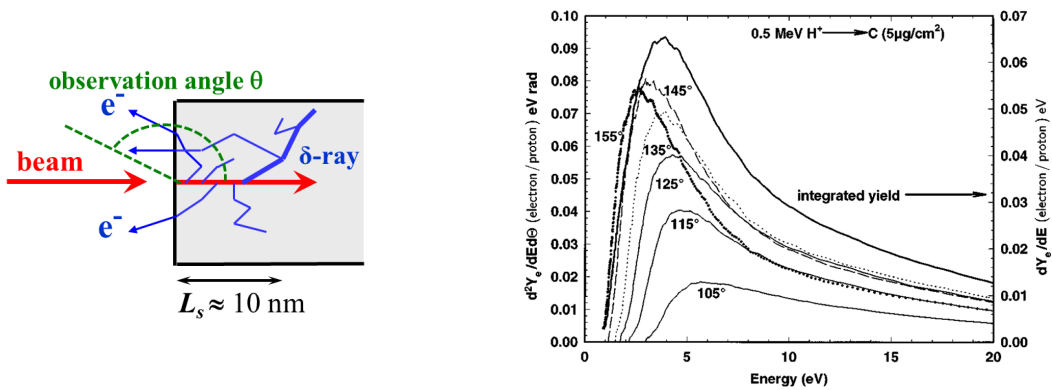


Fig. 16: Left: Secondary electron generation from a surface by charged particle impact; L_s is the scattering length from which electrons are able to reach the surface. Right: Typical measurement of electron energy spectrum for different emission angles and total yield in backward direction by 0.5 MeV proton impact on a carbon foil [25].

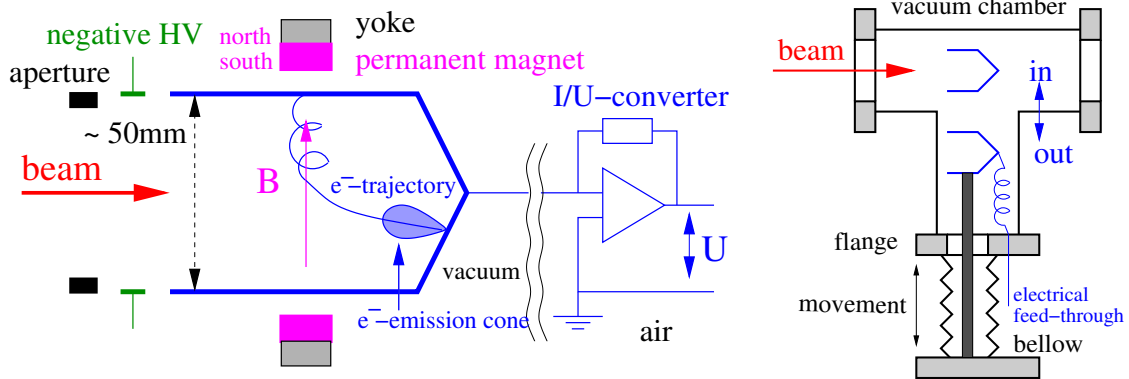


Fig. 17: Left: Scheme of an uncooled Faraday cup with magnetic and electric secondary electron suppression. Right: Scheme for inside and outside position of destructive diagnostics devices.

where I_{beam} is the current of incoming particles and Y is the yield factor describing the amount of secondary emission per unit of energy loss $dE/\rho dx$ at the surface of the metal. The yield Y depends on the metal (via the work function) and the surface quality, e.g., modified by possible adsorbed gas contamination. The mean kinetic energy of the escaping secondary electrons is of the order of 10 eV and has some dependence on the emission angle; an example for the energy spectrum is shown in Fig. 16 and discussed in more detail in Ref. [25]. To first order, the angular distribution $P(\theta)$ of the electron emission can be approximated by a $P(\theta) \propto \cos \theta$ law, where θ is the angle of the trajectory with respect to the surface ($\theta = 180^\circ$ indicates back scattering).

2.4 Faraday cups for low currents

A Faraday cup is a beam stopper that is designed to measure the electrical current of the beam. The basic cup design is shown in Fig. 17 and a photograph is given in Fig. 18. An isolated metal cup is connected to a current-sensitive pre-amplifier. As shown for an active beam transformer, the pre-amplifier consists of a low-impedance input and a conversion to a voltage. Range switching is achieved by using different feedback resistors for the operational amplifier. Much smaller currents can be measured with a Faraday cup than with a transformer: a measurement of 10 pA for a d.c. beam is possible with a low-noise current-to-voltage amplifier and careful mechanical design; this is five orders of magnitude more sensitive than a d.c. transformer. Low-current measurement is important, e.g., for the acceleration of radioactive beams.



Fig. 18: Uncooled Faraday cup ($\varnothing 50$ mm) with magnetic and electric secondary electron suppression

When an accelerated particle hits a surface, secondary electrons are liberated, see also Section 2.3. The flux of these electrons is proportional to $\cos \theta$, where θ is the angle of the electron trajectory with respect to the surface; their average energy is less than $\simeq 10$ eV. If these electrons leave the insulated cup, the reading of the beam current is wrong by this amount. A secondary electron suppression has to be foreseen. It can be realized as follows.

- By using a high-voltage suppression close to the entrance of the cup. By applying a voltage well above the mean energy of the secondary electrons, they are pushed back to the cup surface, see the left-hand panel of Fig. 19. The disadvantage of this method is related to the fact that the electrical field on the beam axis is smaller than that at the edges; in the depicted case, the maximum potential is about 35% of the potential applied to the electrode. The emission of the maximal energetic electrons occurred opposite to the beam direction and the potential must be chosen to be greater than the kinetic energy of at least 99% of the electrons. A measurement with varying suppression voltage is shown in the right-hand panel of Fig. 19.
- By using a magnetic field created by permanent magnets. In this field B , the secondary electrons spiral around the magnetic field lines with the cyclotron radius r_c

$$r_c = \frac{\sqrt{2m_e E_{\text{kin}}}}{eB} \quad (17)$$

where m_e is the electron's mass, e is its charge, and E_{kin} is the kinetic energy component perpendicular to the field lines. For $E_{\text{kin}} = 10$ V and a field of 10 mT, $r_c \sim 1$ mm. With permanent magnets, field lines perpendicular to the beam axis can be created relatively easily, see Fig. 20.

2.5 Low-current measurement used for slow extraction

Many experiments in particle, atomic, or nuclear physics use protons or ions in the energy range as reached in synchrotrons, i.e., higher than some 100 MeV/u. A typical beam current during the acceleration inside the synchrotron followed by a slow extraction recorded by a d.c. transformer is shown in Fig. 13. Typical beam currents, as slowly extracted from a synchrotron range, from only 10^3 to 10^{12} particles per second, which corresponds to an electrical current from 10^{-15} to 10^{-6} A. This is well below the resolution of a d.c. transformer. Owing to the high energy, the range of the particles is too large for the use of Faraday cups, as shown in Fig. 14 for copper. In addition, a lot of secondary charged particles would be created in the cup material. The techniques of particle detectors are used instead. An overview of the typical dynamic range of detectors is presented in Fig. 21.

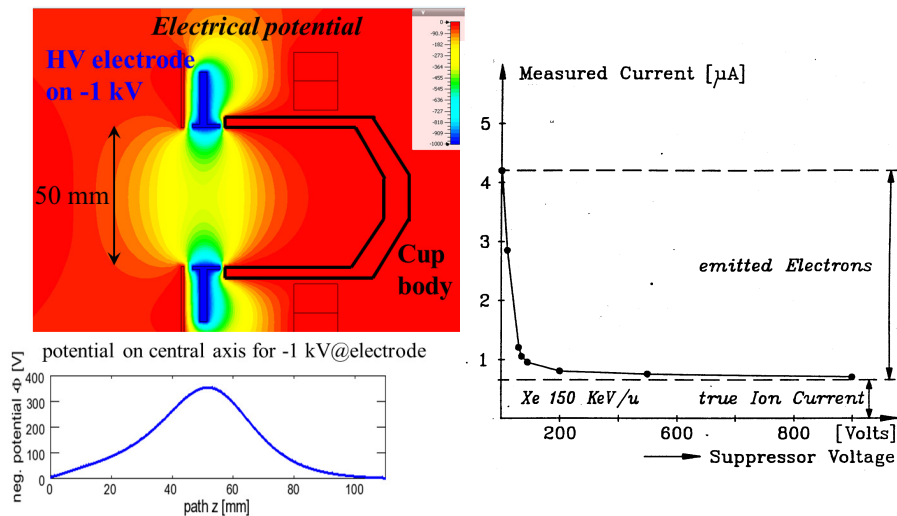


Fig. 19: Left: The electric potential of the Faraday cup shown in Fig. 18 with the high-voltage electrode biased by -1 kV is shown at the cylindrical symmetry plane. The beam enters from the left. The negative potential along the central axis is depicted at the bottom. Right: The effect of secondary electron suppression inside a Faraday cup as determined by the beam current determination as a function of applied voltage.

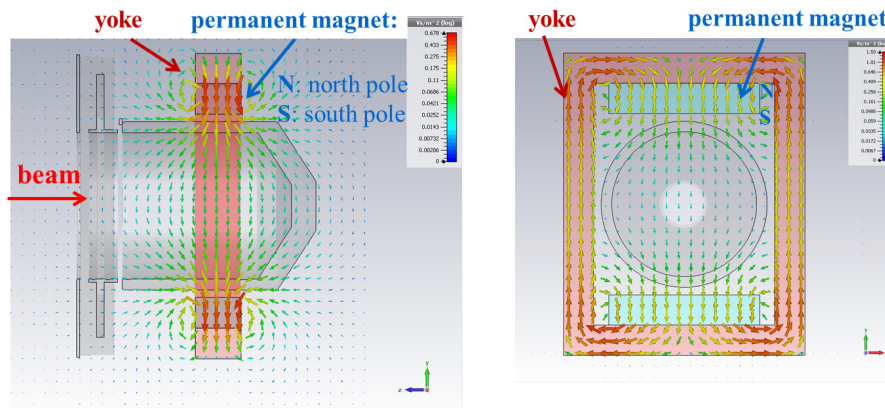


Fig. 20: Magnetic field lines of the arrangement of Co-Sm permanent magnets within the yoke for the Faraday cup of Fig. 18. The homogeneous field strength is $B \sim 60$ mT.

- For an ion rate below 10^6 s $^{-1}$, the individual particles can be counted by scintillators.
- For the medium range, from about 10^4 to 10^9 s $^{-1}$, the energy loss in a gas is measured by an ionization chamber.
- For the higher range, from about 10^8 s $^{-1}$, the emission of secondary electrons from a metal surface forced by the primary ion's energy loss is determined by secondary electron multipliers (SEMs).

The design of such a system and the combination of the three detector is described in, e.g., Refs. [26–28].

2.5.1 Scintillation counter

When a charged particle penetrates a scintillating material, the electronic energy lost by the collision of the beam particles with the target electrons creates atomic excitation; the excited atoms might then decay via emission of fluorescence photons. These photons can be detected and amplified by a photomultiplier,

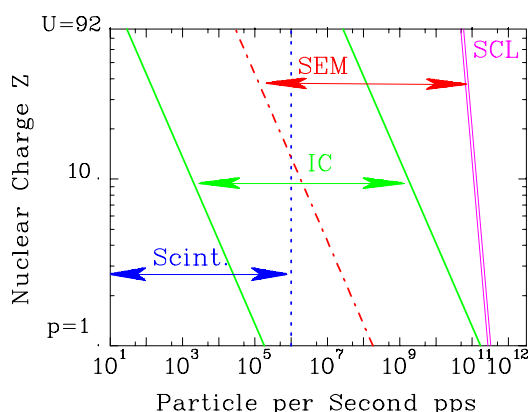
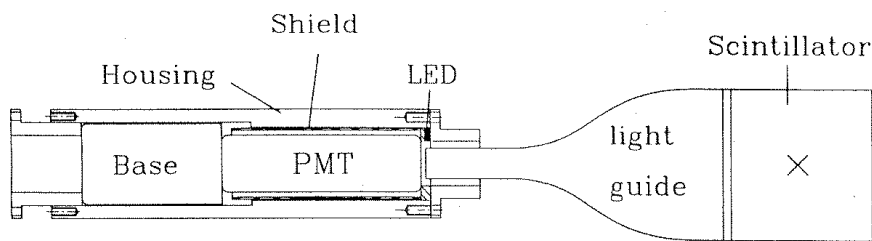


Fig. 21: Overview of the different detector systems used for slow extraction at the GSI synchrotron. The numbers are given for the different ions with a kinetic energy of 1 GeV/u, extracted within 1 s, and a spot size of 1 cm². With a scintillator, up to 10⁶ particles can be counted. The lower limit of the ionization chamber and SEM correspond to a secondary current of 1 pA, the upper threshold of the ionization chamber is 30 Gy/s. SCL: incoherent space charge limit of the synchrotron at injection energy.



Multiplier Tube:

Philips XP2972 (1")

Gain $\approx 10^4 \dots 10^6$

Anode rise time < 2 ns

Scintillator:

Pilot U

75 x 75 x 1.0 mm³

Pulse Width 1.2 ns

Fig. 22: Plastic scintillation counter connected to photomultiplier via plastic light guide

converted to a logical pulse by a discriminator and finally counted by a scaler; for more details see Refs. [16, 17].

In most cases, plastic scintillators are used. They are cheap and easy to produce in nearly every mechanical shape. As an example, the arrangement used at GSI is shown in Fig. 22 and a photograph, together with an ionization chamber, is shown in Fig. 23. A large size of 75 mm × 75 mm has been chosen with a thickness in the beam direction of 1 mm. The plastic scintillator (in this case BC 400) has a short decay time in the range of some nanoseconds, see, e.g., Ref. [17]. Typical pulses are displayed in Fig. 24, recorded with a medium-energy heavy-ion beam. The energy resolution is quite good, which is important because it yields good accuracy of this absolute count rate measurement. Owing to the long cables, several hundreds of metres long, used between the detector in the beam pipe and the electronic processing, cable dispersion broadens the peak. Before pile-ups start to play a role, count rates up to several 10⁷ s⁻¹ can be accepted. A typical measurement of an extracted current is shown in Fig. 25, where the particle rate as determined by a scintillator is compared with the particle rate as determined by an ionization chamber. This is corroborated with the signal of the d.c. transformer measuring the stored current in the synchrotron.

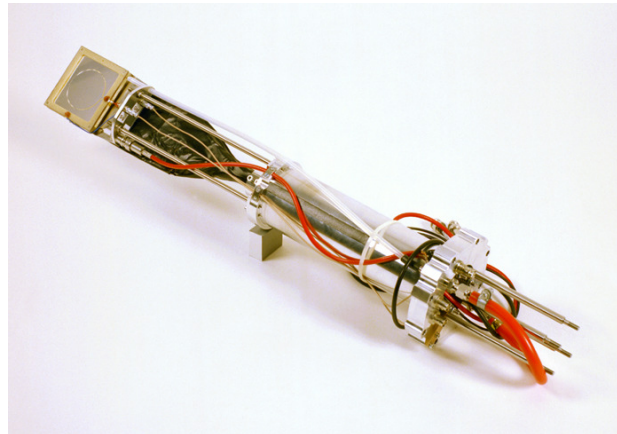


Fig. 23: The hardware of the scintillators (wrapped in black tape) and the ionization chamber installed at GSI

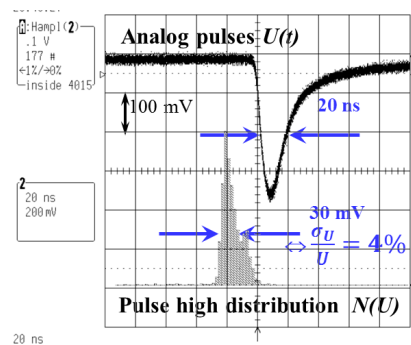


Fig. 24: Analogue pulses from a plastic scintillator recorded with a low-current 300 MeV/u Kr beam; the scaling is 20 ns per division and 100 mV per division. The lower curve is the pulse height distribution.

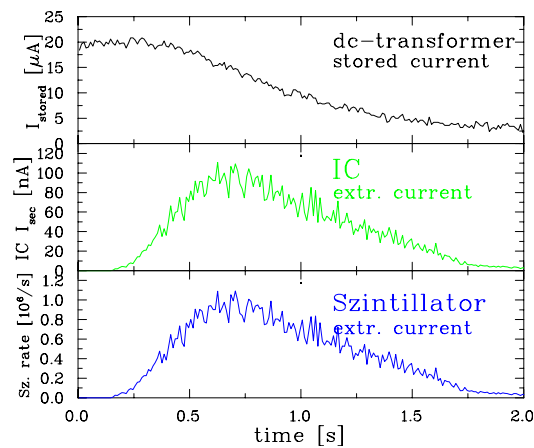
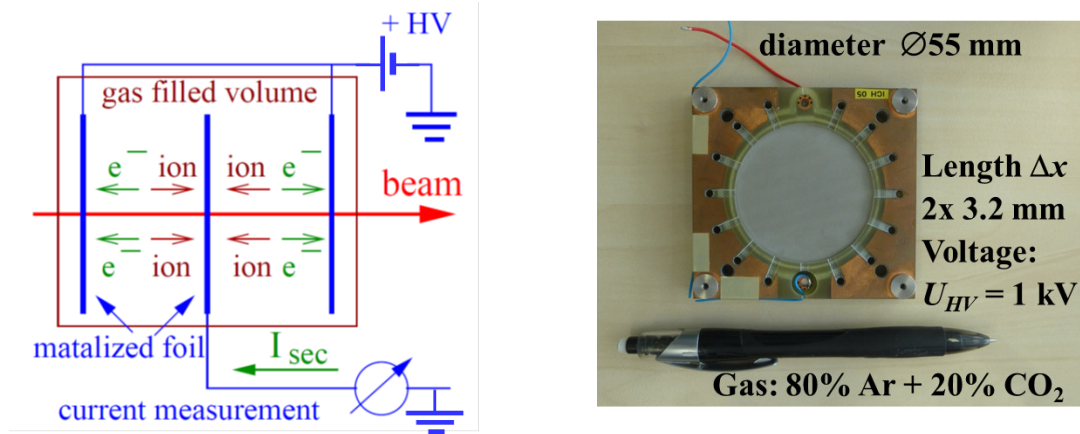


Fig. 25: Extracted current measured by an ionization chamber (middle, given in nanoamps for the secondary current) and a scintillator (bottom, given in particles per second) as compared with the current inside the GSI synchrotron determined by a d.c. transformer (top, given in microamps) for one extraction of a 250 MeV/u $^{208}\text{Pb}^{67+}$ beam with a total amount of 10^6 particles.

Table 4: Ionization potential and W values

Gas	H ₂	He	N ₂	O ₂	Ar	CH ₄	CO ₂
Ionization potential [eV]	15.6	24.5	15.5	12.5	15.7	14.5	13.7
W value [eV]	36.4	42.7	36.4	32.2	26.3	29.1	33.0

**Fig. 26:** Left: Scheme of an ionization chamber. Right: Its realization, with a 2 mm \times 3.2 mm active length in the beam direction.

The disadvantage of the plastic scintillators is the very low radiation hardness, owing to their complex organic molecular structure. Inorganic crystals have a much higher radiation hardness. In most cases, Ce-activated materials are used [17, 29]. However, these inorganic single-crystal scintillators are difficult to produce in larger sizes.

2.5.2 Ionization chamber

For the medium particle range, the current is determined by the energy loss of charged particles in a gas inside an ionization chamber. A general description of ionization chambers can be found in Refs. [17, 30]. Owing to the large statistics, the average energy for the production of an electron-ion pair is a well-known number, the so-called W values are given in Table 4. The arrangement of an ionization chamber is displayed in Fig. 26 and a photograph is displayed in Fig. 27. For this realization, the beam passes a 6.4 mm thick active gas volume and creates electron-ion pairs. In most cases, pure Ar is used, sometimes also mixed with about 10% of molecular gases, such as CH₄ or CO₂. The active gas volume is confined by metallized plastic foils or networks. These metallized electrodes are biased with about 1 kV, to separate the charges. The middle electrode measures the amount of secondary charge using a sensitive current amplifier. A secondary current down to the picoamp region can be measured precisely, see, e.g., Ref. [31]. The ionization chamber, filled with gas at atmospheric pressure, is separated from the vacuum by a metallic foil of typically 100 μ m thickness. The foil thickness must be low to prevent for significant energy loss in this foil. The specifications of the ionization chamber at GSI are given in Table 5.

With the help of the W values and the calculated energy loss dE/dx within an active length Δx , the number of primary ions I_{beam} is determined from the secondary current I_{sec} , as

$$I_{\text{sec}} = \frac{1}{W} \cdot \frac{dE}{dx} \Delta x \cdot I_{\text{beam}} \quad . \quad (18)$$

The precision of such a measurement depends mainly on the accuracy of the energy-loss calculation. For energies above 1 GeV/u, the value of dE/dx is only weakly dependent on the energy E ; see Fig. 14. When the energies of the beam particles are less than this, calibrations have to be made to reach an

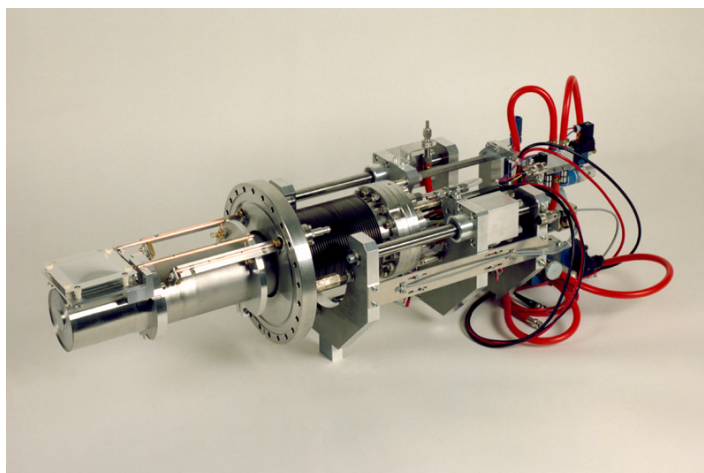


Fig. 27: Pneumatic drive mounted on a $\varnothing 200$ mm flange containing a scintillator and ionization chamber inside a pocket at atmospheric pressure and an SEM in a vacuum.

Table 5: Specifications of the ionization chamber at GSI

Parameter	Value
Active surface	$\varnothing 55$ mm
Active length	2 mm \times 3.2 mm
Electrode material	Plastic network
Coating	100 $\mu\text{g}/\text{cm}^2$ silver
Gas (flowing)	80 % Ar + 20 % CO_2
Pressure	1 bar
Voltage	500–2000 V

accuracy in the range of 1%. The ionization chamber can be calibrated with respect to a scintillator, where an absolute measurement is performed, as shown in Fig. 25. From the number of counted particles and the secondary current of the ionization chamber, a calibration factor can be determined, see, e.g., Ref. [28].

The lower limit of an ionization chamber is given by the minimum measurable secondary current, which is about 1 pA. Taking this current, the line in Fig. 21 is determined. The upper limit is based on the recombination of the electrons with the ions from the gas—for the case of Ar working gas, the reaction is $\text{Ar}^+ + e^- \rightarrow \text{Ar}$ —which is a sink for the generated charges. This is demonstrated in Fig. 28. We first discuss the characteristic line of the ionization chamber with a moderate primary current. The proportional region is reached after applying a moderate voltage of 500 V, corresponding to 1 kV/cm. The output is then independent of the voltage (or the applied electric field). The characteristic line is determined by comparison with the SEM (see next section) to obtain the efficiency. For a higher primary current, the plateau is no longer reached. A higher voltage cannot be applied without the risk of sparks. The drift time of the ions towards the electrodes depends on the applied electric field, while the drift time for the electrons is nearly constant for the given parameters [17]. The collision frequency of electrons and ions is proportional to their concentration n_e and n_i . The recombination rate is

$$\frac{dn_e}{dt} = \frac{dn_i}{dt} = \alpha \cdot n_e n_i \propto I_{\text{beam}}^2 \quad (19)$$

where α is the rate coefficient. The loss rate is therefore proportional to the square of the primary beam current. Typical values are summarized in Table 6. One can conclude that the secondary current for the

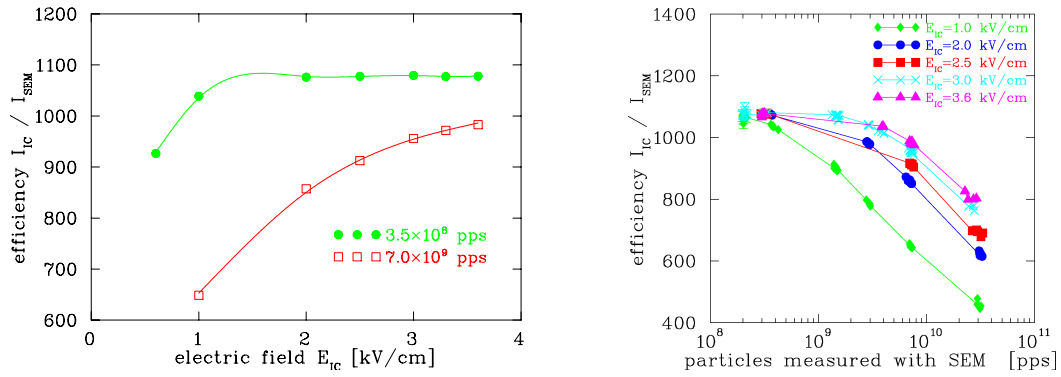


Fig. 28: Left: Characteristic line for ionization chamber, as determined for the 300 MeV/u Ne^{10+} beam. The efficiency is measured by the ratio of the secondary current of the ionization chamber and the SEM as a function of the applied electric field [27]. For a low primary current, a plateau is reached; for a high current, the recombination leads to a decrease of the secondary charges. Right: Comparable data shown as a function of transmitted ions per second for different applied electric fields.

Table 6: Properties of the ionization chamber close to the saturation point, see text

Parameter	Ions	Electrons
Drift velocity, w^{drift}	0.1 mm/ μs	20 mm/ μs
Drift time, t^{drift}	50 μs	0.1 μs
Saturation density, n^{sat}	$2 \times 10^9 \text{ cm}^{-3}$	$4 \times 10^6 \text{ cm}^{-3}$
Secondary current, I_{IC}	1 μA	
Dose rate, D_{IC}	30 Gy/s	
Average rate coefficient, α	$10^{-9} \text{ cm}^3/\text{s}$	

used ionization chamber should be below $\sim 1 \mu\text{A}$ for typical parameters, corresponding to a dose rate of about 30 Gy/s [27]. To obtain the value of the primary beam current, the conversion from the energy loss as given in Eq. 18 must be used.

To get a large upper threshold, the use of gases with high electron affinity, such as O_2 and H_2O , must be avoided [17]. The electron affinity describes the probability of an electron capture, e.g., $\text{O}_2 + e^- \rightarrow \text{O}_2^-$. The presence of negative ions enhances the recombination with positive ions, e.g., $\text{O}_2^- + \text{O}^+ \rightarrow \text{O}_3$, resulting in a smaller amount of measured secondary charge. In particular, an ionization chamber for high count rate applications should not contain air.

An ionization chamber can serve as a permanently installed monitor in front of the target for online beam current determination. The output signal from this ionization chamber can serve as the input for beam current control via a feedback circuit to control the amount of slowly extracted current. In particular, in a medical synchrotron delivering ions to a patient, the control of beam current by varying the amplitude of the transverse excitation power for a slow knock-out extraction has been realized [32–34].

2.5.3 Secondary electron multiplier

To cover the large current range from, e.g., slow extraction from a synchrotron, the emission of secondary electrons from a metallic surface can be determined using a secondary electron multiplier (SEM). Such a set-up is shown in Fig. 29, where three 100 μm thick aluminium foils are visible, installed on the vacuum side of the feed-through. The specifications of the SEM used at GSI are given in Table 7. The outer two foils are biased by typically +100 V to sweep out the free electrons. The middle foil is connected to a sensitive current amplifier. The secondary emission current depends on the energy loss at the surface,

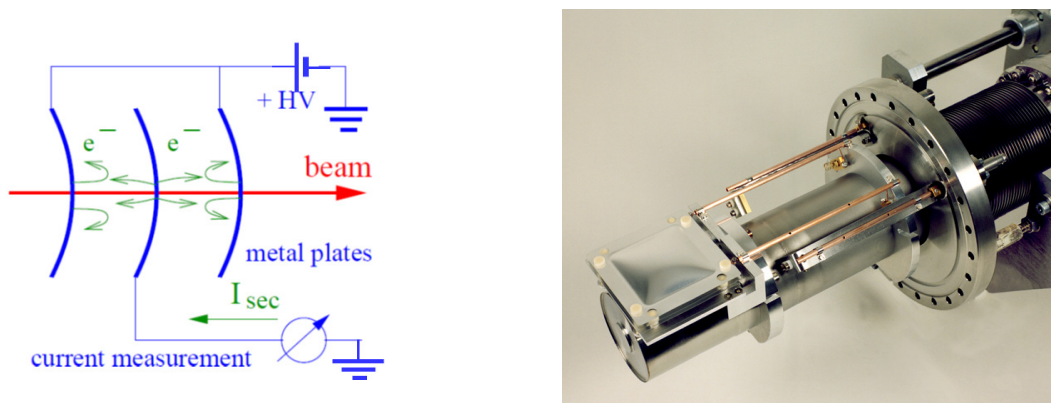


Fig. 29: Left: Scheme of a scanning electron monitor (SEM). Right: Photograph of the SEM part, made of three 100 μm thick aluminium foils, of the feed-through used for slow extraction current measurements at GSI.

Table 7: Specification of the SEM at GSI

Parameter	Value
Material	Pure Al ($\simeq 99.5\%$)
Thickness	100 μm
Number of electrodes	3
Active surface	$80 \times 80 \text{ mm}^2$
Distance between electrodes	5 mm
Voltage	100 V

$dE/\rho dx$, and is given by the Sternglass formula [24]

$$I_{\text{sec}} = Y \cdot \frac{dE}{\rho dx} \cdot I_{\text{beam}},$$

where Y is the yield factor describing the amount of secondary emission per unit of energy loss at the surface of the aluminium foil, see Eq. 16. Experimental calibration is required to determine the value of Y , yielding a precision of 5%, see, e.g., Ref. [28]. The accuracy is less than for an ionization chamber, because the actual value of the yield is determined by the surface structure of the material, which might vary, depending on the production and cleaning method. Equation 16 reflects the fact that the only electrons that are knocked out are those that are excited to the conducting band close to the surface of roughly $\simeq 10 \text{ nm}$; see Section 2.3.3 for a discussion of secondary electron emission. The physics of the secondary electron emission is also used for profile measurements, see Section 4.2.

Aluminium is often used because of its well-suited mechanical properties. In particular, it is stiff enough to prevent microphonic pick-up by external vibrations caused, e.g., by turbo vacuum pumps. However, the emission yield Y might change with irradiation. This is caused by modifications of the surface, which changes the work function and therefore the average yield Y . Measurements have shown a significant degradation, by a factor of two, after $10^{18} \text{ proton/cm}^2$ with 450 GeV protons at CERN SPS [35]. Here Ti foils have a much lower sensitivity to radiation. Radiation hardness is important, because these devices are often used in front of the target as a permanent current monitor.

3 Beam loss detection

In a real accelerator, the transmission from the source to the target is never 100%. The fraction of beam particles lost must be controlled carefully to achieve optimal transmission. The lost beam particles cause some activation of the accelerator components by nuclear reactions. Moreover, the surrounding material

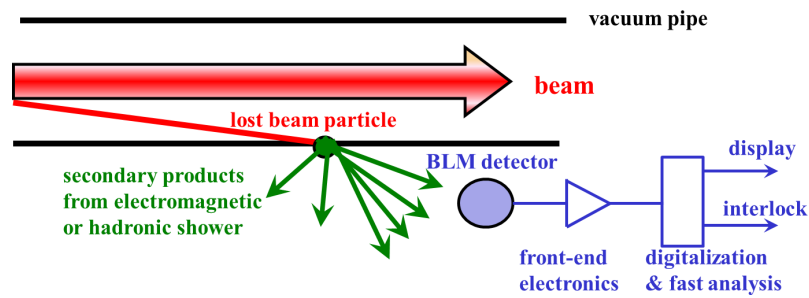


Fig. 30: Scheme for the installation of beam loss monitors outside a vacuum pipe

can be destroyed by the radiation, as well as by the heating due to the particles' energy loss. To detect the shower of secondary particles as originated by nuclear interaction processes, a large variety of beam loss monitors exists. Most of these are particle counters, detecting secondary reaction products. At nearly every high-current accelerator facility, these monitors are installed for the protection of the accelerator components. The relatively cheap beam loss monitor instruments are mounted outside of the vacuum pipe at crucial locations, as depicted schematically in Fig. 30. Their signals give important information to prevent unwanted loss during the operation, e.g., caused by malfunctions of components. A careful analysis of the location and time structure of possible losses must be performed before suitable types of beam loss monitors can be chosen; see Refs. [36–39] for reviews. Beam loss monitors can be sensitive devices, which detect even a very small fraction of losses; therefore, they are also used for machine tuning. Two examples are presented in Section 7.

3.1 Secondary particle production

When a high-energy particle hits a vacuum pipe, or any other material, secondary particles are generated. The relevant processes are described, e.g., in Refs. [40, 41]. Here only a brief overview is given.

- *Interaction of electrons.* For electron energies above ~ 100 MeV, Bremsstrahlung dominates the slow-down process in materials, as shown in Fig. 15. The created high-energy γ -photons give rise to further particles via e^+e^- pair production. If the energies of the γ -photons are high enough, other particles, e.g., μ^\pm , π^\pm , \dots , can also be produced, an electromagnetic shower is generated. Moreover, the nucleus can be excited to so-called giant resonances. This is a collective nuclear excitation, in which the neutrons oscillate against the protons. The dipole mode of these giant resonances has a threshold of about 6 MeV for typical materials. The de-excitation proceeds with high probability via neutron emission as a (γ, n) reaction. For higher energies, (γ, p) and (γ, np) channels are also open. When the electron is slowed down to below ~ 10 MeV, ionization loss by electronic stopping dominates, i.e., an electron vacancy is created at the atomic shell, which is then filled by an outer electron, leading to a soft X-ray emission. Those X-ray photons are absorbed within a short distance, from millimetres to centimetres in typical metals.
- *Interaction of protons.* Beside electronic stopping, as shown in Fig. 14, nuclear interactions are possible. First, we define the term ‘thick target’, when the interaction length is comparable to the range as given by the electronic stopping. In these thick targets, the probability of a nuclear reaction rises to nearly 100% for energies above 1 GeV, see Fig. 31. Most of the final channels of these nuclear reactions include neutron emission. As an example, for the stopping of 1 GeV protons in copper or iron, ~ 10 fast neutrons are liberated. The neutron yield scales approximately with E_{kin} for energies above 1 GeV. In addition, hadron showers (by the strong interaction at the quark level) are possible, resulting in various species of ‘elementary’ particles.
- *Interaction of ions.* Beside the interactions also valid for the protons, an ionic projectile can be induced by fragmented or fission, leading to radioactive nuclei and fast proton and neutron emission.

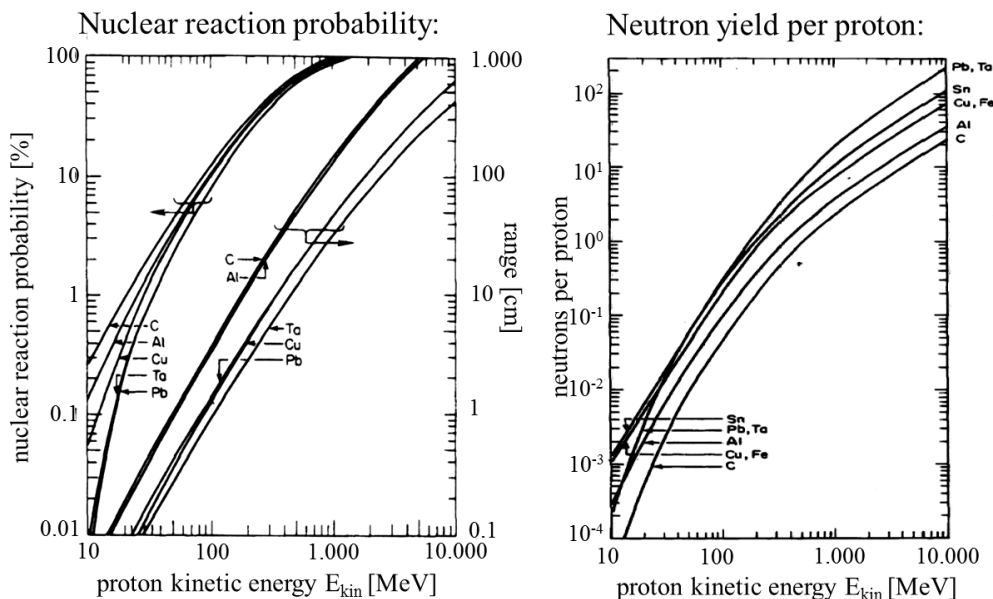


Fig. 31: Left: Ranges of protons in various metals and the probability of an inelastic nuclear reaction within the range as a function of the proton energy, i.e., within a thick target. Right: Total number of neutrons per proton incident on a thick target of various metals as a function of the proton energy [41].

Simple scaling laws do not exist, owing to the complex nuclear physics involved.

Common to all interactions is the production of radioactive nuclei, leading to activation of the accelerator components. The emitted charged particles are stopped relatively quickly by the surrounding material but the neutrons, produced by most primary interactions, can travel long distances. Some beam loss monitors are therefore sensitive to these neutrons. Except for the production of radioactive nuclei, all processes are fast, compared with the timescale of interest in accelerator physics, i.e., faster than ~ 10 ns. In this sense, a beam loss monitor reacts promptly to particle loss. Owing to the kinematics of the primary interaction, the secondary particles are emitted in a (more or less) forwardly peaked angular distribution. This leads to a spatial resolution of the loss detection by the monitor position close to the loss point.

3.2 Types of beam loss monitor

The task for beam loss monitors is to determine the position and time of the loss. Their signals should be proportional to the amount of loss at this position. A high sensitivity is needed to measure small losses. A high dynamic range is required to deal with a sudden loss of a sizeable fraction of the beam. Depending on the application, a bunch-to-bunch resolution on a ~ 10 ns time scale is needed, as well as up to 100 ms for a slow detection. All loss monitors are installed outside of the vacuum pipe, detecting mostly secondary particles. These can be neutrons, which are not much absorbed by the surrounding material, charged particles, such as protons, e^- or e^+ , or γ -rays. Figure 32 shows some frequently used types of beam loss monitor, as tested at the GSI synchrotron. An overview of the different types is given in Ref. [39].

3.2.1 Plastic scintillators

Plastic scintillators detect charged particles through electronic stopping, as discussed in Section 2.5.1. γ -rays are detected as they liberate electrons from the molecules via the photo effect or Compton scattering; those electrons generate optical photons through electronic stopping. Moreover, plastic scintillators are also sensitive to neutrons, owing to their elastic scattering on the hydrogen atoms of the polymers [17]. Owing to the elastic scattering process generated by the relativistic neutrons, a large momentum transfer

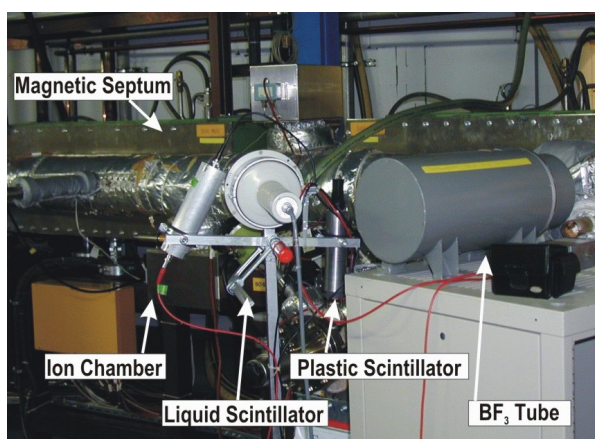


Fig. 32: Tested beam loss detectors installed at the extraction from the GSI heavy-ion synchrotron [42]

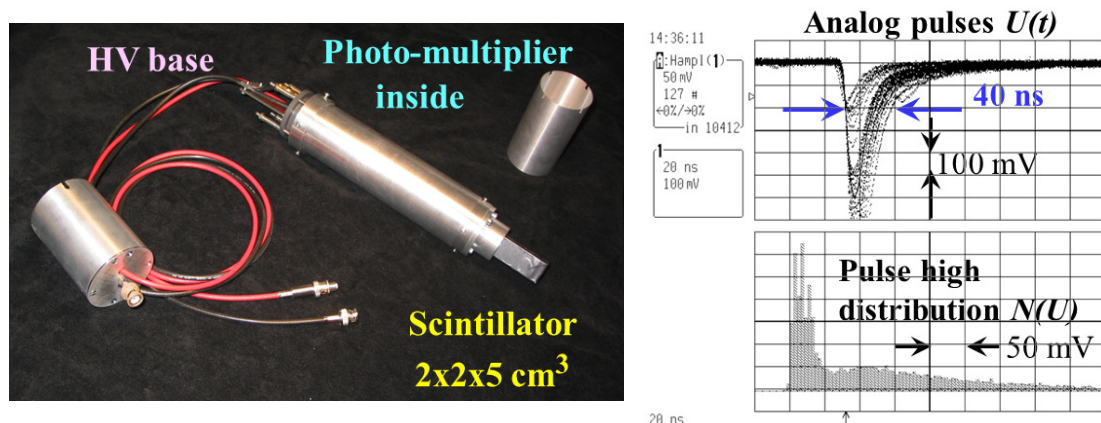


Fig. 33: Left: Typical beam loss monitor based on a plastic scintillator connected to a photomultiplier. Right: Typical pulses from a plastic scintillator (top, 100 mV/division and 20 ns/division) and their pulse height distribution (bottom, 50 mV/division), as measured at the GSI heavy-ion synchrotron.

to the hydrogen atoms of the macromolecules is probable, which leads to a fast proton travelling through the scintillator material and finally generating light emission through electronic stopping. The light is guided to a photomultiplier, converted to electrons, and amplified; see Fig. 33 for a typical realization. The resulting electronic signal can be read out by digitizing the analogue voltage using a relatively small photomultiplier gain, or a particle-counting mode can be used for higher sensitivity and larger dynamic range. A typical output for the counting mode is shown in Fig. 33, which shows analogue pulses of ~ 10 ns duration. Owing to the wide spectrum of incoming particle species and related energies, the pulse height distribution is quite broad. (This should be compared with the narrow pulse height distribution of single energetic particles shown in Fig. 24.) In the counting mode, the plastic scintillators have a very large dynamic range, from single-particle counting up to a count rate of 10^7 s⁻¹. In most cases, the scintillation monitors are located in crucial areas, such as injection or extraction devices, or close to scrapers. The disadvantage is the low radiation hardness of the plastic materials, owing to the complex chemical composition of the polymers from the plastic matrix. A very approximate number of the destruction threshold is given by the dose $D = 1$ Mrad = 10^4 Gy, where the light transmission is reduced by a factor $1/e = 0.37$. Typical plastic scintillators are cylindrical rods of 2 cm diameter and 10 cm length. Sometimes, long fibres of plastic or inorganic materials are used.

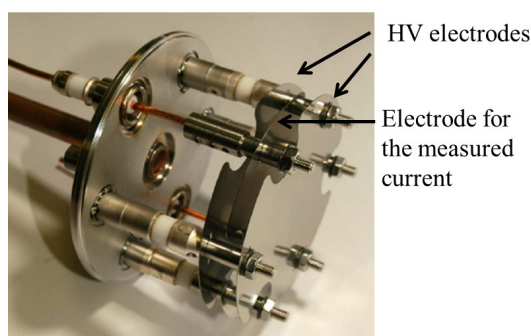


Fig. 34: Three plate SEM beam loss monitor [43,44]

3.2.2 *Liquid scintillator*

A scintillator material within a liquid solvent of about one litre is used [17]. The device is also sensitive to charged particles, e^{\pm} , γ -rays and neutrons through the same mechanisms as plastic scintillators. A comparable pulse height distribution is observed. The pulse length of the scintillation process is about one order of magnitude longer; therefore, the dynamic range is a factor of ten less for the counting mode. Owing to the microscopic light creation, γ -rays and neutrons can be discriminated using special electronics and so-called pulse shape discrimination [17]. The liquid is about a factor of ten more radiation hard than the plastics, owing to the simpler chemical composition of the solvent.

3.2.3 *Secondary electron multiplier and secondary electron multiplier*

An aluminium-coated electron multiplier is an electron multiplier in which the photocathode is replaced by an aluminium surface. Secondary electrons are liberated by the interaction with the radiation and amplified by the dynodes. This device offers a fast rise time and high dynamic range, but the sensitivity is much lower than that of scintillators.

If the loss rate is very large, the current of secondary electrons from a surface is large enough to be measured directly. This can be realized using a secondary electron multiplier with three plates installed in a small vacuum vessel [43,44]. The outer plates are biased by some +100 V and the secondary electron current emitted from the central plate is measured by a transimpedance amplifier or a current-to-frequency converter. The inner part of such a monitor is shown in Fig. 34. Relevant simulations and tests of the response to different radiation are reported in Refs. [43,44].

3.2.4 *PIN diode*

Solid-state detectors can be used as particle counters. In the typically 100 μm thick depletion layer of the doped Si-crystal, electron-hole pairs are generated. For a minimum ionizing particle, say, a charged proton at the minimum of its electronic stopping power, about 10^4 electron-hole pairs are generated. This signal must be amplified by a charge-sensitive pre-amplifier and can then be counted. As depicted in Fig. 35, two face-to-face mounted PIN diodes are used in coincidence to count only the charged particles and not the low-energy photons, as emitted at electron accelerators by synchrotron radiation. These photons are absorbed in one PIN diode and do not arrive at the second. The detection efficiency is relatively low, owing to the small active area, typically $10 \times 10 \text{ mm}^2$, and the 0.1 mm depletion depth. A device made of two PIN diodes including the amplifier and the counter is commercially available [11]; these are often installed at synchrotron light sources.

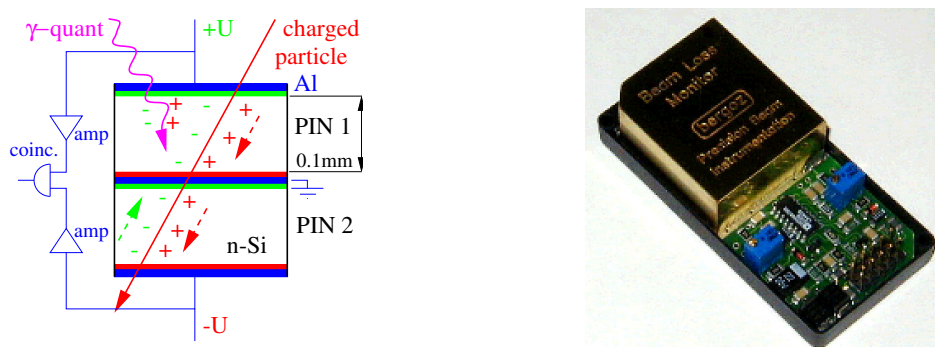


Fig. 35: Scheme of two PIN diodes driven in coincidence and photograph of the device [11]

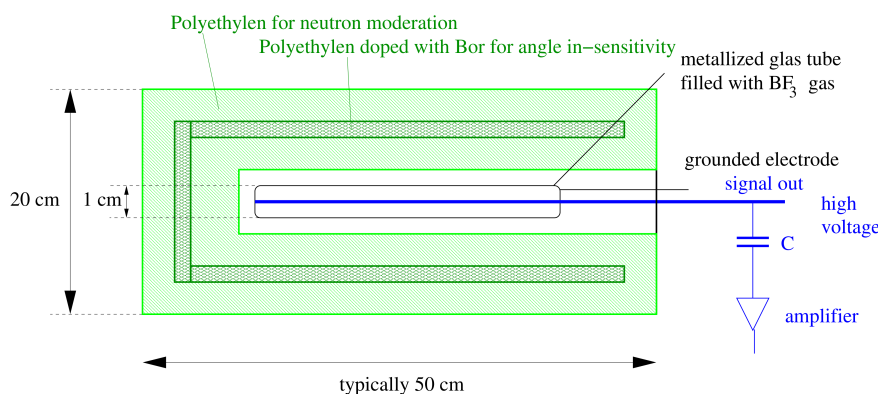


Fig. 36: BF_3 proportional tube as used for beam loss detection. The proportional tube is filled with BF_3 gas surrounded by polyethylene for neutron moderation.

3.2.5 BF_3 proportional tube

To have the possibility of measuring only neutrons, a cylindrical proportional tube (typical diameter, 10 mm and length 500 mm) filled with BF_3 gas can be used [17], as shown in Fig. 36. For thermal neutrons, the reaction $^{10}\text{B} + \text{n} \rightarrow ^7\text{Li} + \alpha$ has a high cross-section (~ 1 kbarn) and is exothermic by a Q value (total kinetic energies of Li and α) of 2.3 MeV. The gas-filled tube is surrounded by concentric layers of polyethylene, with an outer diameter of ~ 200 mm. The neutrons from the primary beam interaction are slowed down by elastic collisions with the hydrogen nuclei of the polyethylene. Special precautions are taken to obtain a flat detection efficiency as a function of the angle. Normally, these detectors are used at nuclear power plants for neutrons with energies of up to 10 MeV, but the thermalization yield of the neutrons can be extrapolated at least up to 100 MeV. In the traditional application, the glass tube is operated as a proportional tube; the count rate is limited to several 10^4 s^{-1} , owing to the time needed to recharge the inner wire of the proportional tube. Instead of the BF_3 working gas, comparable types are used, except filled with ^3He , having a comparable cross-section of thermal neutron absorption by the reaction $^3_2\text{He} + \text{n} \rightarrow ^3_1\text{H} + ^1_1\text{H}$ [17].

3.2.6 Ionization chamber

An ionization chamber measures the amount of secondary charges created in a gas volume, see also Section 2.5.2. Figure 37 shows such a round ionization chamber filled with Ar or N_2 gas. Typically, a sealed glass or metal tube contains $\sim 100\text{--}1000 \text{ cm}^3$ of gas between an outer high-voltage electrode and an inner grounded and readout electrode [45, 46]. The output current is measured using a sensitive current-to-voltage or current-to-frequency converter [47]. The ionization chamber is not sensitive to neu-

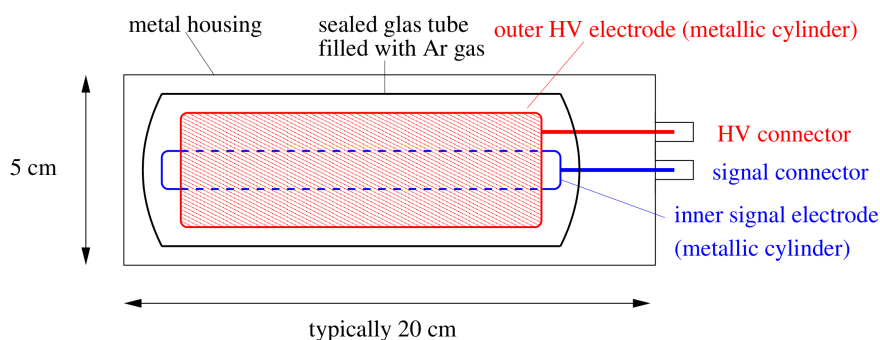


Fig. 37: Co-axial ionization chamber, as used for beam loss detection

Table 8: Basic parameters for the so-called RHIC-type co-axial ionization chamber [45,46] and the planar LHC-type ionization chamber [48,49].

Parameter	Co-axial ionization chamber	Planar ionization chamber
Outer length & diameter [cm]	20 & 6	50 & 9
Active gas volume [l]	0.11	1.5
Gas type & pressure [bar]	Ar & 1.1	N ₂ & 1.1
Number of electrodes	2	61
Distance of electrodes [mm]	$\varnothing_{\text{inner}} = 6.3, \varnothing_{\text{outer}} = 38$	5.7
Voltage [kV]	1	1.5
Reaction time [μs]	$\simeq 3$	$\simeq 0.3$

trons and has a low detection efficiency for γ -rays; mainly charged hadrons and e^{\pm} are detectable. By definition, the signal strength gives the absorbed dose in Gy directly. Because an inert, rare gas, such as Ar, or diatomic gas, such as N₂, is used in the detection volume, the device is very radiation hard. The signal strength is orders of magnitude less than for detectors in a particle-counting mode. Figure 37 depicts the scheme of a co-axial ionization chamber. For this geometry, the ionization chamber does not react as quickly as the scintillators, because the gas ions, created by the radiation, need $\sim 10 \mu\text{s}$ to reach the electrode. This time constant leads to a convolution of the primary signal, which is acceptable for most applications. The readout of the ionization chamber current by the digital electronics is therefore not faster than 1 ms in typical applications. The important parameters for such an ionization chamber are summarized in Table 8. A typical installation of a co-axial ionization chamber at an accelerator beam line or synchrotron is depicted in Fig. 38.

The detection threshold of an ionization chamber is proportional to the gas volume. To achieve a fast reaction time, even for a large gas volume, the drift time of the gas ions and electrons should be reduced. This can be realized by a parallel electrode arrangement with alternating biased and readout electrodes. Such an ionization chamber is shown in Fig. 39, as installed at CERN LHC and other facilities. About 4000 beam loss monitors are installed along the 27 km long LHC, corresponding to an average distance of about 6 m. They serve as the main detectors for beam protection and can trigger a fast abort. The design of such ionization chamber for LHC and relevant simulations concerning the response to various radiation species are discussed, e.g., in Refs. [48,49].

3.2.7 Comparison of different beam loss monitors

Several of the described types of beam loss monitor are tested at the extraction septum magnets at the GSI synchrotron [42]. A typical example is shown in Fig. 40 for a O⁸⁺ beam of 800 MeV/u extracted; the maximum number of stored particles was 4×10^{10} . The linearity of the different detectors is checked

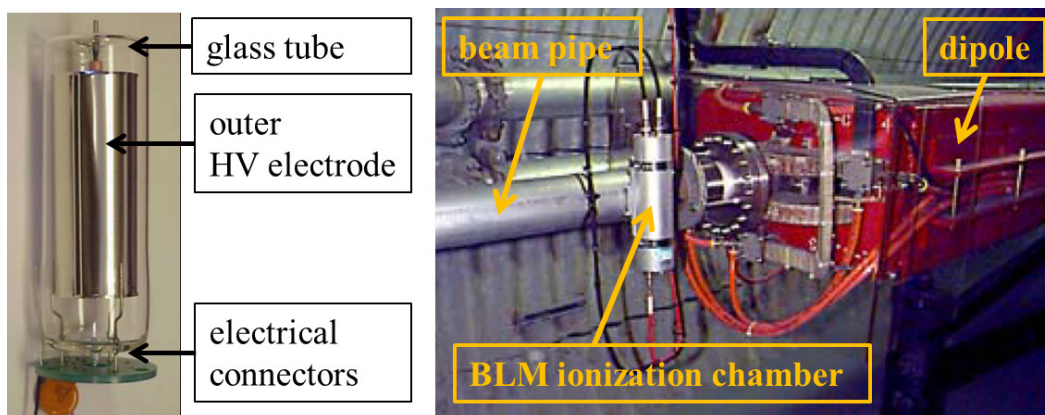


Fig. 38: Left: A 15 cm long co-axial ionization chamber used as a beam loss monitor (BLM). Right: Installation of such a ionization chamber for beam loss detection in a transport line.

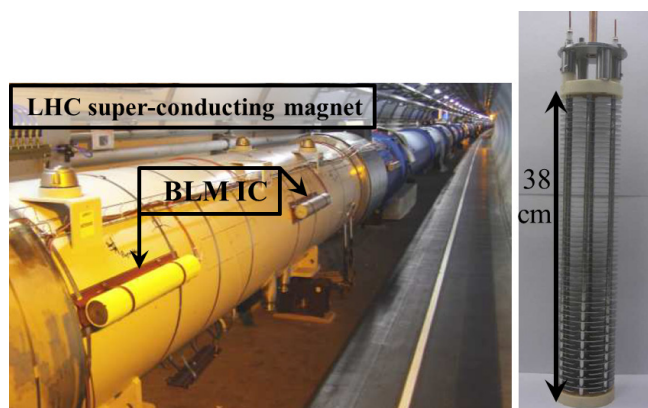


Fig. 39: Installation of a 50 cm long ionization chamber comprising 61 parallel plates at CERN LHC [48, 49]

by plotting the total counts for one spill as a function of the current detected at the experiment. The count rates obtained using the different types of monitor are quite different. The plastic scintillator shows the largest rate, about a factor of 30 greater than the BF_3 -tube, owing to the detection of more categories of secondary particles. The liquid scintillator shows a smaller rate; the saturation for the highest rate is due to the slow-integrating pre-amplifier. The signal strength of the ionization chamber is smaller by a factor of 200 than that of the plastic scintillator. The dynamic range is highest for the plastic scintillator. Results for the PIN diode are not shown here, but the count rate would have been about three orders of magnitude less than that of the plastic scintillator. The choice of beam loss monitor type for a given range of beam parameters is therefore mainly driven by the expected count rate for a given beam loss scenario and the expected composition of the secondary particles.

3.3 Machine protection using beam loss detectors

The most frequent application of beam loss monitors is the protection of accelerator components. The high energy stored in the beam can lead to the damage of surrounding materials. In particular, the vacuum pipe can be destroyed by the temperature increase due to the energy release of the particles, leading to a vacuum leakage. Moreover, other materials, like electrical feed-through connections, the insulation of magnet coils or any electronic devices, can be destroyed as a result of the modification of their material by the radiation. As discussed in Section 3.1, nuclear interaction leads to radioactive nuclei, which have lifetimes of hours or longer. This results in activation of the accelerator components, preventing access

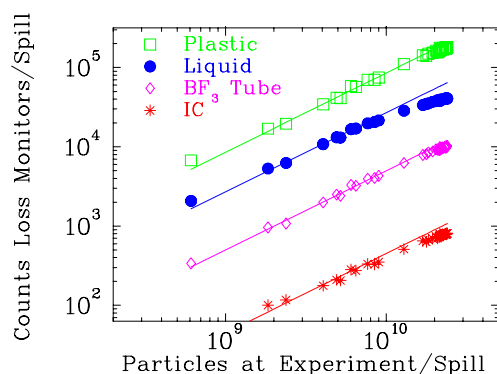


Fig. 40: Comparison of different beam loss monitors as a function of beam delivered to the target current for a O^{8+} beam of 800 MeV/u during slow extraction [42]. The lines are linear fits.

to the accelerator tunnel and strongly hampering maintenance. As a general rule, the power dissipation of the beam losses should be below 1 W/m to enable ‘hands-on maintenance’.

Another important application of beam loss monitors is the quench protection of superconducting magnets and cavities. Even a small amount of loss can heat up the superconducting material to above the critical temperature, causing a quench, i.e., a transition to normal conductivity. This dangerous situation is always controlled by loss monitors. They create an interlock: as soon as a critical count rate or dose is reached, the beam is immediately kicked out of the accelerator. The design criteria of an interlock system are discussed in Ref. [47]. Last but not least, the reason for reducing losses is protection of the environment and an efficient transfer of particles to the experiment. In the control room of most high-current accelerator facilities, the loss rate at sensitive locations is monitored online to visualize the full functionality of the machine.

We discuss briefly two categories of loss.

- *Irregular or fast losses* occur because of malfunctions of accelerator devices, e.g., magnets or RF cavities of power supplies. Such a malfunction leads to a beam with wrong parameters and subsequently the loss of part or all of the beam particles. Moreover, a misalignment of the device settings (e.g., the beam is not centred inside a quadrupole leading to steering, or a wrong RF cavity phase or amplitude produces a beam with the wrong kinetic energy) results in a mismatch of beam at the subsequent stages of the accelerator and part of the beam might be lost. The task of the beam loss monitors is to localize these losses, warning the operator or triggering an interlock to stop beam delivery.
- *Regular or slow losses* are known losses, e.g., at aperture limits of a collimator system, or losses due to the finite lifetime of the beam in a synchrotron. Most of these are unavoidable, but an increase in the loss rate indicates a malfunction. In addition, beam loss monitors can be used to find the appropriate parameters, e.g., for an emittance-reducing collimator.

It is obvious, particularly from the first item, that a beam loss monitor system should have a high sensitivity as well as a very large dynamic range. The high sensitivity is necessary to produce a usable signal when only a very small fraction of the beam is lost. Using scintillators or PIN diodes, single-particle counting can be performed with a very low detection threshold. Detecting the lost particles directly gives a much higher sensitivity than looking at the lost fraction of the total signal using a current transformer. The high dynamic range is mainly necessary for the detection of irregular losses, because the losses at one location can easily vary by several orders of magnitude, e.g., due to a power failure of a magnet or cavity. The monitoring has to be operated over several orders of magnitude concerning the signal strength without changing the full-scale range, to prevent saturation of the signal for large losses.

Here, a particle-counting mode delivers this high dynamic for rates ranging from 10 s^{-1} to 10^7 s^{-1} . Close to a collimator, scintillators offer a high dynamic range, which is needed for sensitive detection of the tails in the transverse particle distribution. For other regular losses, the required dynamic range is not so large, owing to the slower time variation. Ionization chambers are often installed for those applications.

Beam loss monitors are relatively cheap instruments and are installed outside the vacuum pipe, see Fig. 32. At most facilities, they are mounted at many locations along the accelerator to give good spatial coverage. The required time resolution depends very much on the application. To resolve the properties of individual bunches, fast-responding detectors (reaction time less than 100 ns), such as scintillators or PIN diodes, are necessary. Ionization chambers are much slower, having, in combination with the connected analogue and digital electronics, only $\sim 10\text{ }\mu\text{s}$ time response. However, ionization chambers offer direct determination of dose and are therefore often installed for machine protection systems.

The positions of the beam loss monitors should be well chosen. For greatest sensitivity, the distribution of the secondary particles should be a maximum at this location. The secondary particle distribution must be calculated using an adequate software code. For high energies, the well-known code GÉANT [50] is used in most cases. A loss of beam particles at a quadrupole is assumed in many cases because the beam has the largest width there. Because of the alternating focusing, the differences in the horizontal and vertical beam widths offers the possibility of distinguishing between horizontal and vertical losses. Moreover, monitors are often installed at insertions that limit the acceptance, such as injection of extraction septa.

3.4 Beam loss monitoring for beam alignment

Beam loss monitors have two main advantages, namely the high sensitivity and the fact that these monitors can be installed at many locations. For beam alignment at critical positions with small beam pipes, beam loss monitors can be mounted densely. An example for the slow extraction at the GSI synchrotron is shown in Fig. 41. Here, the septum elements, used to kick the beam, have small pipe diameters, comparable to the actual beam size. If the angle at the input of the septum magnets is slightly wrong, part of the beam is lost there. Therefore, the angle kick at the first element (here the electrostatic septum) must be aligned carefully in small steps to find the minimal loss rate. Using beam loss monitors, the alignment procedure can be executed with more sensitive input signals than by monitoring the transmitted current, as demonstrated by the top curve in Fig. 41. Beam loss monitors can serve as a basic tool for daily operation. Beam loss monitors are also useful for the time-dependent monitoring of a possible misalignment at different sections of a synchrotron or a transfer line, e.g., during slow extraction, because they can be installed at several critical locations. At some linac-based facilities, beam loss monitors are used as the operation tool for transmission optimization, owing to their high sensitivity, which might be greater than achievable by measuring the transmitted beam via current transformers, see, e.g., Ref. [51].

4 Measurement of beam profile

The beam profile can be influenced by quadrupole magnets installed in all accelerating structures and in transfer lines. Measurement is important to control the beam width, as well as transverse matching between different parts of an accelerating facility. The large number of bending, focusing, and correction magnets gives rise to the need for many profile measurement stations. Depending on the beam particles, current, and energy, a very large variety of devices exists. We can only briefly discuss the most popular ones. The beam spot can be observed directly by intercepting it with scintillator screens and viewing the emitted fluorescence with a camera. Secondary electron emission grids (SEM grids) are widely used as an electronic alternative to achieve a large dynamic range; a grid of wires with typically 1 mm spacing is inserted. Instead of a fixed grid, a single wire can be scanned through the beam to give high spatial resolution; this is called a wire scanner. A third approach is a so-called ionization profile monitor, in which the ionization products of the interaction of the beam with the residual gas atoms or molecules inside the

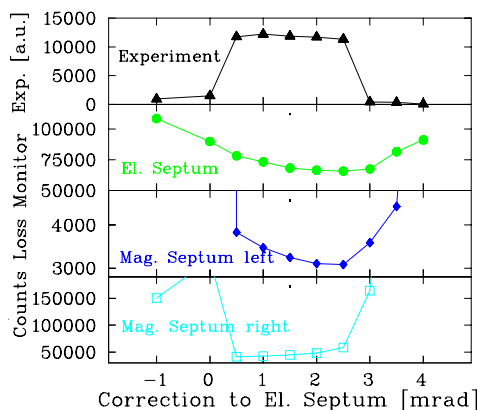


Fig. 41: Counts per spill from three loss monitor locations and the current at the experiment as a function of the angle electrostatic septum at the GSI synchrotron [42].

(imperfect) vacuum of the tube are detected. In these devices, the resulting electrons or ions are accelerated by an external electrical field to a detector with a spatial resolution. The ionization profile monitor is well-suited as a non-destructive method for a synchrotron. When charged particles with relativistic velocities pass through a metallic foil, radiation is emitted, as described by classical electrodynamics; this process is called optical transition radiation. This light is recorded by a camera to determine the beam profile. High-energy electrons emit synchrotron radiation if the trajectory is curved. Monitoring this light by synchrotron radiation monitors yields direct information about the beam spot.

Normally, the diameter of an electron beam is less than 1 mm, while proton or heavy-ion beams have large diameters, up to some centimetres. In particular, in a synchrotron with multiturn injection, diameters of several centimetres can be produced.

The beam width is mainly given by the settings of the focusing magnets and the beam emittance ϵ . Knowing the lattice, i.e., the β function $\beta(s)$ and the dispersion $D(s)$ at the monitor location s , the measured beam width $\sigma(s)$ is given by

$$\sigma_x^2(s) = \epsilon_x \beta_x(s) + \left(D(s) \frac{\Delta p}{p} \right)^2 \quad \text{and} \quad \sigma_y^2(s) = \epsilon_y \beta_y(s). \quad (20)$$

In a synchrotron, the lattice functions are well-known, or can be measured separately. If the momentum spread $\Delta p/p$ is also known, the emittance can be calculated. (In the vertical direction, the dispersion is zero in most cases, because only horizontal bending magnets are used.) Nevertheless, the contribution due to the dispersion must be taken into account for the interpretation of the beam width. In a linac, the lattice functions are not so precisely fixed, owing to the variable input emittance orientation, leading to a less stringent relation between profile width and emittance.

4.1 Scintillation screen

The most direct method of beam observation involves recording the light emitted from a scintillation screen intersecting the beam, monitored by a commercial video, CMOS (complementary metal-oxide-semiconductor), or charge-coupled device (CCD) camera, see, e.g., Refs. [52–54] for an overview. These devices are installed in nearly all accelerators from the source up to the target. A scintillation screen is schematically shown in Fig. 42 together with a realization in which the pneumatic drive is mounted on a $\varnothing 200$ mm flange.

When a charged particle penetrates a material, the energy loss can be transformed to fluorescence light, as discussed in Section 2.5 for the scintillation counter. The important properties of such a scintillator are as follows.

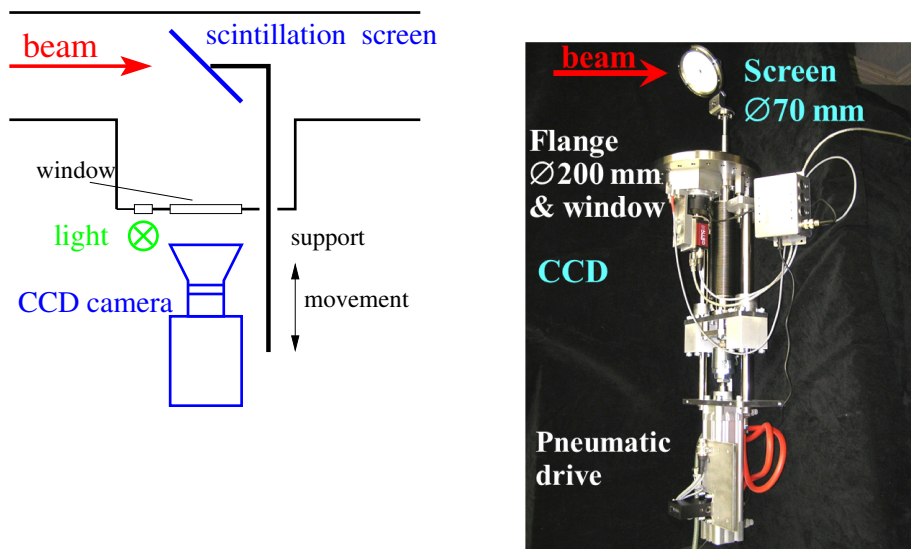


Fig. 42: Left: Intercepting scintillation screen. Right: A P43 phosphor scintillation screen of $\varnothing 70$ mm and CCD camera are mounted on a $\varnothing 200$ mm flange with pneumatic drive.

Table 9: Chemical composition and some basic optical properties of inorganic scintillation screens. The matrix Al_2O_3 is used in the form of a ceramic. The last four materials are so-called phosphor screens, where powder is deposited on glass or metal plates.

Material	Type	Composition	Activator	Maximum emission [nm]	Decay time
Quartz	Glass	SiO_2	None	470	<10 ns
Alumina	Ceramics	Al_2O_3	None	380	~ 10 ns
Chromox	Ceramics	Al_2O_3	Cr	700	~ 10 ms
YAG	Crystal	$\text{Y}_3\text{Al}_5\text{O}_{12}$	Ce	550	200 ns
LuAG	Crystal	$\text{Lu}_3\text{Al}_5\text{O}_{12}$	Ce	535	70 ns
Caesium iodide	Crystal	CsI	Tl	550	1 μs
P11	Powder	ZnS	Ag	450	3 ms
P43	Powder	$\text{Gd}_2\text{O}_2\text{S}$	Tb	545	1 ms
P46	Powder	$\text{Y}_3\text{Al}_5\text{O}_{12}$	Ce	530	300 ns
P47	Powder	$\text{Y}_2\text{Si}_5\text{O}_5$	Ce & Tb	400	100 ns

- High light output matched to the optical system of the camera in the optical wavelength range of $400 \text{ nm} < \lambda < 700 \text{ nm}$.
- High dynamic range, i.e., a good linearity between the incident particle flux and the light output. In particular, a possible saturation of the light gives rise to a deformation of the recorded profile.
- No absorption of the emitted light to prevent artificial broadening by stray light inside the material.
- No significant contributions from reflection at the surfaces of the scintillation light produced inside the material; depending on the geometry, this can lead to an artificial profile broadening. In this case, e.g., anti-reflex coating should be applied.
- Fast decay time, to enable the observation of possible variations of the beam size.
- Good mechanical properties for producing up to $\varnothing 100$ mm large screens.
- Radiation hardness to prevent permanent damage.

As stated, plastic scintillators have only low radiation hardness and various kinds of inorganic material are used instead. Some properties are given in Table 9 [52, 53]; for more details see Refs. [17, 29].

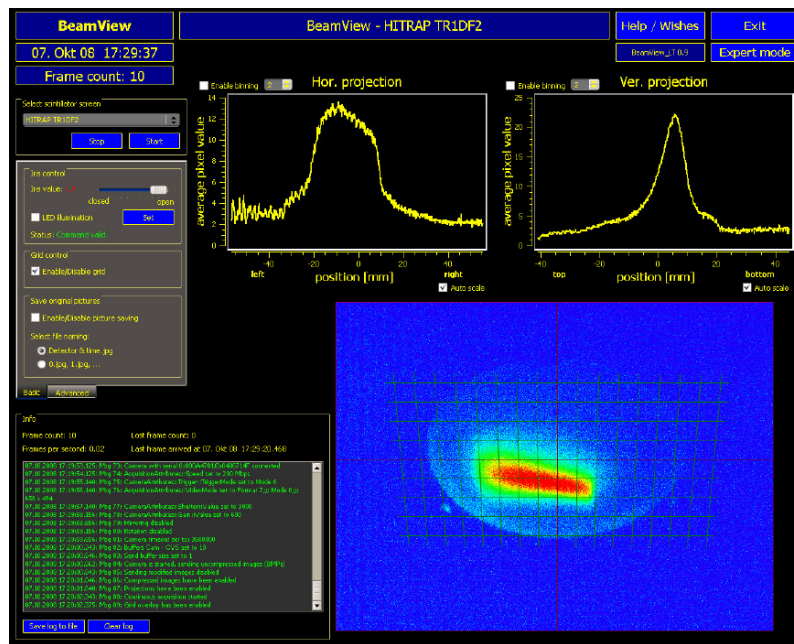


Fig. 43: Beam spot of low-current 4 MeV/u beam at GSI on a YAG:Ce screen recorded with a digital CCD camera. The original greyscale image is converted to false colour for better visibility. The projection on the horizontal and vertical axes are shown in the upper part. From Ref. [65].

The material Chromox is a ceramic, which can be fabricated like pure Al_2O_3 and used widely as an insulating material. The scintillation is due to the Cr activators; chemically, it is comparable to ruby. The disadvantages are its long decay time of ~ 10 ms and the large absorption inside the material. Nevertheless, owing to its robustness, it is quite often used. The well-known Ce-activated crystal materials, such as YAG ($\text{Y}_3\text{Al}_5\text{O}_{12}$) have better optical properties and are widely used for particle-counting applications [17]. However, it is difficult to produce crystalline discs of about 10 cm diameter from this material. Instead of the expensive single-crystal disc, one can use small grains of ~ 10 μm size, deposited on glass or metal discs that are several millimetres thick. These phosphor screens are also used very frequently in analogue oscilloscopes, electron microscopes, and image intensifiers. P46 is an example for a phosphor screen powder offering a much lower production cost compared with the chemically equivalent single-crystal YAG:Ce. The properties of doped materials depend strongly on the activator concentration; therefore, Table 9 gives only approximate values. The sensitivities of the different materials span several orders of magnitude and also depend on the particle species, see, e.g., Refs. [54–56]. Scintillation screens are used in all types of accelerators [54]; some examples of investigations are discussed for electron beam [57–60] and proton or ion [55, 56, 61–64] accelerators with quite different applications.

The beam image from a YAG:Ce screen is shown in Fig. 43 for a low-current beam of only $\sim 10^6$ ions at 4 MeV/u, proving the high sensitivity of that material.

For high-intensity beams, it must be ensured that the material is not destroyed by the absorbed beam power. In particular, for slow heavy ions with a range comparable to the screen thickness, this restricts the use; see also the discussion in Section 2.3. A disadvantage of the screen is related to the interception. The used material is so thick (several millimetres) that it causes a large energy loss, so that it cannot be used for the diagnostics of a circulating beam inside a synchrotron.

The screen is observed with a CCD or CMOS camera. A modern approach uses a digital link, with digital data transfer of the camera pixel values, enabling fast data rates for long cable lengths without

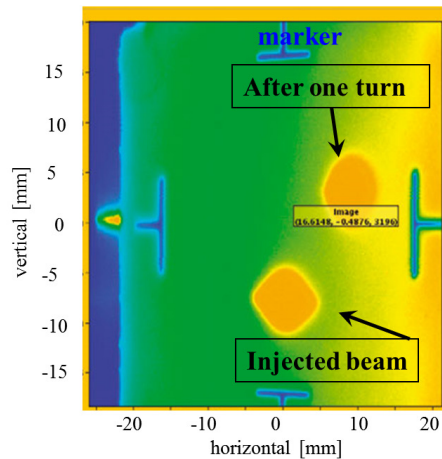


Fig. 44: Beam spot of injected beam and beam after one turn at LHC, recorded using a Chromox screen

signal degeneration, see, e.g., Ref. [65]. One problem is the radiation sensitivity of the CCD sensor and the digital equipment. At high levels of radiation, old-fashioned analogue vidicon cameras are used; in this case, the analogue video output is digitized by a frame grabber.

For alignment of the injected beam into a synchrotron, a so-called first-turn diagnostics unit is installed. After a one-turn passage, the beam hits a profile measurement device, in most cases a scintillation screen, to check for the beam properties after one turn (for this case, the synchrotron is more or less treated as a single-pass transfer line). In Fig. 44, a historically important example is depicted from the injection to the LHC, as recorded at the first day of its operation, in which a scintillation screen is installed just after the injection location to monitor the injected beam as well as the beam after one turn. For larger synchrotrons, such first-turn diagnostics are installed at several sectors. The profile diagnostics are often accompanied by the determination of beam current, using a Faraday cup for low-energy ions, a current transformer for multiturn injection or beam position monitor (BPM) readouts in a single-pass mode for single-turn bunch-to-bucket injection.

4.2 Secondary electron emission grid

When particles hit a surface, secondary electrons are knocked out from the surface, as described in Section 2.5.3. For the profile determination, individual wires or ribbons interact with the beam; this device is called a secondary electron emission grid or a harp, as reviewed in Ref. [66]. Each of the wires has an individual current-to-voltage amplifier. This is an electronic alternative to a scintillation screen with a much higher dynamic range, i.e., the ratio of minimal to maximal detectable current is orders of magnitude greater. W-Re alloys are often used for the metallic wires or flat ribbons, owing to their excellent refractory properties. This is particularly important for low-energy linacs because no cooling can be applied, owing to the geometry. A photograph of such a device is shown in Fig. 45; the specifications are given in Table 10.

For low energies at proton or heavy-ion linacs, the particles are stopped in the material or undergo significant energy loss. The diameter-to-spacing ratio of the wires determines the attenuation of the beam current (and, of course, also the signal strength on the individual wires). Typically, only 10% of the beam area is covered by the wires; in this sense, the profile measurement is nearly non-destructive. For energies above 1 GeV/u, the relative energy loss is negligible and large ribbons are used. A typical example of the SEM grid measurement used for beam optimization is shown in Fig. 46 for a transfer line.

Each wire has an individual pre-amplifier, in most cases an I/U converter, followed by a sample-and-hold circuit (Fig. 47). These electronics must be installed close to the accelerator hardware. With

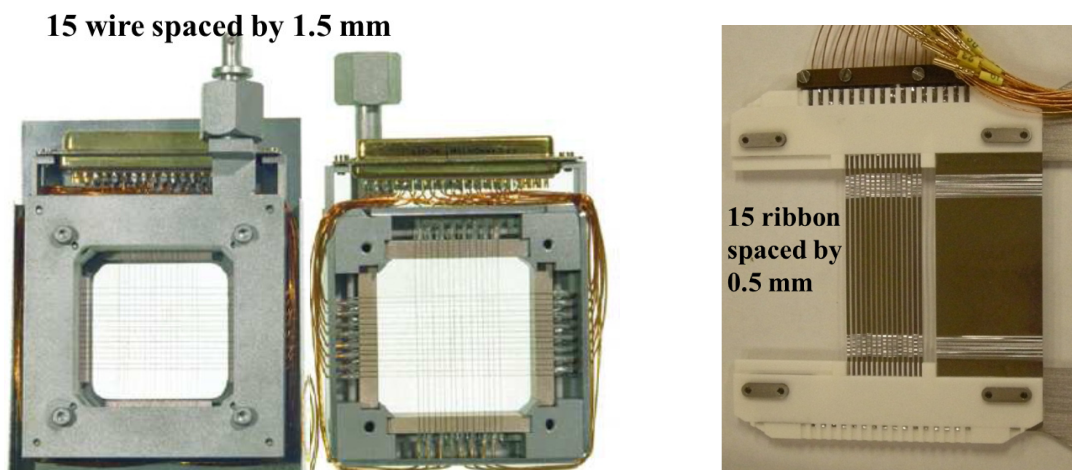


Fig. 45: Left: Secondary electron emission grid for both planes with 15 tungsten wires spaced by 1.5 mm as typically used at a proton linac. The individual wires are insulated with glass-ceramics. Middle: Same grid with tin cover removed. Right: Grid based on ribbons of 25 μm thick aluminium foil by laser cutting; the spacing is 0.5 mm. This type is used for high-energy protons, typically >1 GeV. The devices are mounted on a pneumatic drive to move them in and out of the beam (not shown).

Table 10: Typical specification for SEM grid used at proton and heavy-ion linacs

Parameter	Value
Diameter of the wires	0.05–0.5 mm
Spacing	0.5–2 mm
Length	50–100 mm
Material	W or W-Re alloy
Insulation of the frame	Glass or Al_2O_3
Number of wires	10–100
Maximum power rating in vacuum	1 W/mm
Minimum sensitivity of I/U conversion	1 nA/V
Dynamic range of electronics	$1:10^6$
Integration time	1 μs to 1 s

a multiplexer, the analogue values are transported to an analogue-to-digital converter (ADC) located outside the accelerator tunnel. Readout of a full SEM grid in less than a millisecond is typical for the use of pulsed or d.c. beams.

4.3 Wire scanner

Instead of using several wires with individual, expensive, electronics, a single wire can be swept through the beam [66]. The advantage is that the resolution is not limited by the wire spacing; therefore, this technique is often used in electron accelerators with beam sizes in the sub-millimetre range. It can also be applied in proton synchrotrons, owing to the small amount of intercepting matter.

An arrangement with a straight wire on a fast pendulum mechanics is shown in Fig. 48 [67, 68]. Scanning velocities up to 10 m/s can be achieved with a special pneumatic mechanism. Sometimes this set-up is also called a flying wire. Carbon or SiC is used as the wire material, owing to its low weight and low nuclear charge, Z , resulting in a low-energy deposition in the wire (the Bethe–Bloch equation (Eq. 13) gives $dE/dx \propto \rho \cdot Z/A$). In addition, these materials can withstand high temperatures without melting. The wire can be as thin as 10 μm . However, owing to the scanning of the single wire, the

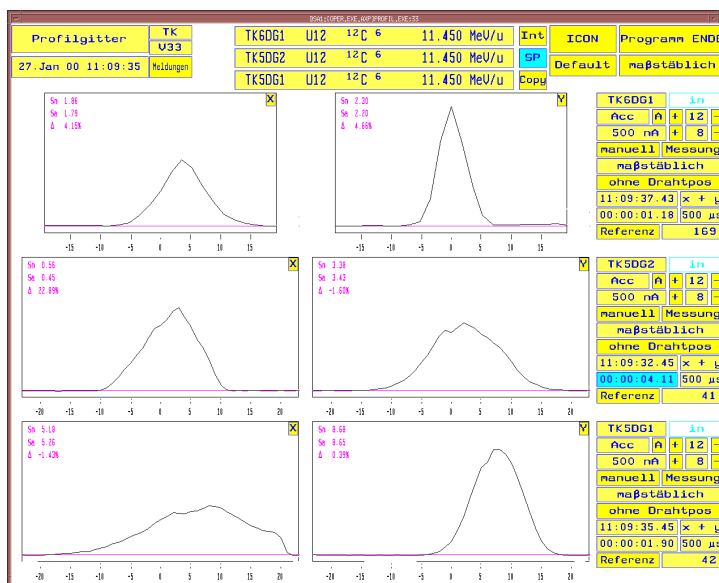


Fig. 46: Measured profiles [mm] of SEM grids in one transfer line at the GSI heavy-ion linac. Left: horizontal profile. Right: vertical profile.

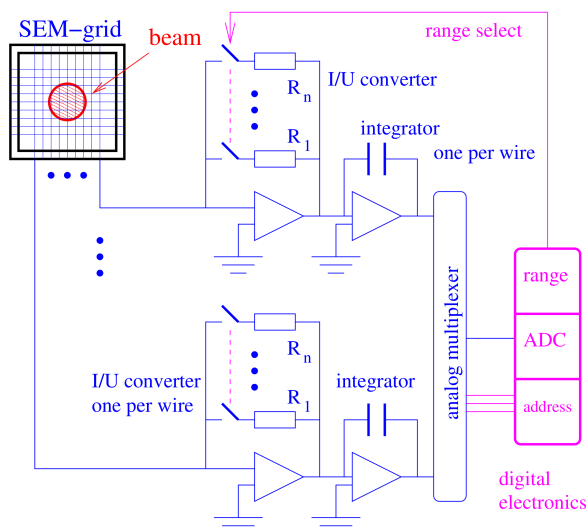


Fig. 47: Typical analogue signal processing for SEM grid

profile is not taken at a single instant, even at high scanning velocities. Therefore, only the steady-state distribution can be probed.

For profile display, the position of the wire, determined by the position encoder, is plotted along the horizontal axis. The beam signal for the vertical axis can be deduced from the current given by the emitted secondary electrons, as for a SEM grid. This is done, in particular, for low-energy protons and heavy ions. In most cases, for beam energies larger than 150 MeV/u for ions (the threshold for π -meson production) or 10 MeV for electrons, the signal is deduced by monitoring the secondary particles outside the beam pipe, see Fig. 49. These secondary particles might be hadrons created by the nuclear interaction of the proton or ion projectiles and the wire, having enough kinetic energy to leave the vacuum chamber. For the case of electron accelerators, the secondary particles are mainly Bremsstrahlung photons. The detector is simply a type of well-suited beam loss monitor, e.g., a scintillator installed several metres

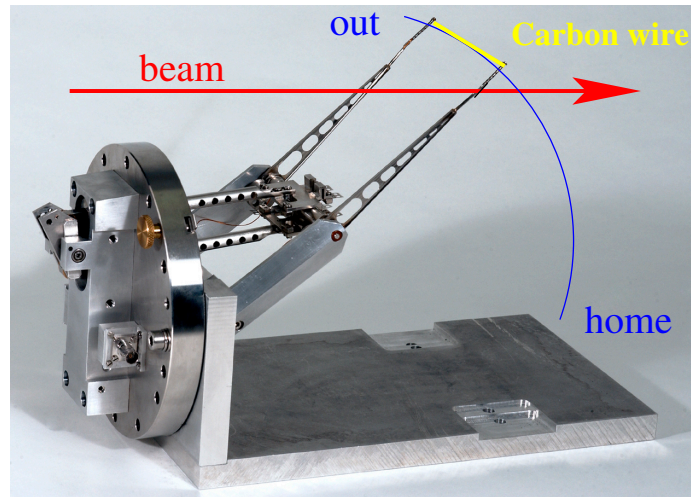


Fig. 48: Pendulum scanner or ‘flying wire’ used at CERN synchrotron [67]

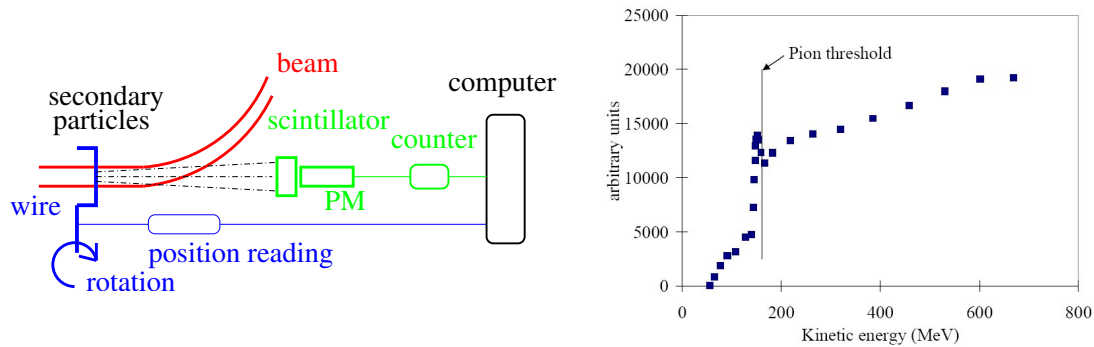


Fig. 49: Left: Scheme of wire scanner using the production of secondary particles as the signal source. Right: Total rate from wire scanner under proton impact at CERN PS-Booster, showing the rate increase above the π -threshold at ~ 150 MeV [69].

away (see also Section 3). The count rate is plotted as a function of the wire position, as a precise representation of the beam profile.

For fast movements, vibration of the wire restricts the spatial resolution. A much greater precision can be achieved using a much slower movement of, for example, only 0.1 m/s, with a linear drive, as shown in Fig. 50 [70]. With these types, a resolution of 1 μm is reached in electron accelerators [71]. To achieve this low beam width reading, σ_{beam} , for a Gaussian beam, the contribution of the wire (4 μm thick carbon wire in this case) must be deconvoluted from the measured width σ_{meas} according to

$$\sigma_{\text{beam}}^2 = \sigma_{\text{meas}}^2 - 4 \cdot r_{\text{wire}}^2 \quad . \quad (21)$$

In most cases, the wire is mounted on a fork, which is inserted into the beam pass by a drive mounted at 45° . Then only one drive is sufficient for measuring both transverse planes by mounting the wires in a crossed orientation, as shown in Fig. 50. If the signal generation is performed by reading the secondary emission current, two isolated wires can be mounted in a compact manner. If the signal is generated by beam loss monitors outside the beam pipe, the two wires must be separated (as shown in the left-hand panel of Fig. 50), so that the wires cross the beam one after the other.

A comparison of the wire scanner and the SEM grid shows the advantages and disadvantages of both types [66].

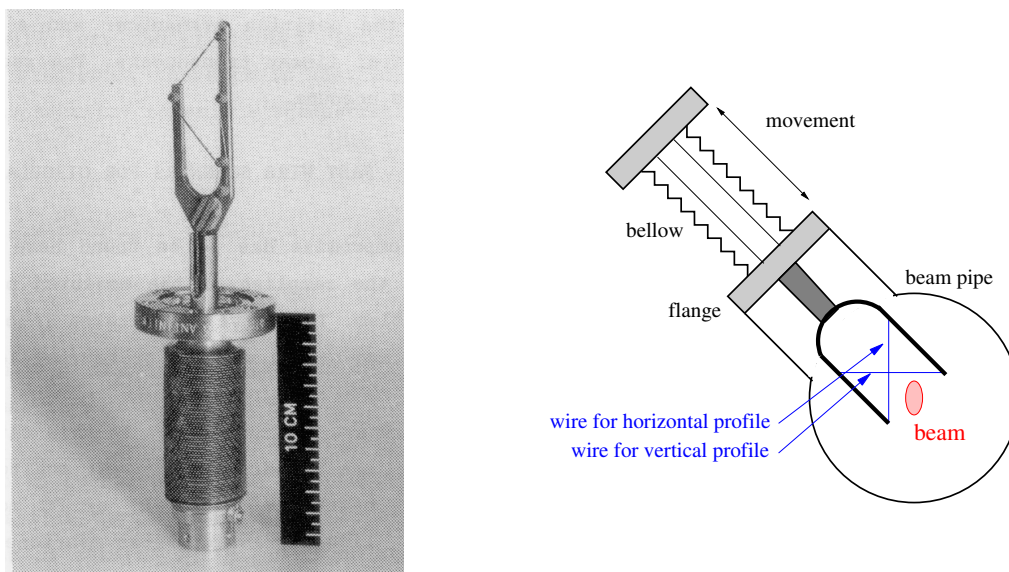


Fig. 50: Left: Linear scanner used at CERN [70]. Right: Schematics of the movement

- With a SEM grid, the beam intensity is sampled concurrently, whereas a moving wire samples the parts of the profile at different locations at different times. Therefore, variations of the beam intensity in time will be mixed with transverse intensity variations using a scanning device.
- In the case of pulsed beams, a synchronization between the readout of the electronics and the beam pulse is required, as well as a movement within the beam pulse. The synchronization between readout and beam pulse is more easy to achieve for a SEM grid.
- The resolution of a SEM grid is fixed by the wire spacing (typically 1 mm), while a wire scanner can have much higher resolution, down to 10 μm , owing to its constant movement. (For high resolution, mechanical vibration must be avoided.)
- The electronics for data acquisition are cheaper for a scanning system. A SEM grid requires one channel per wire.
- For the cost of the mechanics, it is the other way around: the precise vacuum actuator for the scanner is more expensive than the pneumatic drive needed for a SEM grid.

4.4 Multiwire proportional chamber

For slowly extracted beams from a synchrotron, the current is much too low to be measured using a SEM grid. One can use the amplification of electrons in a gas, as is done in a multiwire proportional chamber; for the principle of operation see, e.g., Ref. [17]. As discussed for the ionization chamber for current measurements in Section 2.5.2, the primary particles traverse a gas (such as 90% Ar mixed with 10% CH_4 or CO_2), creating secondary electrons. A multiwire proportional chamber consists of a grid held at a high voltage, typically several kilovolts, and a grounded grid, which is read by a charge-sensitive pre-amplifier, as for SEM grids. The distance between the anode and the cathode plane is typically 1 cm and the spacing of the wires about 1 mm. The principle is shown in Fig. 51. Close to the anode wires, typically of 25 μm diameter, the electrical field increases in proportion to $1/r$, see Fig. 52. After reaching a threshold, the energy of the electrons accelerated towards the wires is high enough to knock out additional electrons from the gas atoms or molecules. This gives rise to an avalanche, which results in a $\sim 10^4$ amplification in the number of electrons. This amplification inside the detector volume is nearly noise-free, owing to the high source electrical impedance of the free charge carriers. The resulting low noise could not be achieved by an electric amplifier, owing to its thermal noise. The following electronics

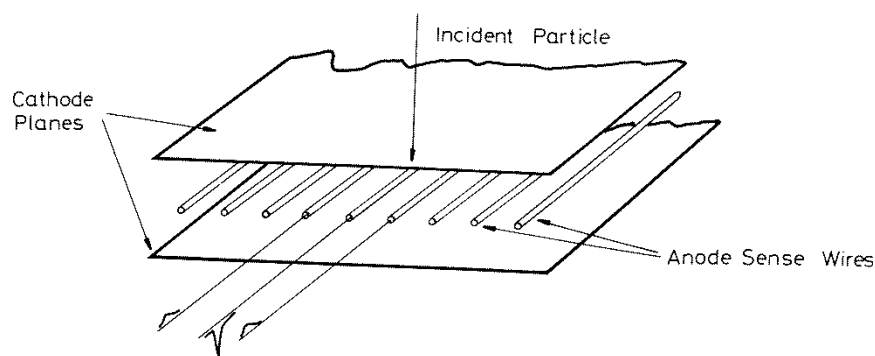


Fig. 51: Scheme of multiwire proportional chamber for one plane, showing signal generated by particle interaction

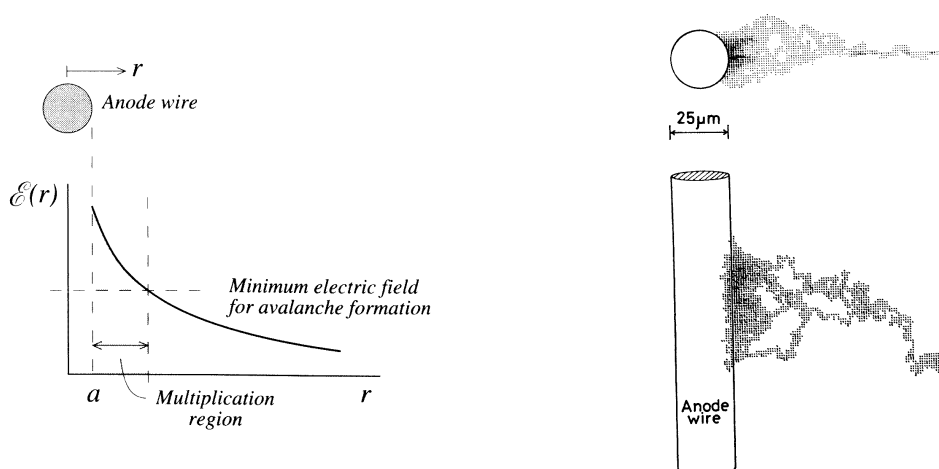


Fig. 52: Left: Electric field close to anode wires, showing amplification region. Right: Monte Carlo simulation showing electron avalanche as grey shading [72].

(further amplifier and ADC) and the display method are comparable to the procedure for SEM grids

An example of a multiwire proportional chamber used at GSI is shown in Fig. 53.

4.5 Ionization profile monitor

A frequently used non-destructive method for profile determination is the ionization profile monitor, sometimes also called the residual gas monitor. These monitors are installed in nearly every proton or heavy-ion synchrotron for the detection of beam sizes between some millimetres and several centimetres; a review is given in Ref. [73, 74]. They are seldom used for electron synchrotrons, owing to the smaller electron beam. The principle is based on the detection of the ionized products from a collision of the beam particles with residual gas atoms or molecules in the vacuum pipe. A scheme for such a monitor is shown in Fig. 54. Typical pressures for linacs and transfer lines are in the range 10^{-8} – 10^{-6} mbar, containing mainly N_2 and O_2 , and for synchrotrons are in the range 10^{-11} – 10^{-9} mbar, containing mainly H_2 ; the different compositions are due to the different vacuum pumps used. Owing to the electronic stopping process, electrons are liberated and electron–ion pairs are generated. An estimate of the signal strength can be obtained using the Bethe–Bloch formula. However, owing to the single collision behaviour, the W values (see Section 2.5.2) are only a first-order approximation for the conversion of the energy loss to the numbers of secondary particles; the process is better approximated by considering some 100 eV for the creation of an electron–ion pair. To separate the electron–ion pairs, an external electric field of the

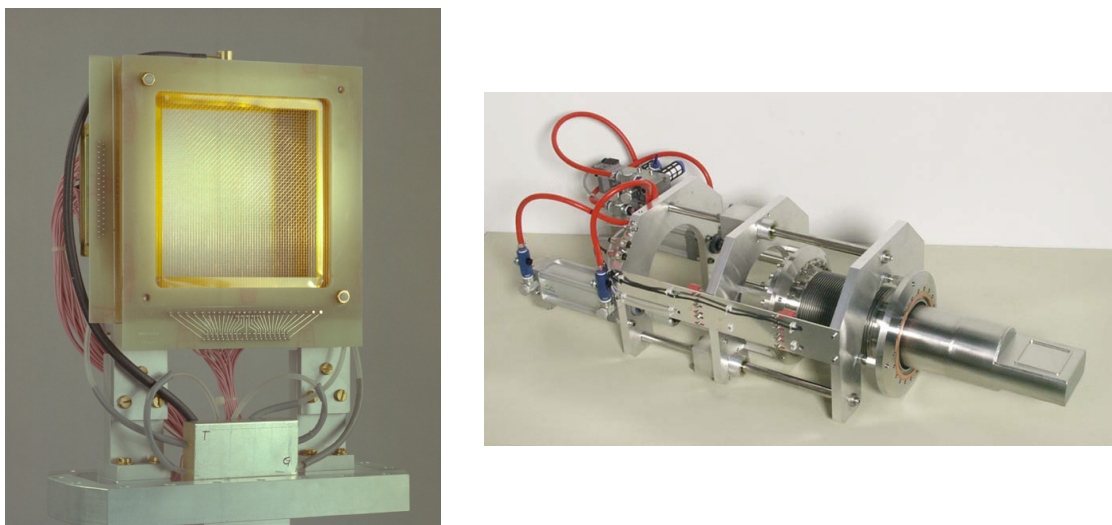


Fig. 53: Left: Multiwire proportional chamber used for profile measurement of slowly extracted ion beams at GSI. Right: Pneumatic drive with multiwire proportional chamber mounted inside pocket having normal pressure and separated from vacuum by a 100 μm thick foil.

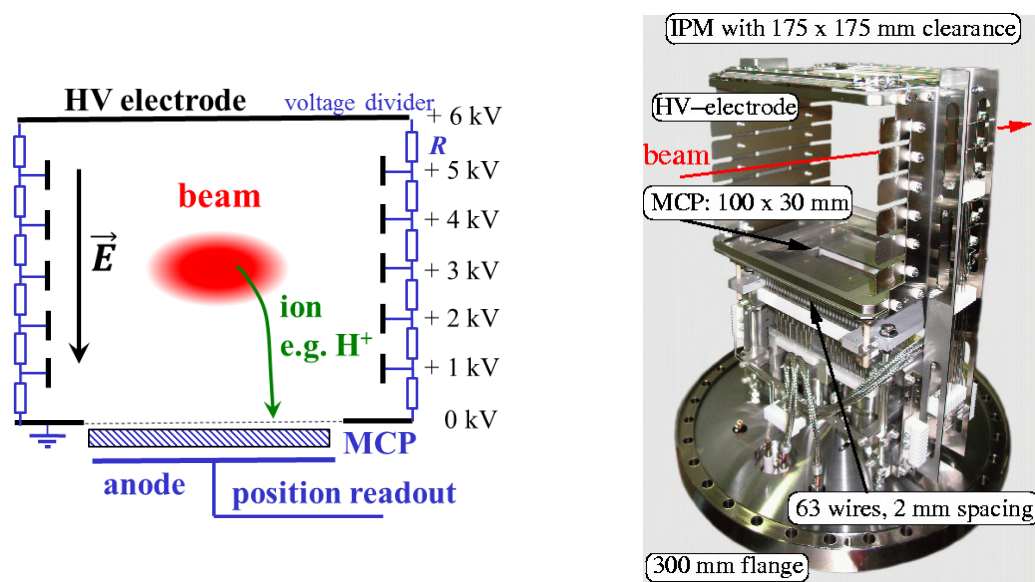


Fig. 54: Left: Scheme of ionization profile monitor for horizontal profile determination. Right: The large aperture ionization profile monitor installed at the GSI synchrotron for the horizontal direction; the clearance is 175 mm \times 175 mm. The monitor is mounted on a \varnothing 300 mm flange. The readout behind the multichannel plate (bottom) is achieved with an array of 63 wires with 2 mm spacing.

order of 1 kV/cm is applied by metallic plates installed in the vacuum pipe, but outside the beam path. To obtain a more homogeneous field, guiding strips are installed at the side to get a smooth transition from the high-voltage side to the ground plane. For most applications, the residual gas ions are detected in this set-up. A realization from the GSI synchrotron, with a large opening, of 17 cm, is shown in Fig. 54 [75, 76].

For the linac case, the vacuum pressure is high and the energy loss is larger, owing to the lower beam energy. Enough electron-ion pairs are generated to give a measurable current (down to 0.1 nA

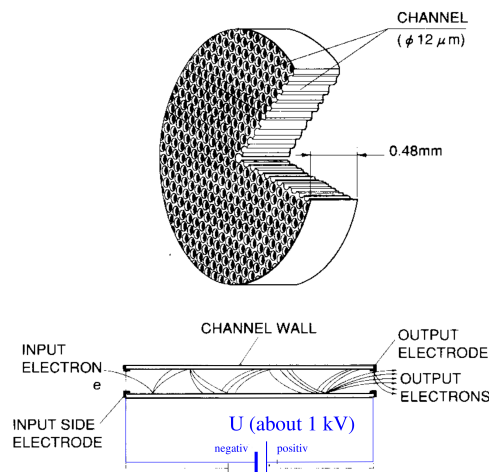


Fig. 55: Scheme of a single multichannel plate made of a glass plate with small channels, where the amplification of the secondary electrons takes place.

per strip) of secondary ions for direct detection by a sensitive SEM grid-like wire array [77, 78]. In a synchrotron, the pressure and the stopping power are smaller. A multichannel plate particle detector is used as a ‘pre-amp’. A multichannel plate is made of a 1 mm thick glass plate with round channels of $\sim 10 \mu\text{m}$, see Fig. 55. These channels are coated with high-resistivity materials and a voltage of $\sim 1 \text{ kV}$ is applied across them. When a residual gas ion (or electron) hits the surface, secondary electrons are liberated, i.e., the ions are converted to electrons. These electrons are multiplied, as in a photomultiplier, by a factor of typically 10^3 per multichannel plate. Owing to the diameter of the channels, the spatial resolution of a single step multichannel plate is of the order of 0.03 mm. For higher amplifications, a two-step device (Chevron geometry) with a gain of $\sim 10^6$ is used, resulting in a resolution of about 0.1 mm.

To detect the secondary electrons at the multichannel plate output, two technologies concerning the anode are available.

- A SEM grid made of wires with $\sim 0.5 \text{ mm}$ diameter and 1 mm spacing. The advantage is the fast readout made possible using appropriate electronics [79]. The disadvantage is the limited spatial resolution.
- A phosphor screen installed close to the back of the multichannel plate. The secondary electrons create a light pulse, which is imaged by a CCD camera. The advantage is the high resolution, as there are several hundreds of pixels for one plane, and the cheap and direct data acquisition system supplied by the commercial CCD camera. However, with this technique, the time resolution and the image repetition rate are limited by the CCD camera frame-rate, of about 100 frames per second. For faster readout, the CCD is replaced with a photomultiplier or avalanche diode, e.g., Ref. [80].

In the following, we discuss some examples for the profile measurement inside a synchrotron.

Adiabatic damping. During the acceleration of a beam inside a synchrotron, the beam width should shrink. This is related to the fact that the emittance is defined in the laboratory frame by the angle between the transverse and longitudinal velocities. During acceleration, the longitudinal velocity increases (for the non-relativistic case), while the transverse component remains the same, leading to a decrease of the angle between both vectors, as shown schematically in Fig. 56. This is called transverse adiabatic damping by the conservation of the normalized emittance; see also the discussion in Section 5 and Eq. 40. The normalized emittance is defined as $\epsilon_{\text{norm}} = \beta\gamma\epsilon$ for a beam of velocity β , Lorentz factor γ and actual emittance ϵ . The beam width σ scales as $\sigma \propto \sqrt{\epsilon}$. In Fig. 56, the decrease of the beam width

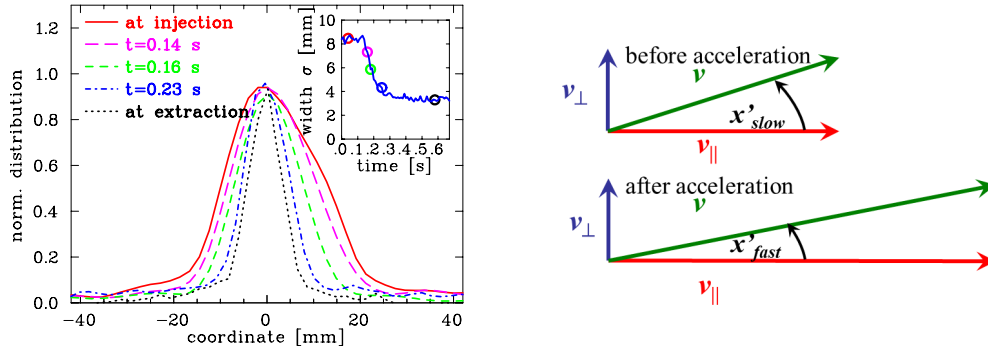


Fig. 56: Left: Evolution of the horizontal beam profile during the acceleration of C^{6+} from 6.7 MeV/u to 600 MeV/u within 0.4 s at the GSI synchrotron. The inset depicts the evolution of the beam width of one standard deviation during the acceleration started at 0.15 s; the depicted beam profiles are indicated by coloured circles. Right: Schematic visualization of transverse, v_{\perp} , and longitudinal, v_{\parallel} , velocity evolution during acceleration, leading to a decrease of the angle x' .

is demonstrated for the acceleration of a C^{6+} ion beam from a kinetic energy of $E_{\text{ini}} = 6.7$ MeV/u, corresponding to a velocity of $\beta_{\text{ini}} = 12\%$ and a Lorentz factor of $\gamma_{\text{ini}} = 1.007$, to $E_{\text{final}} = 600$ MeV/u, corresponding to $\beta_{\text{final}} = 79\%$ and $\gamma_{\text{final}} = 1.64$. The assumption of normalized emittance preservation would lead to the scaling of the expected beam width as

$$\sigma_{\text{final}}^{\text{theo}} = \sqrt{\frac{\beta_{\text{ini}} \cdot \gamma_{\text{ini}}}{\beta_{\text{final}} \cdot \gamma_{\text{final}}}} \cdot \sigma_{\text{ini}}^{\text{theo}} = 0.33 \cdot \sigma_{\text{ini}}^{\text{theo}}$$

for the case depicted in Fig. 56. The experimental value $\sigma_{\text{final}}^{\text{exp}} = 0.37 \cdot \sigma_{\text{ini}}^{\text{exp}}$ is close to that theoretical value; the larger value for the experimental case is related to a change of the focusing and further imperfections during the acceleration. An ionization profile monitor, as a non-intercepting device, is well-suited for a long-time observation without any influence on the beam.

Properties during multiturn injection. During a typical multiturn injection, the horizontal phase space is filled like a spiral. This is controlled by bumper magnets inside the synchrotron, which shifts the orbit of the stored particles for each turn and the duration of the beam delivery, as varied by a chopper in the transfer line in front of the synchrotron. The process is performed such that the central orbit, i.e., the central part of the horizontal phase space, is filled first. If now the length of the injected beam pulse is varied, the process can be demonstrated, as displayed in Fig. 57. For a short beam pulse, the beam width and, therefore, the beam emittance is small and increases with the duration of the beam delivery. The vertical emittance is not influenced in the displayed case, showing the absence of horizontal–vertical coupling in the synchrotron. However, the stored beam current is significantly smaller if only one or a few turns are injected. During operation, the amount of accelerated particles and their emittance can be balanced; for a proton synchrotron, the normalized emittance is preserved (as shown already) and therefore the beam quality is dominated by the injection process.

Steering of the injected beam. If the beam is injected at an improper angle with respect to the synchrotron reference orbit, the particles might still be stored. However, particles at a large angle compared with the (imaginary) reference particle fill the phase space at the outer periphery. The beam profile is the projection of the phase space to the spatial axis and this peripheral distribution might correspond to a non-Gaussian beam with large shoulders or even a ‘hollow beam’. This is demonstrated in the left-hand panel of Fig. 58. Here, the beam’s steering angle with respect to the reference orbit of the synchrotron beam axis is changed by a transfer line dipole in front of the synchrotron. Depending on the chosen angle, the entire synchrotron acceptance can be filled, as demonstrated by an increase in the width and, correspondingly, the emittance of the stored beam. To prevent such an emittance blow-up, the steering angle

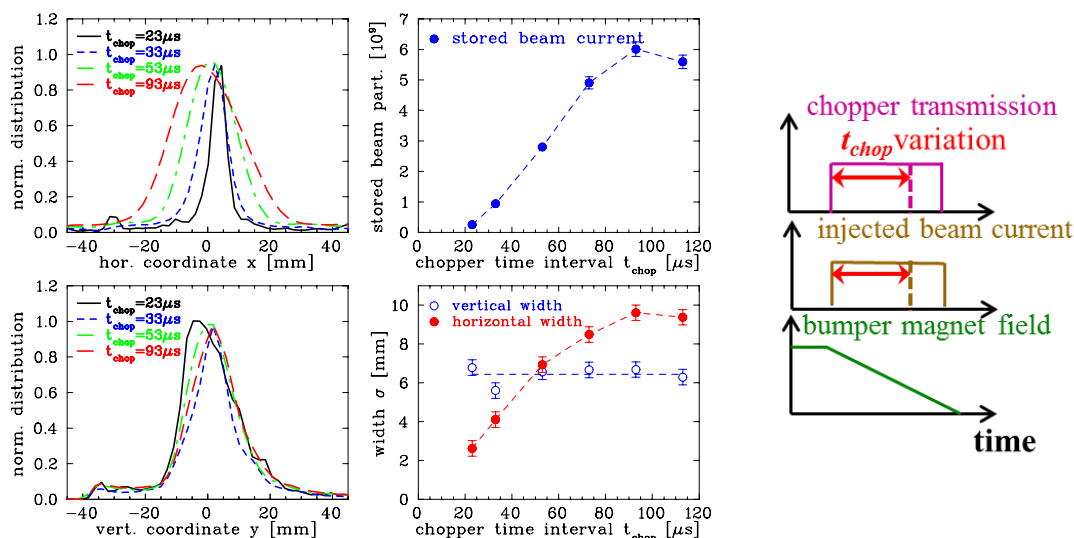


Fig. 57: Multiturn injection properties at an ion synchrotron for C^{6+} beam at 6.7 MeV/u with up to 6×10^9 ions per fill using a multiturn injection at the GSI synchrotron, with a revolution time of 5 μ s per turn; each profile is an average over about 100 turns. Top left: Horizontal beam profile for different beam delivery times. Bottom left: Vertical profile. Top centre: Beam current measured by a d.c. transformer. Bottom centre: Calculated standard deviation of the profiles. Right: Schematic diagram of transfer line chopper and synchrotron bumpers.

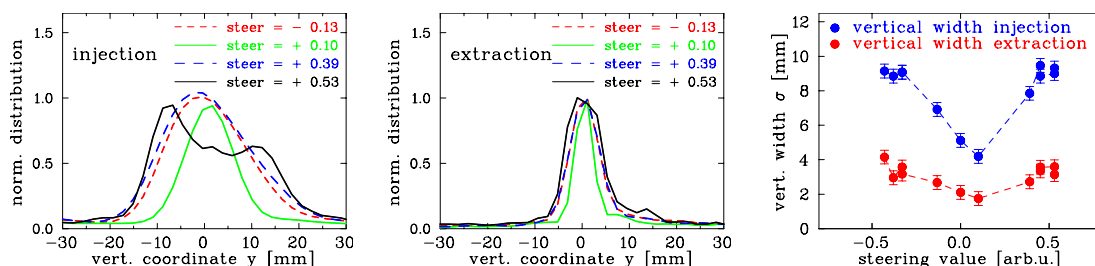


Fig. 58: Demonstration of the effect of vertical injection steering for the stored beam. The beam parameters are the same as of Fig. 57, followed by an acceleration to 600 MeV/u. Left: Vertical profiles at injection energy of 6.7 MeV/u. Middle: Vertical profiles at extraction energy of 600 MeV/u. Right: Beam width as a function of steering angle.

must be optimized to achieve a minimal beam width. For hadron synchrotrons, the enlarged emittance is conserved even after acceleration, leading to a decreased beam quality for the user. This is demonstrated in the middle panel of Fig. 58, which shows the profile measurement of the circulating beam after acceleration for the same values of the steerer in the injection line. The right-hand panel of this figure depicts the beam width before and after acceleration as a function of the steering angle and demonstrates the emittance blow-up for these cases.

Betatron mismatch for synchrotron injection. To prevent transverse emittance enlargement, it is important to control the injection into a synchrotron for a single-turn injection. If the orientation of the injected beam emittance is wrong, owing to misaligned focusing in the transfer line, beam storage might still be possible but then the emittance ellipse would start to rotate with an angle per revolution given by the fractional part q of the tune Q of the synchrotron, as shown in Fig. 59. A rotating ellipse is equivalent to a variation in the beam profile from turn to turn. After several hundred turns, the full synchrotron acceptance is filled, owing to the decoherence of the single particle's betatron-phases (e.g., caused by the momentum spread of the particles Δp and the coupling to tune via chromaticity ξ as $\Delta Q/Q_0 = \xi \cdot$

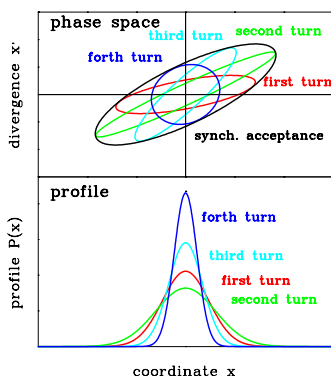


Fig. 59: Schematics for betatron mismatched injection into a synchrotron. If the orientation of the injected beam emittance does not fit the acceptance, variations of the beam profile occur.

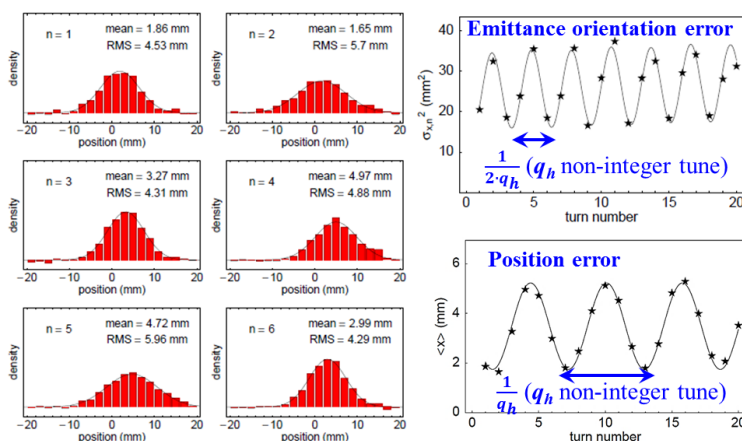


Fig. 60: Left: Profile measurement for a mismatched injection into the CERN PS synchrotron for the first $n = 1, \dots, 6$ turns. Right: Fitted square of the beam width and centre as a function of time [81].

$\Delta p/p_0$), leading to a larger circulating beam and an emittance blow-up. The mismatch can be determined by recording the profile width on a turn-by-turn basis.

An example is shown in Fig. 60 for a proton injection into the CERN PS synchrotron with 1.4 GeV energy and a bunch length of 80 ns [81, 82]. A thin SEM grid is used and the data are digitized for each revolution of the short bunch. The energy loss of the protons in the wires is too small to influence this measurement during only a few turns. The oscillation of the profile width can be seen; the fitted Gaussian width is plotted as a function of the turn number. The mismatch of the emittance orientation leads to an oscillation of the beam width with a periodicity given by the fractional part of the tune as $1/2q_h$; because of the symmetric phase space distribution, depicted in Fig. 59, one half rotation in phase space leads to reproduction of the profile. For the depicted case, the mismatch results in a blow-up of the stored emittance by $\sim 10\%$. The variation of the centre of the transverse profile is caused by a mismatch in terms of dispersion; the centre oscillates with a period of $1/q_h$. A better injection is created by changing the setting of the quadrupole magnets in the transfer line. Such measurements can also be performed by a turn-by-turn readout of an ionization profile monitor; an example is shown in [83, 84].

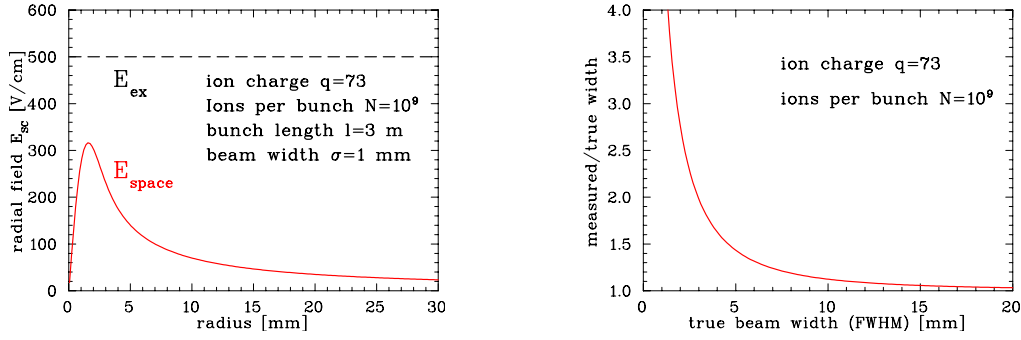


Fig. 61: Left: Space charge field of 7×10^{10} charges per 3 m bunch length. Right: Resulting relative broadening using an ionization profile monitor with ion detection, plotted using Eq. 24.

4.5.1 Ion detection: resolution limit by the beam's space charge

The residual gas ions or electrons are accelerated towards the detector by applying an external electrical field of typically 0.3–3 kV/cm. However, the beam, made of charged particles, also carries an electrical field, the space charge field, which influences the trajectory as well. The radial electrical field E_{space} of a round beam is given non-relativistically for a Gaussian distribution with standard deviation σ (full width at half-maximum = $2.35 \cdot \sigma$) by

$$E_{\text{space}}(r) = \frac{1}{2\pi\epsilon_0} \cdot \frac{qeN}{l} \cdot \frac{1}{r} \cdot \left(1 - e^{-\frac{r^2}{2\sigma^2}}\right), \quad (22)$$

assuming equal beam sizes in the horizontal and vertical directions, which leads to a radially symmetrical field, where qeN/l is the number of particles in charge state q per unit length. For high-current operation, this field strength is comparable to the external field, see Fig. 61. The residual gas ions or electrons are accelerated by both fields, leading to a broadening of the measured profile, see Fig. 62. To estimate the real beam size, the correction can be calculated via

$$\sigma_{\text{beam}}^2 = \sigma_{\text{meas}}^2 - \sigma_{\text{corr}}^2, \quad (23)$$

where σ_{corr} is given to a first-order approximation by the beam space charge and the external field according to [85–88]

$$\sigma_{\text{corr}}^2 = \frac{e^2 \ln 2}{4\pi\epsilon_0 \sqrt{m_p c^2}} \cdot d_{\text{gap}} \cdot qN \cdot \sqrt{\frac{1}{eU_{\text{ex}}}}. \quad (24)$$

The correction is proportional to the number of beam particles N . It is inversely proportional to the square root of the external field (created by the static voltage U_{ex}); therefore, an increase of the external field has only a relatively weak influence on the broadening. A large distance d_{gap} between the two high-voltage electrodes results in a longer drift time and therefore in a prolonged influence of the space charge field. To calculate this correction for a real case with different horizontal and vertical sizes and a longitudinal extension within the bunch, numerical simulations are required, see, e.g., Refs. [87, 88].

The initial velocity of the residual gas ions immediately after the ionizing atomic collision between the residual gas molecule and the beam particle (Bethe–Bloch regime) is too small to affect the resolution (in contrast with the electron detection scheme, see next section).

4.5.2 Electron detection in the presence of a magnetic field

To measure intense beams, electron detection is more suited for overcoming space charge induced broadening, see Fig. 62. For this, the high voltage is reversed, to accelerate the negative electrons created by

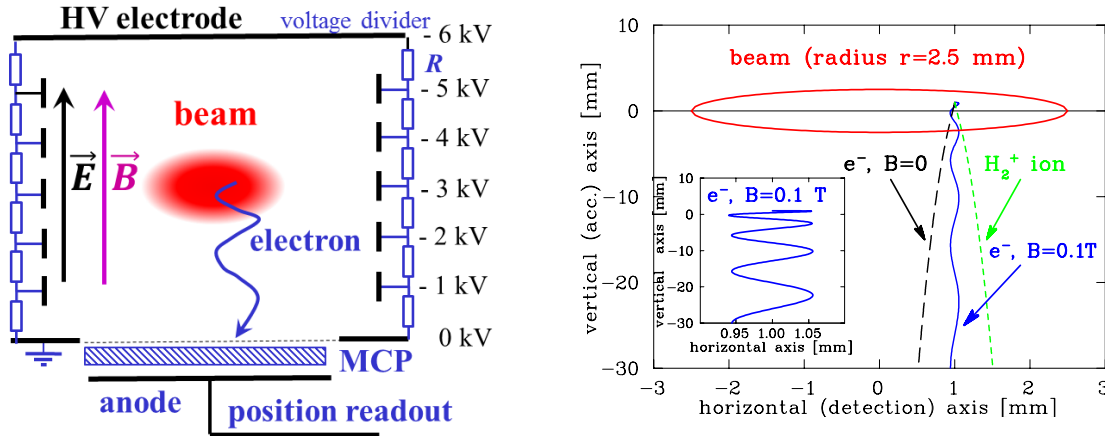


Fig. 62: Left: Trajectory of electron in ionization profile monitor in the presence of a homogeneous electric E and magnetic field B . Right: Comparison of trajectories of H_2^+ ion and electron with and without magnetic field, showing the broadening due to the beam space charge field. By applying a magnetic field, the electron is fixed to the field line, as shown in the inset. Beam parameters: $10^9 U^{73+}$ within a 10 m long bunch with radius 2.5 mm.

the beam interaction towards the detector. If an additional magnetic field B is applied parallel to the external electrical field, the electrons spiral around the magnetic field lines with the cyclotron radius $r_c = \sqrt{2m_e E_{kin,\perp}}/eB$ with $E_{kin,\perp}$ being the kinetic energy fraction perpendicular to the magnetic field. This transverse kinetic energy is determined by the initial transverse velocity given by the kinematics of the atomic collision. The cross-section depends on the beam and residual gas molecule properties [89], resulting in kinetic energies of up to kiloelectronvolts for the emitted electron, for the typical case. The cyclotron radius, and therefore the detector resolution, is mainly determined by this initial energy and is almost independent of the beam space charge field. The projection of the trajectory in the plane perpendicular to the field is a circle with less than 0.1 mm radius (corresponding to the spatial resolution of the multichannel plate) if a magnetic field of $B \simeq 0.1$ T is applied. The movement along the field is a linear acceleration with a typical time of flight of ~ 2 ns. In most cases, the necessary magnetic field of about 0.1 T is generated using a dipole magnet of the same type as used for the beam bending, see, e.g., Ref. [80].

4.6 Optical transition radiation screens

At electron accelerators with relativistic particles, the profile is determined from the so-called optical transition radiation at an intercepting thin metallic foil. The optical transition radiation is produced in a purely classical electromagnetic process, including special relativity, when a charged particle passes from one medium into another. While passing to the vacuum in front of the foil, the particle has a certain electromagnetic field configuration, which is different from the field inside the medium, because the foil has a (complex) dielectric constant $\epsilon_r \neq 1$, i.e., different from vacuum. On approaching the foil, the particle's electromagnetic field leads to a time-dependent polarization at the foil boundary. When the charged particle traverses the foil, the field configuration is suddenly changed. The change of this polarization at the foil surface generates radiation with a characteristic intensity and angular distribution.

A typical set-up of an optical transition radiation measurement is shown in Fig. 63. The foil is inserted at $<45^\circ$ with respect to the beam path in most cases. The foil is made of aluminium or aluminium coated on Mylar with a thickness of 1 μm or less. The light is emitted in the forward direction as well as at 90° , because the metallic surface acts as a mirror. Depending on the particle energy, the angular distribution peaks at an angle $\theta = 1/\gamma$, where γ is the relativistic Lorentz factor. For typical values, 100 to 1000 beam particles yield one photon in the optical wavelength range. With appropriate optics, an

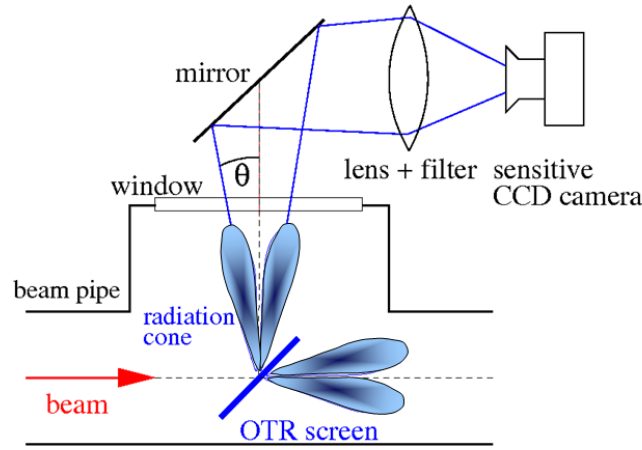


Fig. 63: Optical transition radiation (OTR) screen measurement

image of the foil is recorded with a CCD or CMOS camera. In some cases, an image amplifier is used, owing to the relatively small number of photons.

The general process is treated in, e.g., Refs. [18, 90, 91], leading to closed but extensive formulae. For relativistic beam particles and some other valid assumptions, the radiated energy dW into a solid angle $d\Omega$ per frequency interval $d\omega$ can be approximated as

$$\frac{d^2W}{d\Omega d\omega} = \frac{2e^2\beta^2}{\pi c} \cdot \frac{\theta^2}{(\gamma^{-2} + \theta^2)^2} \quad (25)$$

where c , e , and γ are the velocity of light, the elementary charge, and the relativistic Lorentz factor, respectively. The observation is oriented at an angle θ perpendicular to the beam path, the so-called specular angle, see Fig. 63. There is no difference in the radiation for electrons or protons moving with the same Lorentz factor, reflecting the fact that only the electromagnetic fields of the beam particles are concerned. Note that the radiated energy does not depend on the frequency, ω , i.e., the whole spectrum is covered. This is valid up to the plasma frequency of the metal, which, for most metals, is in the deep ultraviolet, at about 10 eV. The radiated energy of Eq. 25 is converted to the number of photons by $W = N_{\text{photon}} \cdot \hbar\omega$, observed within a wavelength interval from λ_{begin} to λ_{end} in the optical region by the camera and integration over the interval $\lambda_{\text{begin}} - \lambda_{\text{end}}$. This yields the number of photons per solid angle

$$\frac{dN_{\text{photon}}}{d\Omega} = N_{\text{beam}} \cdot \frac{2e^2\beta^2}{\pi\hbar c} \cdot \log\left(\frac{\lambda_{\text{begin}}}{\lambda_{\text{end}}}\right) \cdot \frac{\theta^2}{(\gamma^{-2} + \theta^2)^2}, \quad (26)$$

where N_{beam} is the number of beam particles. This function is plotted in Fig. 64 for three different values of γ . It is clearly seen that the radiation is more tightly focused for higher energies (more precisely, higher values of the Lorentz factor γ), having the advantage that a larger proportion of the photons reach the camera. At electron accelerators, optical transition radiation is used even at moderate energies above $\simeq 100$ MeV (corresponding to a Lorentz factor $\gamma \simeq 200$). For proton acceleration with a Lorentz factor $\gamma \simeq 200$ or equivalent, a beam energy for protons above 200 GeV is only achieved at some high-energy facilities, such as CERN SPS and LHC, where optical transition radiation screens are installed [92, 93].

The optical transition radiation profile determination has some advantages and disadvantages compared with a scintillating screen measurement [52, 53, 58].

- It is based on a classical electromagnetic process, leading to a linearity between the number of photons and the beam intensity.

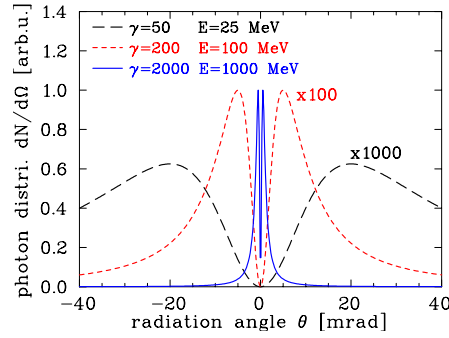


Fig. 64: Intensity distribution of optical transition radiation as a function of observation angle for three different values of the Lorentz factor γ . Corresponding beam energies for electrons are also given. The photon intensity is enhanced by a factor of 1000 for $\gamma = 50$ and 100 for $\gamma = 200$ in the plot.

- The number of photons and their distribution are independent of the thickness of the foil. Therefore, very thin foils of pure aluminium foil or aluminium coated on Mylar down to $0.25 \mu\text{m}$ can be used.
- It is still an intercepting method, but a thin foil minimizes the influence on the beam, owing to the low scattering probability. It can also be applied at high beam power, because of the low energy loss in the thin, low- Z material.
- It is mainly used for electron beams with energies above 100 MeV. For proton beams, the necessary γ is only reached at very-high-energy accelerators.
- The intensity of usable light using an optical transition radiation screen is orders of magnitude less than for a scintillation screen. Therefore, more advanced and expensive cameras must be used.

4.7 Synchrotron radiation monitor

For electron accelerators, the effect of synchrotron radiation, emitted by accelerated electrons, can be used for profile determination. As known from classical electrodynamics [18], the radiation power P_{synch} is given for a momentum change dp/dt of a particle with mass m_0 by

$$P_{\text{synch}} = \frac{e^2 c}{6\pi\epsilon_0(m_0 c^2)^2} \left[\frac{dp}{dt} \right]^2. \quad (27)$$

For a circular accelerator, the direction of the momentum is changed in the bending dipole magnets, leading to the emission of synchrotron radiation, which is significant only for relativistic energies with a Lorentz factor above at least $\gamma > 100$. Therefore, the process is of importance for most circular electron accelerators but only for proton accelerators with an energy above some 100 GeV.

In the centre-of-mass system, the radiation is emitted perpendicular to the momentum change. The Lorentz transformation to the laboratory frame gives a factor of γ , yielding a forward peak distribution with opening cone of half angle γ , as demonstrated in Fig. 65. The physical basis, the achievable resolution, and some applications are reviewed in Ref. [94].

The light emitted by the electron's bend in a dipole magnet can be used to monitor its horizontal and vertical beam profile, as shown schematically in Fig. 66. For diagnostic purposes, the optical part of the emitted spectrum is observed, in most cases, by using optical band-pass filters. For this wavelength, high-quality optics are available and standard CCD or CMOS cameras can be used. A typical resolution limit for the related optics is of the order of $\sim 100 \mu\text{m}$, and is related to the diffraction pattern created at the finite-size lenses and filters [94, 95]. A higher resolution can be achieved by observing the light from wigglers or undulators, if they are installed in the synchrotron.

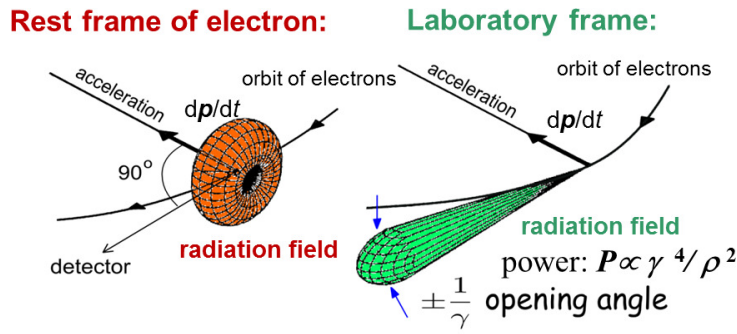


Fig. 65: Forward peaked synchrotron radiation for relativistic particles from a bending magnet

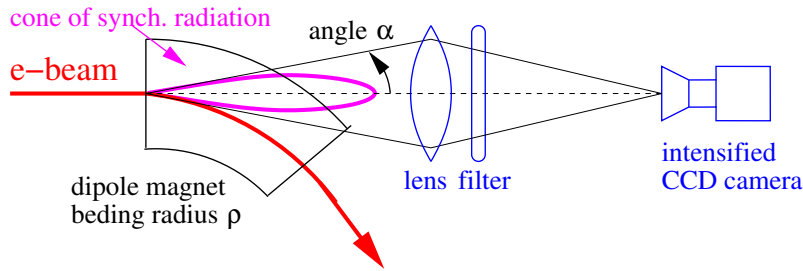


Fig. 66: Scheme for a synchrotron radiation profile monitor to observe the radiation from a dipole

A realization of a synchrotron light profile monitor used at CERN LEP is shown in Fig. 67 [96]. The bending radius here is 3.1 km; diffraction gives the largest contribution to the resolution, by about $\sigma \sim 300 \mu\text{m}$, which is comparable to the real electron beam size close to the final energy. The set-up consists of a metallic mirror to deflect the light out of the plane of the beam. Owing to the high power of the synchrotron radiation, the mirror must be cooled; possible deformations can spoil the optical quality. With the help of some curved mirrors, the light is focused; an optical filter selects the wavelength range of blue or ultraviolet light; the detector is an image-intensified CCD camera. Even though the resolution is not too high, this relatively straightforward system can be quite helpful, owing to its non-destructiveness, as demonstrated in Fig. 68 from the synchrotron light source APS [97]. Such synchrotron light monitors can also be installed at dipoles in transfer lines, as realized at some facilities, e.g., Ref. [98]. However, there might be some technical problems, as the amount of light emitted by the single pass of the electrons might be insufficient; instead optical transition radiation screens, owing to their simpler technical realization, serve as frequently used profile diagnostics in transfer lines at third-generation light sources, while scintillation screens are used for low beam current applications at other electron accelerators.

An example of the application of a synchrotron radiation monitor during acceleration at the ALBA booster synchrotron is shown in Fig. 69 [99, 100]. For the two-dimensional beam image, the widths in the horizontal and vertical directions can be calculated and compared with simulations. At first glance, the adiabatic damping is less pronounced than in the example of the hadron beam shown in Fig. 56: the reason is the contribution to the beam width of the relative momentum spread $\Delta p/p_0$ of the beam particles and the non-zero dispersion D at the measurement location,

$$x_{\text{tot}} = \sqrt{\varepsilon\beta + (D \cdot \Delta p/p_0)^2},$$

and the contribution of the quantum fluctuations related to the emission of photons [99, 100].

The diffraction limit of the standard monitor can be compensated for by using an interference technique with a double slit, known from astronomy. The beam width can be calculated from the

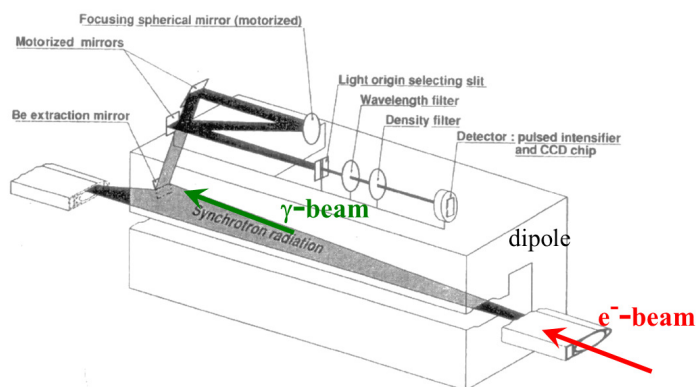


Fig. 67: Synchrotron radiation profile monitor at LEP. The optical system is installed close to the dipole magnet with bending radius of 3100 m [96].

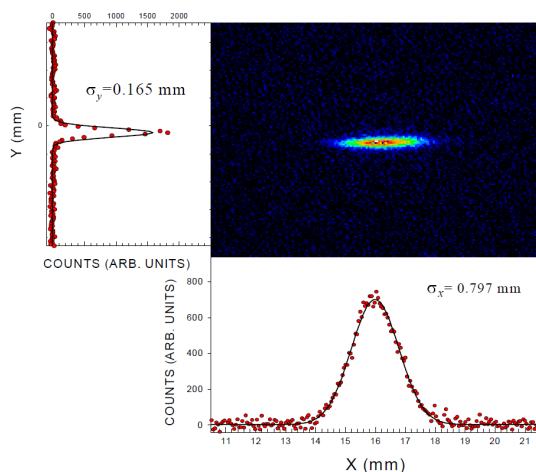


Fig. 68: Image of electron beam in the APS accumulator ring, obtained using synchrotron radiation monitor [97]

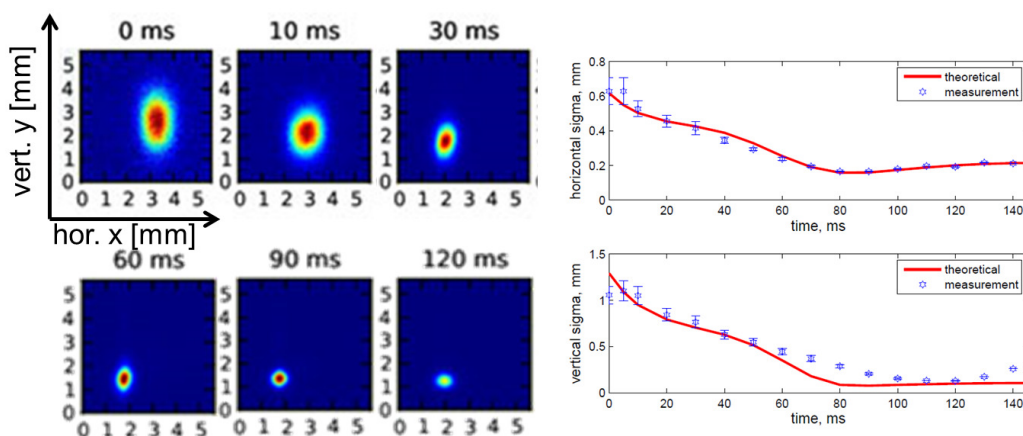


Fig. 69: Left: Examples of two-dimensional beam images obtained using a synchrotron light monitor at the ALBA booster synchrotron. Right: Fitted horizontal and vertical beam widths during acceleration from 0.1 to 3 GeV within 130 ms and comparison with simulations [99, 100].

distance of the minima of the interference pattern. Owing to non-coherent emission by an ensemble of electrons, the fringes fade out for large beam sizes. A resolution down to the micrometre range has been realized with this method in combination with elaborate analysis tools, see, e.g., Refs. [94, 101, 102].

A higher resolution can also be achieved by monitoring the profile at much shorter wavelengths; X-ray pinhole cameras are used for this purpose. Only the emitted X-rays, scraped by a typically 20 μm aperture of high- Z material are recorded by a detector. A typical resolution, concerning the beam width, of 10 μm can be obtained using such an X-ray observation scheme [94] but this requires a more complex technical realization than for the observation in the optical range.

5 Measurement of transverse emittance

The emittance describes the quality of a beam. Its determination is based on profile measurements; it is unimportant what method of profile measurement is used, as long as it has an adequate resolution. In the following, we start with a slit-grid device, in which the spatial co-ordinate is fixed by an aperture and the angle distribution is measured. This is suited for particles with a range in matter below ~ 1 cm, i.e., protons or ions with $E_{\text{kin}} < 100$ MeV/u. The emittance can also be determined by fitting the beam envelope measured at one location with different focusing conditions or at different locations. This can be applied to transfer lines for all particle conditions. However, here it is problematic to include emittance growth due to space charge forces, i.e., blow-up of the transverse size due to the forces between the charged particles. A detailed review of the involved physics, technologies, and data acquisition is given in Ref. [103].

In a synchrotron, it is sufficient to measure the beam profile at one location only. For the stationary state of stable storage, the orientation of the ellipse, which is equivalent to knowledge of the lattice function dispersion $D(s)$ and β function $\beta(s)$, is fixed (or can be measured separately). The emittance is calculated from the beam width σ as

$$\epsilon = \frac{1}{\beta(s)} \left[\sigma^2 - \left(D(s) \frac{\Delta p}{p} \right)^2 \right], \quad (28)$$

which is valid for the horizontal and vertical planes, respectively. If only horizontal bends occur in a facility, the dispersion in the vertical direction is, in most cases, $D_y = 0$, and Eq. (28) simplifies to $\epsilon_y = \sigma_y^2 / \beta_y(s)$.

5.1 Definition of emittance

The motion of the beam particle can be described by a linear second-order differential equation. This assumes the absence of any non-linear coupling, such as space charge forces or beam-beam effects, as well as coupling between the two transverse planes and the longitudinal plane. The beam quality is given by the phase space volume, which, in this case, is a constant of the motion. The emittance for one plane is defined by

$$\epsilon_x = \frac{1}{\pi} \int_A dx dx', \quad (29)$$

where $A = \pi\epsilon$ is the area of the phase space occupied by the beam, see Fig. 70. Determination of the emittance is equivalent to determination of the distribution of the spatial co-ordinate x (i.e., the beam profile), the distribution in angle x' and the correlation between x and x' .

The interpretation of an area assumes a hard-edge, homogeneous distribution. A more realistic case is the Gaussian density distribution $\rho(x, x')$, defined at the position of the vector $\vec{x} = (x, x')$ for each location s along the beam path. The two-dimensional density is then (the notation is defined later)

$$\rho(x, x') = \frac{1}{2\pi\epsilon_x} \exp \left[\frac{-1}{2} \vec{x}^T \boldsymbol{\sigma}^{-1} \vec{x} \right] \equiv \frac{1}{2\pi\epsilon_x} \exp \left[\frac{-1}{2 \det \boldsymbol{\sigma}} \left(\sigma_{22} x^2 - 2\sigma_{12} x x' + \sigma_{11} x'^2 \right) \right]. \quad (30)$$

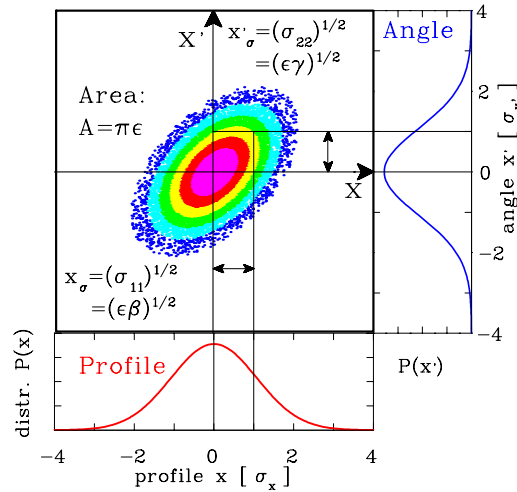


Fig. 70: Emittance ellipse and projection to space- and angle co-ordinates for a Gaussian density distribution. Values of the independent variables are given in units of the standard deviation.

The profile distribution $P(x)$ is obtained by integrating the density ρ over x' as

$$P(x) = \int \rho(x, x') dx'.$$

The parameter $\sqrt{\sigma_{11}}$ is the standard deviation of this distribution; $\sqrt{\sigma_{22}}$ is the corresponding value for the angular distribution $P(x')$ obtained by integrating $\rho(x, x')$ over x as $P(x') = \int \rho(x, x') dx$. σ_{12} is called the covariance; it describes the correlation between x and x' and is related to the orientation of the ellipse in the phase space. With the help of the three-parameter σ_{ij} , the so-called beam matrix σ can be defined as

$$\sigma(s) = \begin{pmatrix} \sigma_{11}(s) & \sigma_{12}(s) \\ \sigma_{12}(s) & \sigma_{22}(s) \end{pmatrix} \quad (31)$$

at one location s in the beam line. The beam matrix σ is a representation of the beam ellipse at this location s and varies along the beam path. It is used in connection with the transfer matrix \mathbf{R} , which describes the action of the optical elements, such as drifts, dipoles, quadrupole magnets, or solenoids, along the beam path in a linear approximation, as

$$\sigma(s_1) = \mathbf{R} \cdot \sigma(s_0) \cdot \mathbf{R}^T \quad (32)$$

from a location s_0 to s_1 . See Section 5.3 for a more detailed discussion.

The absolute value of the emittance at each location can be defined using this notation as

$$\epsilon_x = \sqrt{\det \sigma} = \sqrt{\sigma_{11}\sigma_{22} - \sigma_{12}^2} \quad (33)$$

and corresponds to an occupation of 15% of the full phase space area. The unit of this value is the metre radian or, more frequently, the millimetre milliradian. To be consistent with the geometrical interpretation of an area surrounded by an ellipse, the number is multiplied by π ; in this case, 39% of the beam is inside the area

$$\pi \cdot \sqrt{\sigma_{11}\sigma_{22} - \sigma_{12}^2}.$$

In other words, the Gaussian beam quality at a given location s is fully described by the beam matrix $\sigma(s)$.

Frequently, the Twiss parameters are used; these are the beam matrix elements normalized by the emittance as

$$\alpha = -\sigma_{12}/\epsilon, \quad \beta = \sigma_{11}/\epsilon, \quad \gamma = \sigma_{22}/\epsilon. \quad (34)$$

Table 11: Fraction of beam inside different values of emittance for Gaussian distribution

Factor of ϵ_{rms}	$1 \cdot \epsilon_{\text{rms}}$	$\pi \cdot \epsilon_{\text{rms}}$	$2\pi \cdot \epsilon_{\text{rms}}$	$4\pi \cdot \epsilon_{\text{rms}}$	$6\pi \cdot \epsilon_{\text{rms}}$	$8\pi \cdot \epsilon_{\text{rms}}$
Fraction of beam f [%]	15	39	63	86	95	98

The beam matrix is then

$$\boldsymbol{\sigma} = \epsilon \cdot \begin{pmatrix} \beta & -\alpha \\ -\alpha & \gamma \end{pmatrix} \quad (35)$$

and the equation of the beam ellipse can be written as

$$\gamma x^2 + 2\alpha x x' + \beta x'^2 = \epsilon, \quad \text{with the normalization} \quad \beta\gamma - \alpha^2 = 1. \quad (36)$$

The widths of the profile and angular distribution are given by

$$x_\sigma = \sqrt{\sigma_{11}} = \sqrt{\epsilon\beta} \quad \text{and} \quad x'_\sigma = \sqrt{\sigma_{22}} = \sqrt{\epsilon\gamma}. \quad (37)$$

Their geometric meaning is one standard deviation of the transverse profile and angular distribution of the beam. The geometrical size of the phase space ellipse changes along the beam pass s ; therefore, the parameters $\alpha(s)$, $\beta(s)$ and $\gamma(s)$ are functions of the position s . In particular, for a synchrotron, $\beta(s)$ is called the beta function, describing the beam size via $x_\sigma(s) = \sqrt{\epsilon \cdot \beta(s)}$.

For theoretical calculations, one prefers analytical descriptions of the density distribution. An example is the Gaussian distribution of Eq. 30; other functions are discussed, e.g., in Ref. [104]. However, the beam does not always have a Gaussian shape. For any arbitrary phase space distribution, the beam emittance can be calculated via the statistical moments of a two-dimensional distribution $\rho(x, x')$.

To describe the beam quality via the emittance, the r.m.s. value can be calculated as

$$\epsilon_{\text{rms}} = \sqrt{\det \begin{pmatrix} \langle x^2 \rangle & \langle x x' \rangle \\ \langle x x' \rangle & \langle x'^2 \rangle \end{pmatrix}} = \sqrt{\langle x^2 \rangle \langle x'^2 \rangle - \langle x x' \rangle^2} \quad (38)$$

and follows the same general mathematical role as Eq. 33.

For a Gaussian distribution, the fraction f of the beam inside a certain value of the emittance can be expressed via the r.m.s. value as

$$\epsilon(f) = -2\pi\epsilon_{\text{rms}} \cdot \ln(1 - f), \quad (39)$$

leading to Table 11.

When a certain value of emittance is given for a beam, one must check its meaning carefully, because the different accelerator facilities do not share a common definition for the emittance around or of what beam fraction for a given emittance value is meant.

The emittance is a quantity defined in the laboratory frame, owing to the definition of the divergence. When a beam is accelerated, the divergence shrinks ('adiabatic damping') as a result of the changing ratio of longitudinal velocity v_s to transverse velocity v_x : $x' = v_x/v_s$. To compare the emittance for different longitudinal momenta, $p_s = m_0 \cdot \gamma_{\text{rel}} \cdot v_s$, the normalized emittance ϵ_{norm}

$$\epsilon_{\text{norm}} = \frac{v_s}{c} \gamma_{\text{rel}} \cdot \epsilon \quad (40)$$

is referred to a value $v_s/c \cdot \gamma_{\text{rel}} = 1$, where c is the velocity of light and $\gamma_{\text{rel}} = 1/\sqrt{1 - (v_s/c)^2}$ is the relativistic Lorentz factor. The normalized emittance is constant under ideal accelerating conditions.

A measurement of emittance means a determination of the numerical value of ϵ , as well as of the orientation and shape of the phase space distribution.

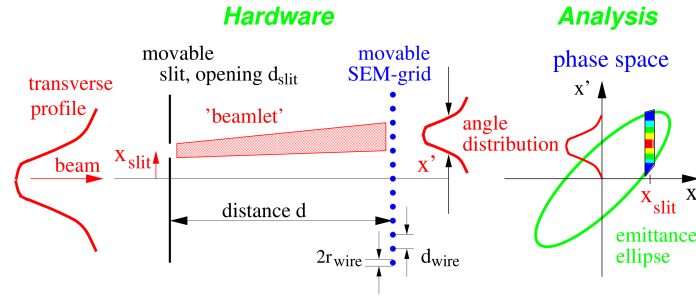


Fig. 71: Scheme of slit-grid emittance measurement device

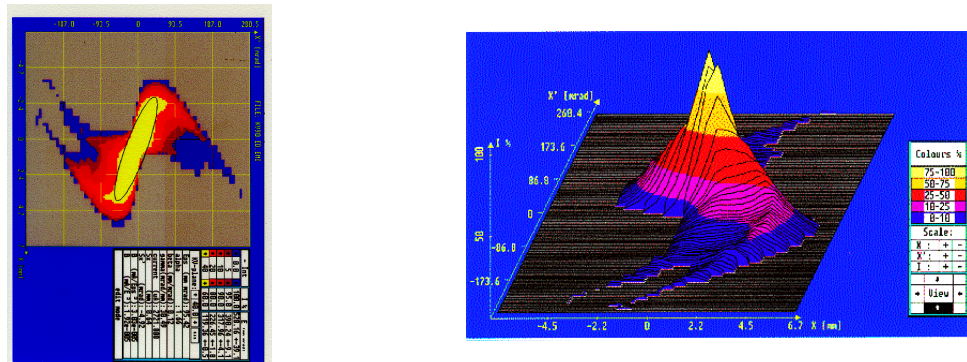


Fig. 72: Emittance measurement using a slit-grid device with a low-energy ion beam after the source at GSI display. Left: contour plot. Right: mountain plot.

5.2 Slit-grid method

A popular method at proton or ion linacs is the slit-grid device depicted in Fig. 71, where the beam particles have a penetration depth less than 1 cm. Here, the position x is fixed for one direction, with a thin slit having an opening of typically 0.1–0.5 mm to filter out only a small fraction of the beam at a known location. In the perpendicular direction, the full beam is transmitted to get a large signal. The angle x' is determined using a SEM grid having a distance from the slit of 10 cm to 1 m, depending on the ion velocity. In the field-free drift space, the trajectories of the particles, combined in a ‘beamlet’, are straight lines [105, 106]. The contribution to the emittance plot in the phase space is given by the angle distribution at the slit location. The slit is then scanned through the beam to determine the emittance at all positions. After making the full scan, the emittance is plotted and the r.m.s. value of the emittance ϵ_{rms} is calculated using the statistical moments, as given in Eq. 38 from the measured data. An elliptical shape is fitted to the data and the Twiss parameters can be calculated. An example is shown in Fig. 72 for a low-energy ion beam as a contour or three-dimensional plot. This method can also be used to determine more pathological phase space distributions, not only Gaussian distributions. This happens quite often close to an ion source, owing to the large space charge forces or the large profile width, where aberrations of the magnets could be significant.

The resolution for the space co-ordinate Δx is limited by the slit width $\Delta x = d_{\text{slit}}$. The angle resolution $\Delta x'$, measured at the distance d , is given by the radius of the wire r_{wire} and the width of the slit, resulting in $\Delta x' = (d_{\text{wire}} + 2r_{\text{wire}})/d$. The size of discrete elements in the phase space is given by $\Delta x \cdot \Delta x'$. This leads to a discretization error, in particular, in the case of small beam sizes (focused beam) or small angle distributions (parallel beam). The resolution is improved by scanning the SEM grid in steps that are smaller than the distance of the wires d_{wire} , increasing the density of the discrete elements in the phase space analysis. This can lead to overlapping elements, because their size $\Delta x \cdot \Delta x'$ remains constant. The same holds for a movement of the slit with step sizes smaller than the slit width.

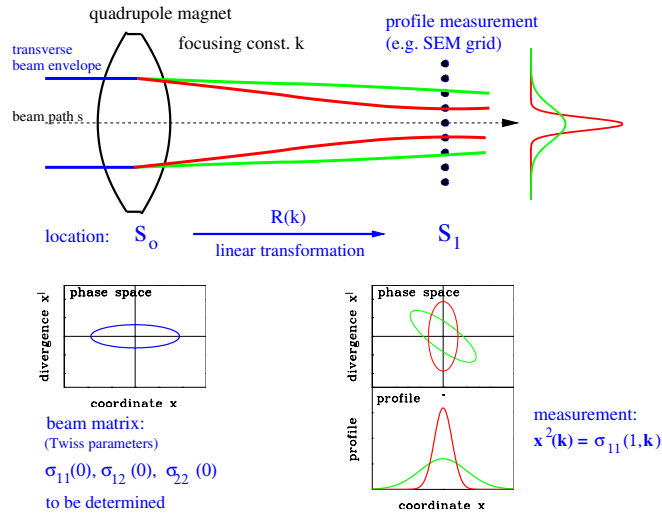


Fig. 73: Variation of quadrupole strength for determination of emittance at location s_0

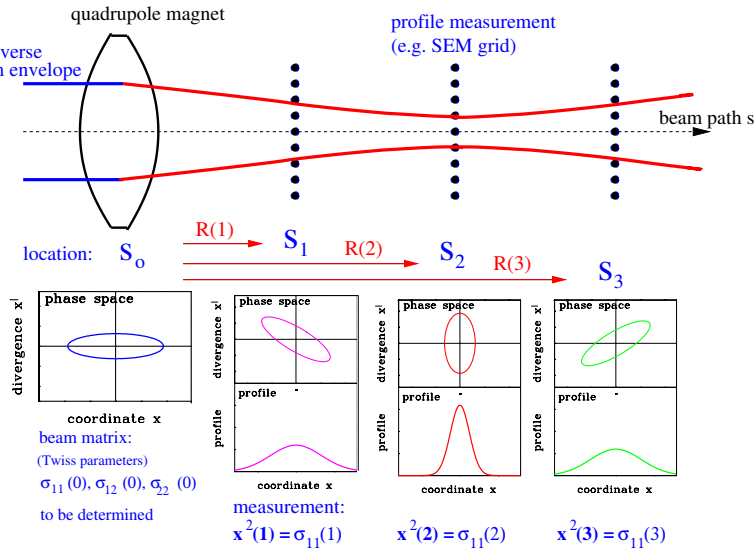


Fig. 74: Scheme for the emittance determination at a transfer line using profile measurement at three locations

5.3 Quadrupole variation

The emittance can be determined from a series of profile measurements, either by changing the focusing strength of a quadrupole, or by measuring at three or more positions along a transfer line, as shown schematically in Figs. 73 and 74. To derive the emittance from such a measurement, linear transformations are used. The described measurement is simply the reverse of normal transport calculations using such codes as MADX or WinAgile: Starting for a given emittance (size and orientation) at the input of a transport line, the beam envelope is calculated along the line. If the profile is measured, one calculates the emittance at the input of the line by using the same transformations in reverse (see later).

For a straight, non-dispersive transfer line, the transformation from a location s_0 to s_1 is given by the 2×2 transfer matrix \mathbf{R} . A determination of the emittance at the position s_0 is equivalent to the evaluation of the beam matrix σ at this position. The beam matrix is transformed to a second location s_1 with the help of the product of transfer matrices for the individual elements $\mathbf{R} = \prod \mathbf{R}_{\text{elements}}$ from the

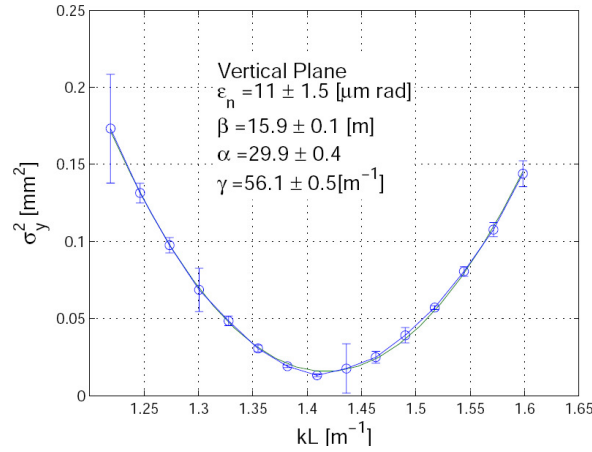


Fig. 75: Profile width determined using a YAG:Ce screen at Elettra electron linac for a quadrupole variation and parabolic fit [107].

quadrupole to the profile measurement location via

$$\boldsymbol{\sigma}(1) = \mathbf{R} \cdot \boldsymbol{\sigma}(0) \cdot \mathbf{R}^T \quad (41)$$

The beam width $x_{\text{rms}}(1)$ is measured at s_1 and the equation for the element $\sigma_{11}(1)$ is given by

$$x_{\text{rms}}^2(1) \equiv \sigma_{11}(1) = R_{11}^2 \sigma_{11}(0) + 2R_{11}R_{12} \sigma_{12}(0) + R_{12}^2 \sigma_{22}(0). \quad (42)$$

This is a linear equation for the unknown three beam matrix elements $\sigma_{ij}(0)$ at location s_0 , as shown in Fig. 73, in front of the focusing quadrupole magnet.

To get a solution, we need at least three different settings of the quadrupole strength k_i , and therefore different transfer matrices $\mathbf{R}(k_i)$ leading to three different readings of the profile width, as depicted in Fig. 73. Assuming $i = 1, 2, \dots, n$ different settings of the quadrupole strength k_1, k_2, \dots, k_n and n measurements of the beam width $x_{\text{rms}}^2(1, k_i) \equiv \sigma_{11}(1, k_i)$, a redundant system of linear equations is obtained in the form

$$\begin{aligned} \sigma_{11}(1, k_1) &= R_{11}^2(k_1) \cdot \sigma_{11}(0) + 2R_{11}(k_1)R_{12}(k_1) \cdot \sigma_{12}(0) + R_{12}^2(k_1) \cdot \sigma_{22}(0), \quad \text{focusing } k_1, \\ \sigma_{11}(1, k_2) &= R_{11}^2(k_2) \cdot \sigma_{11}(0) + 2R_{11}(k_2)R_{12}(k_2) \cdot \sigma_{12}(0) + R_{12}^2(k_2) \cdot \sigma_{22}(0), \quad \text{focusing } k_2, \\ &\vdots \\ \sigma_{11}(1, k_n) &= R_{11}^2(k_n) \cdot \sigma_{11}(0) + 2R_{11}(k_n)R_{12}(k_n) \cdot \sigma_{12}(0) + R_{12}^2(k_n) \cdot \sigma_{22}(0), \quad \text{focusing } k_n. \end{aligned} \quad (43)$$

The solutions of this system are the values of the beam matrix $\sigma_{ij}(0)$ (or, equivalently, the Twiss parameters) at the location s_0 , the entrance of the quadrupole magnet. With these values, the size and orientation of the phase space ellipse is fixed. For three measurements (k_1, k_2, k_3) , we can have a unique solution, but nothing is learnt about the errors. Therefore, more than three measurements must be made, leading to a redundant system of linear equations. The solution is reached by a least square fit to the best parameters of $\sigma_{ij}(0)$ or by solving the linear regression problem via so-called normal equations. Both algorithms are described in textbooks on linear algebra or numerical mathematics.

An example is shown in Fig. 75, obtained at the electron linac at Elettra for a beam with 107 MeV using a YAG:Ce scintillation screen for profile determination. To get a small error for the emittance determination, it is recommended to pass a beam waist using quadrupole variation. Only in this case can a parabola be fitted to the profile data with sufficient accuracy.

Instead of solving the redundant system of linear equations, one can start from the parabola fit of the beam size squared as a function of the quadrupole strength, as shown in Fig. 75. Most frequently, the transfer line comprises a quadrupole followed by a drift towards the profile measurement location. A quadratic dependence is observed for the following reason. Assuming a thin-lens approximation with a focal length f of the quadrupole action, one can write the transfer matrix as:

$$\mathbf{R}_{\text{focus}} = \begin{pmatrix} 1 & 0 \\ -1/f & 1 \end{pmatrix} \equiv \begin{pmatrix} 1 & 0 \\ K & 1 \end{pmatrix}. \quad (44)$$

After a drift of length L , one gets the transfer matrix of the transfer line

$$\mathbf{R} = \mathbf{R}_{\text{drift}} \cdot \mathbf{R}_{\text{focus}} = \begin{pmatrix} 1 + LK & L \\ K & 1 \end{pmatrix}. \quad (45)$$

Inserting this matrix into Eq. 41 for the transformation of the beam matrix $\sigma(1) = \mathbf{R} \cdot \sigma(0) \cdot \mathbf{R}^T$, one gets, for the measured beam matrix element, $\sigma_{11}(1) = x_{\text{rms}}^2(1)$:

$$\sigma_{11}(1) = L^2 \sigma_{11}(0) \cdot K^2 + 2 \left(L \sigma_{11}(0) + L^2 \sigma_{12}(0) \right) \cdot K + \sigma_{11}(0) + 2L \sigma_{12}(0) + L^2 \sigma_{22}(0). \quad (46)$$

This is the expected quadratic function in the quadrupole gradient K . From the beam width measurement for various quadrupole settings, a parabola fit is performed, as for Fig. 75, with the fit parameters a , b and c (this parametrization is chosen to yield a simple expression for the absolute value of the emittance, as shown later for Eq. 50):

$$\sigma_{11}(K) = a(K - b)^2 + c = aK^2 - 2abK + ab^2 + c. \quad (47)$$

A comparison of the coefficients of Eqs. 46 and 47 yields

$$\begin{aligned} a &= L^2 \sigma_{11}(0) \\ -ab &= L \sigma_{11}(0) + L^2 \sigma_{12}(0) \\ ab^2 + c &= \sigma_{11}(0) + 2L \sigma_{12}(0) + L^2 \sigma_{22}(0). \end{aligned} \quad (48)$$

These linear equations can finally be solved, resulting in the requested matrix elements at the entrance of the optical system:

$$\begin{aligned} \sigma_{11}(0) &= \frac{a}{L^2} \\ \sigma_{12}(0) &= -\frac{a}{L^2} \left(\frac{1}{L} + b \right) \\ \sigma_{22}(0) &= \frac{1}{L^2} \left(ab^2 + c + \frac{2ab}{L} + \frac{a}{L^2} \right). \end{aligned} \quad (49)$$

The absolute value of the emittance is calculated from these fit parameters via

$$\epsilon = \sqrt{\det \sigma(0)} = \sqrt{\sigma_{11}(0) \sigma_{22}(0) - \sigma_{12}^2(0)} = \frac{\sqrt{ac}}{L^2}. \quad (50)$$

Be aware that the fit parameters have some units, as given in Eq. 47.

In this discussion, it is assumed that the method is performed at a location where no dispersion D is present. The lattice function dispersion D gives rise to an additional contribution to the beam width Δx through the momentum deviation Δp of the particles with respect to the mean momentum p_0 as $\Delta x = D \cdot \Delta p / p_0$. The dispersion effect is added in a quadratic manner to the measured beam width,

as $x_{\text{rms}}^2 = \sigma_{11}(0) + (D \cdot \Delta p/p_0)^2$. To avoid measurement of the lattice function D and the beam's longitudinal momentum spread, the location for emittance determination should be dispersion-free.

The described method is based on linear transformations and conservation of emittance during manipulation by the quadrupole. Moreover, an elliptical shape of the emittance is assumed. Depending on the general beam properties, this is a good assumption, as long as non-linear effects, such as aberration of magnets by higher-order field contributions or space charge forces are small. If the investigations are conducted with intense beams, an emittance blow-up may occur, depending on the particle density, i.e., on the beam size, but the size is to be changed and even a waist must be created. For high-intensity beams, self-consistent, iterative algorithms must be applied to obtain an estimate of the emittance at the quadrupole entrance, see, e.g., Refs. [108, 109], and references therein.

5.4 'Three-grid' method

Instead of varying a quadrupole, the beam profiles at different locations along a transfer line can be measured with fixed magnet settings. This is easier to achieve at long transfer lines, where the profile monitors are installed, in any case. There is no general restriction to the involved optics, as long as they can be described by linear optics, e.g., dipoles can be included with their known transfer matrix $\mathbf{R}_{\text{dipole}}$.

The profile must be measured at three or more locations, see Fig. 74. For good accuracy, one profile monitor should be close to a beam waist. To determine the beam matrix elements $\sigma_{ij}(0)$ at the entrance of the line s_0 , the profile widths and, therefore, the beam matrix elements $\sigma_{11}(n)$ are determined at n different locations s_n . A system of redundant linear equations for the entrance emittance $\sigma_{ij}(0)$ is given by

$$\begin{aligned} \sigma_{11}(1) &= R_{11}^2(1) \cdot \sigma_{11}(0) + 2R_{11}(1)R_{12}(1) \cdot \sigma_{12}(0) + R_{12}^2(1) \cdot \sigma_{22}(0), & \mathbf{R}(1) : s_0 \rightarrow s_1 \\ \sigma_{11}(2) &= R_{11}^2(2) \cdot \sigma_{11}(0) + 2R_{11}(2)R_{12}(2) \cdot \sigma_{12}(0) + R_{12}^2(2) \cdot \sigma_{22}(0), & \mathbf{R}(2) : s_0 \rightarrow s_2 \\ &\vdots \\ \sigma_{11}(n) &= R_{11}^2(n) \cdot \sigma_{11}(0) + 2R_{11}(n)R_{12}(n) \cdot \sigma_{12}(0) + R_{12}^2(n) \cdot \sigma_{22}(0), & \mathbf{R}(n) : s_0 \rightarrow s_n. \end{aligned} \quad (51)$$

This formula is comparable to the quadrupole variation (Eq. 43), but the transfer matrix $\mathbf{R}(i)$ now describes the beam transport from the starting point of the transfer line s_0 to the location of the individual measurements s_i . The algorithm of the emittance calculation (least square fit or normal equations) is the same as for the quadrupole scan. Such a measurement is shown in Fig. 76, compared with the fitted beam envelope, to enable visualization of possible errors. In practice, the parameters of the entrance ellipse are fitted to match the measured profiles using a linear optics code (e.g., MADX, WinAgile) for this transfer line.

To obtain a reliable measurement, the transfer matrix $\mathbf{R}(n)$ should be an adequate description of the action of the optical elements on the beam. In particular, one must ensure that the beam centre passes the quadrupoles along their magnetic axes, i.e., no 'steering' of the quadrupoles is present. This might be a source of errors in practical situations. As discussed before, no emittance growth, e.g., owing to space charge forces, is assumed here.

The algorithm is not limited to straight transport lines. If a dipole magnet is also present, one must take its action on the beam into account. This results in a dispersion D , i.e., a coupling between the momentum spread $\delta = \Delta p/p$ and the transverse beam size, with $\Delta x = D \cdot \Delta p/p$. For the transport matrix, we get an additional matrix element R_{13} . Also, a dipole has an influence on the angular distribution, called the angular dispersion, resulting in an additional matrix element R_{23} . The single-particle trajectory is now made of a three-dimensional vector $\vec{x} = (x, x', \Delta p/p)$ and the transfer matrix \mathbf{R} is now a 3×3 matrix. The effect of dispersion must be included in the symmetric beam matrix σ , with three new elements, σ_{13} , σ_{23} and σ_{33} . To determine the values of these beam matrix elements, at least

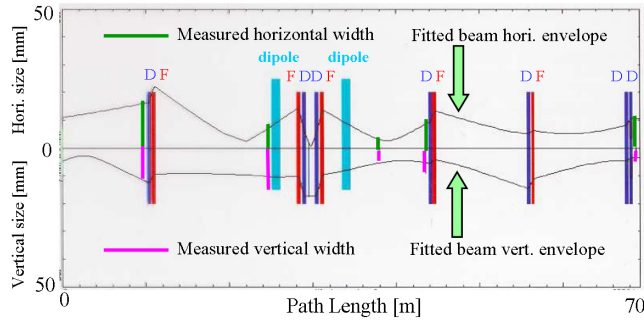


Fig. 76: Determination of beam envelope by linear transformations using different profile measurements. The width of the profile is shown as green lines, measured at a transfer line at GSI. Top: Horizontal direction. Bottom: Vertical direction.

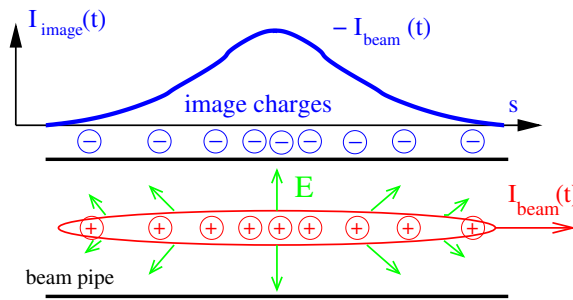


Fig. 77: The beam current induces a wall current of the same magnitude and time structure but reversed polarity

six profile measurements must be made, resulting in at least six equations in the (redundant) system of linear equations for $\sigma_{ij}(0)$ in Eqs. 43 and 51.

6 Beam position monitors

The longitudinal bunch shape, as well as the position of a beam, is very frequently determined using pick-up plates. The idea is to measure, on an insulated metal plate, the image current induced by the electromagnetic field of the beam particles, see Fig. 77. Because the electric field of a bunched beam is time-dependent, an a.c. signal is seen on the plate and the coupling is achieved using RF technologies. Only time-varying signals can be detected by this principle, as generated by a bunched beam. By contrast with bunched beams, the position for a d.c. beams, such as, e.g., behind an ion source in the low-energy transfer lines or beams slowly extracted from a synchrotron, cannot be detected by this method; in this case, the position is determined from the profile measurement. The principle signal shape, as well as the most often used types of pick-up are described. The application is the determination of the beam position, i.e., the transverse centre of mass of the bunches. To this end, four pick-up plates are installed and the difference of the signals yields the centre of mass in both transverse axes. The device with the plates is called the pick-up; the corresponding installation for the centre-of-mass determination is referred to as a beam position monitor (BPM). Using this instrument, the beam position is determined in transfer lines and in synchrotrons. Various measurements based on this position information are possible but are only discussed briefly at the end of this section.

6.1 Signal treatment of capacitive pick-ups

As shown in Fig. 78, a capacitive pick-up consists of a plate or ring inserted in the beam pipe. Here the induced image charge of the beam is coupled via an amplifier for further processing. The plate, at a

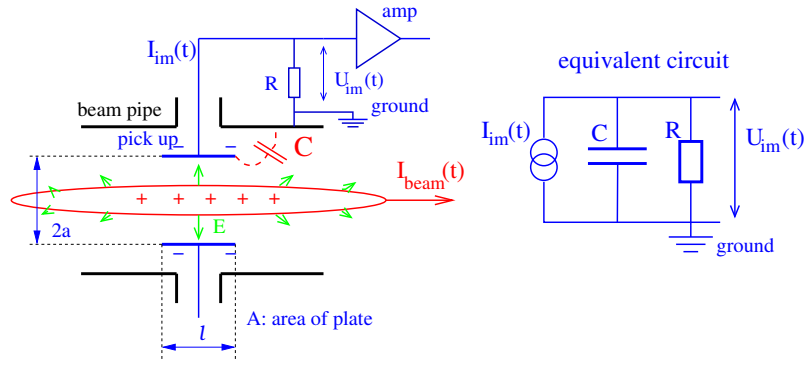


Fig. 78: Scheme of a pick-up electrode and its equivalent circuit

distance a from the beam centre, has an area A and a length in the longitudinal direction l . The current I_{im} driven by the image charge Q_{im} as a function of time t is

$$I_{\text{im}}(t) \equiv \frac{dQ_{\text{im}}}{dt} = -\frac{A}{2\pi a l} \cdot \frac{dQ_{\text{beam}}(t)}{dt}. \quad (52)$$

Having a beam with velocity β , we can write, for the derivative of the beam charge $dQ_{\text{beam}}(t)/dt$,

$$\frac{dQ_{\text{beam}}(t)}{dt} = \frac{l}{\beta c} \frac{dI_{\text{beam}}}{dt} = -\frac{l}{\beta c} \cdot i\omega I_{\text{beam}}(\omega), \quad (53)$$

where the beam current is expressed in the frequency domain using the angular frequency ω as $I_{\text{beam}} = I_0 e^{-i\omega t}$. (More precisely, the derivative of a function df/dt can be expressed as a multiplication of its Fourier transformation $\tilde{f}(\omega)$ by $-i\omega$.) Combining Eqs. 52 and 53, the image current can be written as

$$I_{\text{im}}(t) = \frac{1}{\beta c} \cdot \frac{A}{2\pi a} \cdot i\omega I_{\text{beam}}. \quad (54)$$

As the signal, we use the voltage drop across a resistor R :

$$U_{\text{im}}(\omega) = R \cdot I_{\text{im}}(\omega) = Z_t(\omega, \beta) \cdot I_{\text{beam}}(\omega). \quad (55)$$

For all types of pick-up plate, the general quantity of longitudinal transfer impedance $Z_t(\omega, \beta)$ is defined by Eq. 55 in the frequency domain according to Ohm's law; for a more detailed discussion, see Refs. [110–113]. The transfer impedance describes the effect of the beam on the pick-up voltage and depends on frequency, the velocity of the beam particles β and geometrical factors. It is very helpful to make the description in the frequency domain, where the independent variable is the angular frequency ω , related to the time domain by Fourier transformation.

The frequency-domain function $\tilde{f}(\omega)$ is calculated from the time-domain function $f(t)$ by Fourier transformation as

$$\tilde{f}(\omega) = \int_{-\infty}^{\infty} f(t) \cdot e^{-i\omega t} dt. \quad (56)$$

By inverse transformation, the time-domain function can be recovered as

$$f(t) = \frac{1}{2\pi} \int_{-\infty}^{\infty} \tilde{f}(\omega) \cdot e^{i\omega t} d\omega, \quad (57)$$

if the given integral for $\tilde{f}(\omega)$ exists. Normally, the absolute value, $|\tilde{f}(\omega)|$, also called the amplitude or magnitude, and the phase, $\tan \varphi = \text{Re}(\tilde{f})/\text{Im}(\tilde{f})$, of this complex (in a mathematical sense) function are displayed.

The pick-up of Fig. 78 has a certain capacitance C , which is determined by the distance of the plate from the beam pipe and a capacitance contributed by the cable between the plate and the amplifier input. This amplifier has an input resistance R . Using a current source to model the beam and the parallel connection of the equivalent circuit, we can write its impedance Z as

$$\frac{1}{Z} = \frac{1}{R} + i\omega C \iff Z = \frac{R}{1 + i\omega RC}. \quad (58)$$

Inserting this impedance into Ohm's law, as given in Eq. 55, and using the expression for the image current of Eq. 54, the measurable voltage of the pick-up is

$$U_{\text{im}} = \frac{R}{1 + i\omega RC} \cdot I_{\text{im}} = \frac{1}{\beta c} \cdot \frac{1}{C} \cdot \frac{A}{2\pi a} \cdot \frac{i\omega RC}{1 + i\omega RC} \cdot I_{\text{beam}} \equiv Z_t(\omega, \beta) \cdot I_{\text{beam}}, \quad (59)$$

which results in a general transfer impedance

$$Z_t(\omega, \beta) = \frac{1}{\beta c} \cdot \frac{1}{C} \cdot \frac{A}{2\pi a} \cdot \frac{i\omega RC}{1 + i\omega RC}. \quad (60)$$

This is a description of a first-order high-pass filter for the transfer impedance $Z_t(\omega, \beta)$ with a cut-off frequency $f_{\text{cut}} = \omega_{\text{cut}}/2\pi = (2\pi RC)^{-1}$. For the so-called linear-cut pick-ups used at proton synchrotrons (see later), a typical value of the capacitance is $C = 100$ pF, with a length $l = 10$ cm. The high-pass characteristic is shown in Fig. 79 for a 50Ω and a high-impedance $1 \text{ M}\Omega$ amplifier input resistor. In the figure, the absolute value

$$|Z_t| = \frac{1}{\beta c} \cdot \frac{1}{C} \cdot \frac{A}{2\pi a} \cdot \frac{\omega/\omega_{\text{cut}}}{\sqrt{1 + \omega^2/\omega_{\text{cut}}^2}} \quad \text{and the phase relation} \quad \varphi = \arctan(\omega_{\text{cut}}/\omega) \quad (61)$$

are shown. A pick-up has to match the interesting frequency range, which is given by the accelerating frequency and the bunch length. In a proton synchrotron, typical values of the accelerating frequency are in the range 1–10 MHz, while for linacs and electron synchrotrons, frequencies in the range 100 MHz to 3 GHz are typically used.

We can distinguish two extreme cases for the transfer impedance of Eq. 60.

– *High-frequency range* $\omega \gg \omega_{\text{cut}}$. Here, the transfer impedance converges to

$$Z_t \propto \frac{i\omega/\omega_{\text{cut}}}{1 + i\omega/\omega_{\text{cut}}} \longrightarrow 1. \quad (62)$$

The resulting voltage drop at R is, for this case,

$$U_{\text{im}}(t) = \frac{1}{\beta c C} \cdot \frac{A}{2\pi a} \cdot I_{\text{beam}}(t). \quad (63)$$

Therefore, the pick-up signal is a direct image of the bunch time structure with no phase shift, i.e., $\varphi = 0$. To get a low cut-off frequency, $\omega_{\text{cut}} = 1/RC$, high-impedance input resistors are used to monitor long bunches, e.g., in a proton synchrotron. The calculated signal shape is shown in the right-hand panel of Fig. 80. Note that a 50Ω termination is considered in Fig. 80, leading to a large value of the cut-off frequency, $f_{\text{cut}} = 32$ MHz. In the application of a proton synchrotron, high-impedance ($\sim 1 \text{ M}\Omega$) termination yields a much smaller value of the cut-off frequency, $f_{\text{cut}} = 10$ kHz in this case, as shown in Fig. 79, where the condition corresponds to the enlarged flat part of the depicted transfer impedance. A typical signal from this circuit is given in Fig. 81.

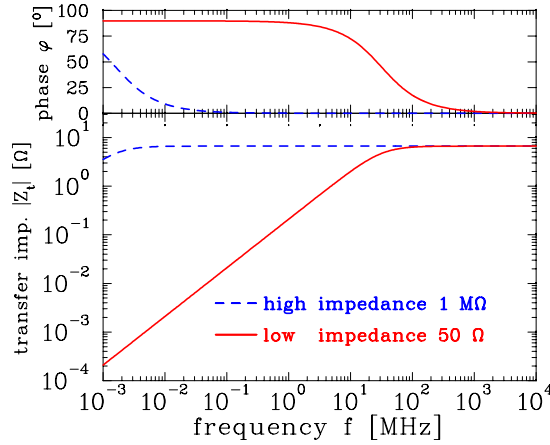


Fig. 79: Absolute value and phase of the transfer impedance for an $l = 10$ cm long cylindrical pick-up with a capacitance of $C = 100$ pF and an ion velocity of $\beta = 50\%$ for high ($1 \text{ M}\Omega$) and low (50Ω) input impedances of the amplifier.

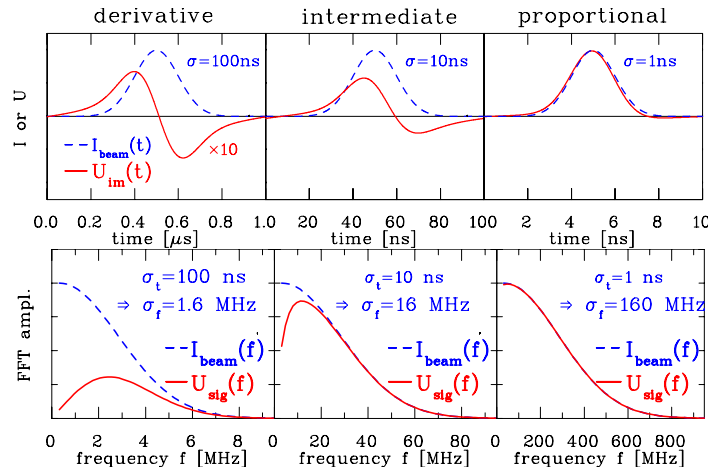


Fig. 80: Simulation of image voltage $U_{\text{im}}(t)$ for the values of the pick-up used in Fig. 79 terminated with $R = 50 \Omega$ for three different bunch lengths of Gaussian distribution, with $\sigma = 100$ ns, 10 ns, and 1 ns, respectively. The cut-off frequency f_{cut} is 32 MHz. Note the different time scales. (The bunch length in the last case is artificially short for a proton synchrotron.) A Gaussian function in the time domain of width σ_t has a Fourier transformation described by a Gaussian function of width $\sigma_f = 1/(2\pi\sigma_t)$, centred at $f = 0$.

– *Low-frequency range* $\omega \ll \omega_{\text{cut}}$. The transfer impedance here is

$$Z_t \propto \frac{i\omega/\omega_{\text{cut}}}{1 + i\omega/\omega_{\text{cut}}} \longrightarrow i \frac{\omega}{\omega_{\text{cut}}}. \quad (64)$$

Therefore, the voltage across R is, in this case,

$$U_{\text{im}}(t) = \frac{R}{\beta c} \cdot \frac{A}{2\pi a} \cdot i\omega I_{\text{beam}} = -\frac{R}{\beta c} \cdot \frac{A}{2\pi a} \cdot \frac{dI_{\text{beam}}}{dt}, \quad (65)$$

again using the frequency-domain relation $I_{\text{beam}} = I_0 e^{-i\omega t}$. We see that the measured voltage is proportional to the derivative of the beam current. This can also be seen from the phase relation of the high-pass filter in Fig. 79, where a phase shift of 90° corresponds to a derivative. The signal

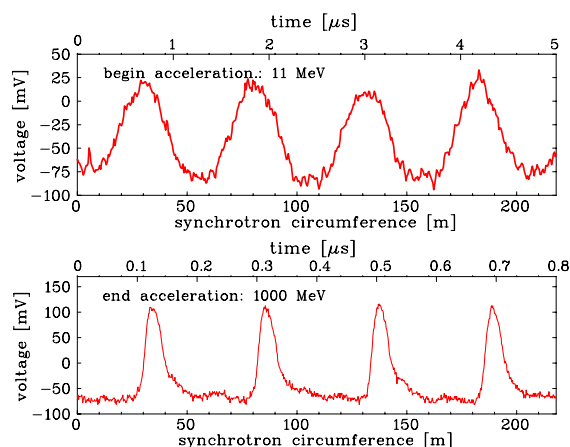


Fig. 81: Bunch signals from a ‘shoebox’ pick-up for $1\text{ M}\Omega$ termination, as installed at the GSI ion synchrotron. Top: Bunches of the proton beam along the synchrotron circumference at the start of the acceleration. Bottom: Bunches of the proton beam along the synchrotron circumference after attaining the final energy. Note the different time scales.

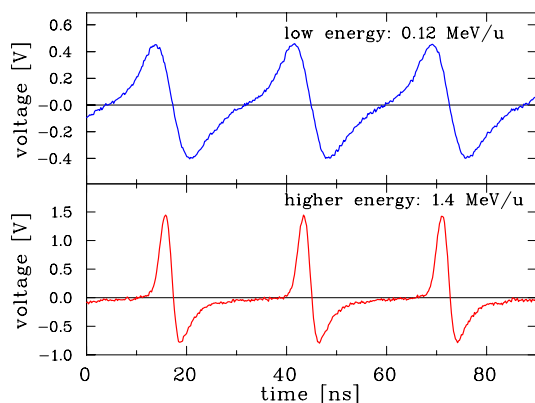


Fig. 82: Bunch signal from a capacitive pick-up at the GSI ion linac. Top: 0.12 MeV/u . Bottom: 1.4 MeV/u . The derivative behaviour is caused by $50\ \Omega$ termination to achieve a large bandwidth of the amplifier. The accelerating frequency is 36 MHz .

is bipolar, as shown in the left-hand panel of Fig. 80. A measurement from the GSI linac, which fulfils this condition, is shown in Fig. 82.

The signal at the amplifier output depends on the frequency range, as compared with the cut-off frequency. Of course, the bunches are not pure sine waves; therefore, it might be that a mixture of proportional and derivative components are present, see the middle panel of Fig. 80. In general, the signal shape, as depicted in Fig. 80, can be calculated for the different parameters using the transfer impedance concept by the following steps.

- The beam current $I_{\text{beam}}(t)$ is Fourier transformed, yielding $\tilde{I}_{\text{beam}}(\omega)$.
- This is then multiplied by $Z_t(\omega)$, yielding the frequency-dependent voltage $\tilde{U}_{\text{im}}(\omega) = Z_t(\omega) \cdot \tilde{I}_{\text{beam}}(\omega)$.
- To retrieve the time-dependent signal, the inverse Fourier transformation is applied, yielding $U_{\text{im}}(t)$.

With respect to the different limits of the transfer impedance, two important applications are discussed for illustration.

- *Range $\omega \gg \omega_{\text{cut}}$ realized by low ω_{cut} due to high impedance.* In a proton or ion synchrotron, a low frequency is used for acceleration in the range of $f_{\text{acc}} = 1\text{--}10$ MHz, resulting in bunches of several metres in length. In these machines, large apertures are, necessarily, typically $a = 10$ cm, reducing the transfer impedance due to $Z_t \propto 1/a$. To increase sensitivity, the length of the pick-up in the beam direction is increased, typically $l \sim 10$ cm as $Z_t \propto l$. Note that the pick-up length is still much shorter than the bunch length. To have a flat curve of the sensitivity, i.e., a large bandwidth, a low value of $\omega_{\text{cut}} = 1/RC$ is used by feeding the signal into a high-impedance field-effect transistor as the first step of the amplifier. A bandwidth of the amplifier circuit of 100 MHz can be achieved, but it is difficult to build amplifier circuits with larger bandwidths. To prevent signal degeneration due to the limited amplifier bandwidth, the application of high-impedance amplifiers is restricted to proton or ion synchrotrons with acceleration frequencies less than ~ 10 MHz. Observation of the contribution in the bunch spectrum from the tenth harmonic of the acceleration frequency is sufficient for most applications. Figure 81 shows that a direct image of the bunch is seen in this case.
- *Range $\omega \ll \omega_{\text{cut}}$ realized by high ω_{cut} due to 50Ω impedance.* At proton linacs and all electron accelerators, the bunches are short, up to the millimetre range, owing to the higher accelerating, $f_{\text{acc}} = 100$ MHz to 3 GHz. Firstly, one does not gain signal strength by increasing the length l . Secondly, a 50Ω termination is used to prevent reflections and achieve smooth signal processing with a large bandwidth, up to several gigahertz. The short l , and therefore smaller capacitance C , along with $R = 50 \Omega$, leads to a high value of ω_{cut} ; the derivative of the bunches is seen, as displayed in Fig. 82.

The foregoing discussion does not take into account the effect of the frequency response of the associated cables or other band-limiting electronics; see Refs. [111, 114] for a more detailed discussion. Further on, the fact that a pick-up has a high-pass characteristic leads to the fact that a d.c. beam cannot be detected (d.c. beam detectors are available, e.g., behind the ion source or for a transfer line during slow extraction).

6.2 Characteristics for position measurement by BPMs

The deviation of the beam centre with respect to the centre of the vacuum chamber is frequently monitored using four isolated plates or buttons by determining the voltage difference $\Delta U_x = U_{\text{right}} - U_{\text{left}}$ or $\Delta U_y = U_{\text{up}} - U_{\text{down}}$ of opposite plates. A shorter distance from one of the plates leads to a higher induced voltage. This is called the ‘proximity effect’; it is shown schematically in Fig. 83. Normalizing to the total signal $\Sigma U_x = U_{\text{right}} + U_{\text{left}}$, the horizontal displacement x can be obtained via

$$x = \frac{1}{S_x} \cdot \frac{U_{\text{right}} - U_{\text{left}}}{U_{\text{right}} + U_{\text{left}}} = \frac{1}{S_x} \cdot \frac{\Delta U_x}{\Sigma U_x} \quad (\text{horizontal}), \quad (66)$$

which is independent of the beam intensity. For the vertical plane, the position y is given by

$$y = \frac{1}{S_y} \cdot \frac{U_{\text{up}} - U_{\text{down}}}{U_{\text{up}} + U_{\text{down}}} = \frac{1}{S_y} \cdot \frac{\Delta U_y}{\Sigma U_y} \quad (\text{vertical}). \quad (67)$$

This position measurement is the most frequent application of pick-ups; hence, they are called beam position monitors (BPMs). The proportional constant S_x (or S_y) between the measured normalized voltage difference and the beam displacement is called the position sensitivity and its unit is %/mm. Sometimes, the inverse is used, $k = 1/S$; this is given in units of millimetres and is called the BPM position constant or position sensitivity. It is possible that the position sensitivity depends on the beam position itself, corresponding to a non-linear voltage response for a large beam displacement and, additionally, on the evaluation frequency; hence, it is a function $S = S(x, y, \omega)$.

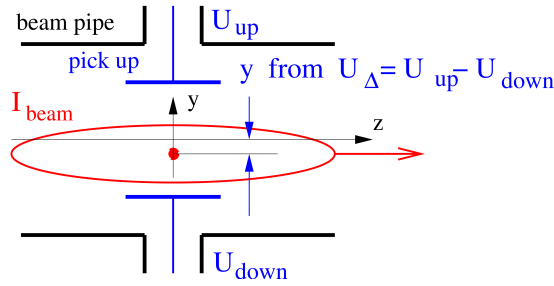


Fig. 83: Schematics of BPM for vertical position reading, based on the proximity effect

For typical beam displacements of less than one-tenth of the beam pipe aperture, the difference ΔU is less by about this factor than the sum voltage ΣU , i.e.,

$$\text{typically } \Delta U < \frac{\Sigma U}{10} . \quad (68)$$

Sensitive signal processing is required for the difference voltage, in order to achieve a sufficient signal-to-noise ratio. This concerns the usage of low-noise amplifiers, which must be matched to the signal level. Sometimes, difference and sum voltages are generated by analogue means using so-called Δ – Σ hybrids. For these cases, the difference voltage can be more greatly amplified than the sum signal (typically amplification by 10 dB corresponds a factor of three for the voltage amplification) to match the optimal signal level for the successive electronics or analogue-to-digital conversion. The most effective noise reduction is achieved by limitation of the signal processing bandwidth, because the thermal noise voltage U_{eff} at a resistor R scales with the square root of the bandwidth Δf as $U_{\text{eff}} = \sqrt{4k_{\text{B}}TR\Delta f}$, where k_{B} is the Boltzmann constant and T is the temperature. The bandwidth limitation is performed by band-pass filtering at a harmonics of this frequency or mixing with the accelerating frequency in narrowband processing, as discussed in Section 6.5. A review of general BPM properties and BPM types is given in Refs. [110–113].

6.3 Position measurement using button pick-ups

For a round arrangement of buttons, a simple two-dimensional electrostatic model can be used to calculate the voltage difference as a function of beam displacement. As shown in Fig. 84, we assume a thin, ‘pencil’ beam having a transverse extension much smaller than the beam pipe radius of current I_{beam} , which is located off-centre by distance r at an angle θ . The wall current density j_{im} at the beam pipe, of radius a , is given as a function of the azimuthal angle ϕ as

$$j_{\text{im}}(\phi) = \frac{I_{\text{beam}}}{2\pi a} \cdot \left(\frac{a^2 - r^2}{a^2 + r^2 - 2ar \cdot \cos(\phi - \theta)} \right) \quad (69)$$

and is depicted in Fig. 84; see Ref. [115] for a derivation of this formula.

As discussed, this represents the proximity effect, where the current density depends on the distance from the beam centre. The button-type BPM electrodes cover an angle α ; the image current I_{im} is recorded as

$$I_{\text{im}} = a \int_{-\alpha/2}^{+\alpha/2} j_{\text{im}}(\phi) d\phi . \quad (70)$$

The resulting signal difference for opposite plates as a function of horizontal beam displacement, corresponding to $\theta = 0^\circ$, shows a significant non-linear behaviour, as displayed in Fig. 85. The signal voltage is calculated according to Eq. 55 as $U = R \cdot I_{\text{im}}$. It can be seen that, for the normalized difference

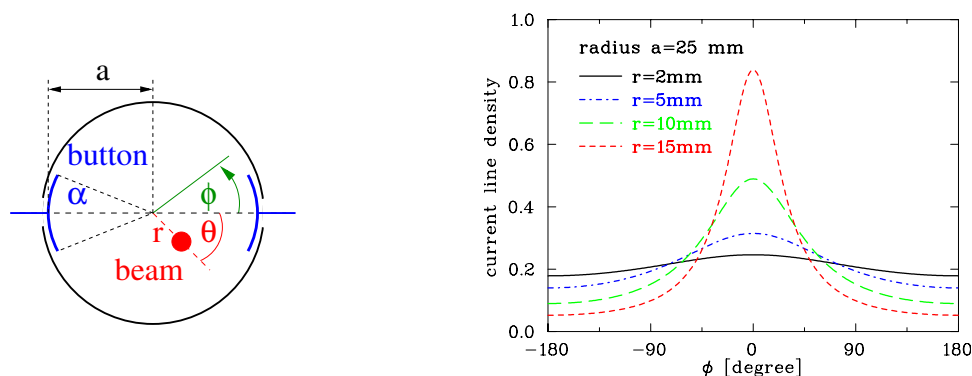


Fig. 84: Left: Schematics for a button BPM. Right: Image current density generated by a ‘pencil’ beam at different displacements r for an azimuth $\theta = 0$.

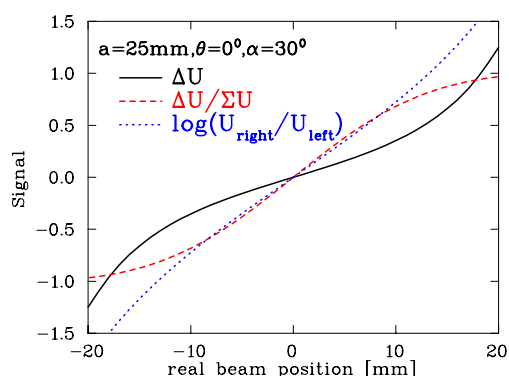


Fig. 85: Difference voltage, normalized difference and logarithmic ratio for a button BPM arrangement of angular coverage $\alpha = 30^\circ$ as a function of horizontal beam displacement, i.e., $\theta = 0$ for a beam pipe radius $a = 25$ mm.

$\Delta U/\Sigma U$, the linear range continues to larger beam offsets. The non-linearity increases if the beam centre moves outside the horizontal axis, as depicted in Fig. 86 for different values of the azimuthal orientation θ as a function of horizontal displacement $x = r \cdot \cos \theta$, according to Eqs. 69 and 70. For an orientation along the diagonal line $\theta = 45^\circ$, a significant deviation from linearity starts for this case, even at about one-quarter of the beam pipe radius. This non-linearity can be influenced by the button size, as represented in this two-dimensional approach by the angle α . However, in the central part, the reading is almost independent of orientation, leading to a universal position sensitivity S . The dependence between the horizontal and vertical planes is better depicted in the right-hand panel of Fig. 86. Here, real beam positions are plotted at equidistant steps, as well as the results obtained using $1/S \cdot \Delta U/\Sigma U$ calculations with S fitted at the central part. The preceding two-dimensional electrostatic model delivers satisfying result for typical electron beams of relativistic beam velocities, i.e., TEM-like field pattern; only minor corrections are necessary in the case of a circular pick-up.

If the beam is accelerated to a non-relativistic velocity, $\beta \ll 1$, and has a bunch length less than 1 cm, as is often the case for proton linacs and cyclotrons, the electric field can no longer be described by a TEM wave. Instead, the field pattern, as originated by the charged particles, has a significant longitudinal extension because the electric field propagation is faster than the beam velocity (see the discussion in Section 7.1). Moreover, this field pattern, and therefore the wall current, depends strongly on the beam displacement for opposite BPM plates, resulting in velocity dependence of the position sensitivity $S(v)$. This is discussed analytically in Ref. [116]; a numerical example is given in Ref. [117, 118].

A BPM arrangement with circular beam pipe geometry, installed at CERN LHC, is depicted in Fig. 87. Owing to the size and the round electrodes, this arrangement is commonly called a button BPM.

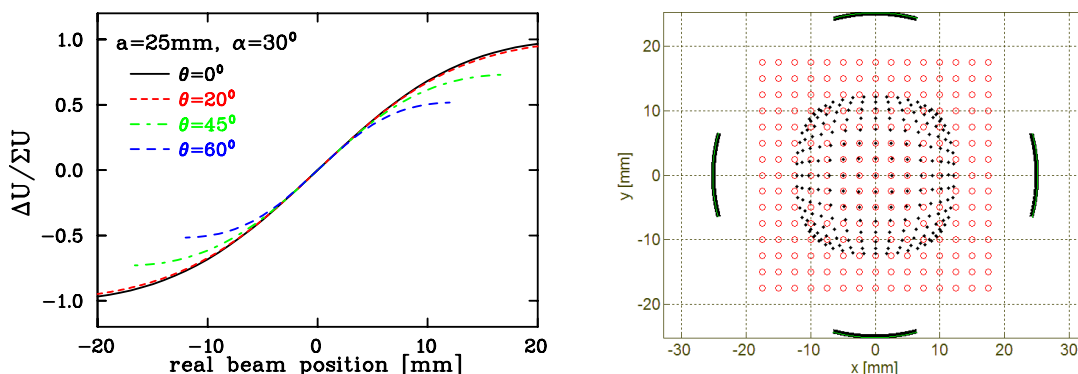


Fig. 86: Left: Calculated horizontal position for different azimuthal beam orientation θ for the parameters of Fig. 85. Right: In the position map, the open circles represent the real beam position and the dots are the results of the $1/S \cdot \Delta U/\Sigma U$, with $S = 7.4 \text{ \%/mm}$ for the central part.

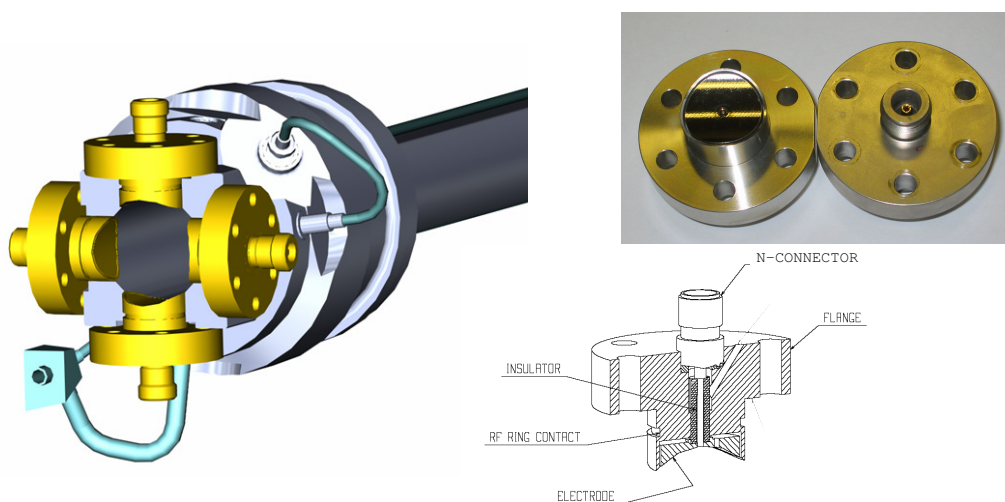


Fig. 87: Left: Installation of curved $\varnothing 24 \text{ mm}$ button BPMs at the LHC beam pipe of $\varnothing 50 \text{ mm}$ [119, 120]. Right: Photograph and technical drawing of BPM used at LHC: the air side is equipped with a N-connector.

The reason for such an installation is to ensure a smooth transition from the regular beam pipe to the BPM region and to prevent excitation of an electromagnetic field, the so-called wakefield, by the beam. In most other cases, planar buttons are used, owing to their simpler mechanical realization.

Button pick-ups are the most popular devices for electron accelerators. A button pick-up consists of a circular plate, typically 10 mm diameter, mounted flush with the vacuum chamber. The cross-section of the chamber is not changed by this insertion, to avoid excitation of wakefields by the beam. The button itself should have a short vacuum feed-through with a smooth transition to the $50 \text{ } \Omega$ cable, to avoid excitation of standing waves and to reach a bandwidth up to 10 GHz.

6.4 ‘Shoobox’ pick-ups using the so-called linear cut

Owing to the long bunches at proton or ion synchrotrons, typically several metres, long electrodes, typically 20 cm, are installed to enhance the signal strength. A box-like device is usually used, to achieve a precise linear dependence with respect to the beam displacement, see Fig. 88. For the previously discussed button pick-up geometries, the signal of the plate closer to the beam’s centre of mass is larger than that of the more distant plate; this is called the proximity effect. By contrast, shoobox pick-ups are based on another principle. The influenced signal is proportional to the actual plate length at the beam

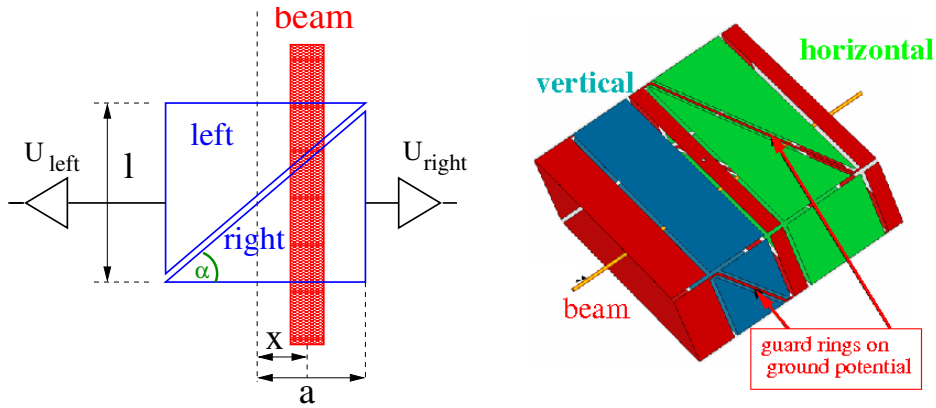


Fig. 88: Left: Position measurement using the so-called linear cut and an example of an electrode arrangement for the horizontal plane. Right: Linear-cut BPM for both planes.

centre position. For a given beam displacement x , the electrode's image voltage U_{im} is proportional to the lengths l_{left} and l_{right} of the beam projected on the electrode surface, as shown for the horizontal direction in the left-hand panel of Fig. 88. For triangle electrodes with half-aperture a , one can write:

$$l_{\text{right}} = (a + x) \cdot \tan \alpha \quad \text{and} \quad l_{\text{left}} = (a - x) \cdot \tan \alpha \quad \implies \quad x = a \cdot \frac{l_{\text{right}} - l_{\text{left}}}{l_{\text{right}} + l_{\text{left}}} . \quad (71)$$

The position reading is linear and can be expressed by the image voltages as

$$x = a \cdot \frac{U_{\text{right}} - U_{\text{left}}}{U_{\text{right}} + U_{\text{left}}} \equiv \frac{1}{S_x} \cdot \frac{\Delta U_x}{\Sigma U_x} \quad \implies \quad S_x = \frac{1}{a} , \quad (72)$$

which shows that the position sensitivity for this ideal case is simply given by the inverse of the half-aperture. Compared with other types of pick-up, the position sensitivity is constant for almost the full range of displacements, i.e., nearly no corrections for non-linearity are required [121]. This is demonstrated in Fig. 89; numerical simulations show a linear scaling of the difference voltage ΔU_x of opposite plates normalized to the sum voltage ΣU_x as a function of beam offset up to about two-thirds of the half-aperture. Moreover, the position reading in the horizontal plane is independent of the beam position in the vertical plane. Owing to the linearity, the position reading is independent of the beam size, which is of importance for the relatively large beam size compared with the chamber aperture for low-energy proton or ion synchrotrons. This position linearity is the main advantage of the linear-cut type over the button BPM type. An analogue signal from such a linear-cut BPM used at an ion synchrotron is shown in Fig. 81.

As a summary, the basic parameters for linear-cut and button BPMs are compared in Table 12; this table contains significant simplifications and serves as an overview only.

For position measurement, other techniques are also used, including the measurement of the magnetic field with so-called inductive pick-ups or the excitation of cavity modes within a so-called cavity BPM. Further descriptions and citations can be found in Refs. [110, 112, 113, 122].

6.5 Electronic treatment for position determination

To determine the position of the beam, the signals from the electrodes must be compared. For this comparison, the signal shape (derivative or proportional behaviour) is of minor importance. The electronics used for this purpose are described only briefly in this contribution; a detailed review is given in Refs. [123–125]. For position resolution, the signal-to-noise ratio is important. Beside the stray fields from the RF cavities, the broadband amplifier noise and the electronic noise of the subsequent devices

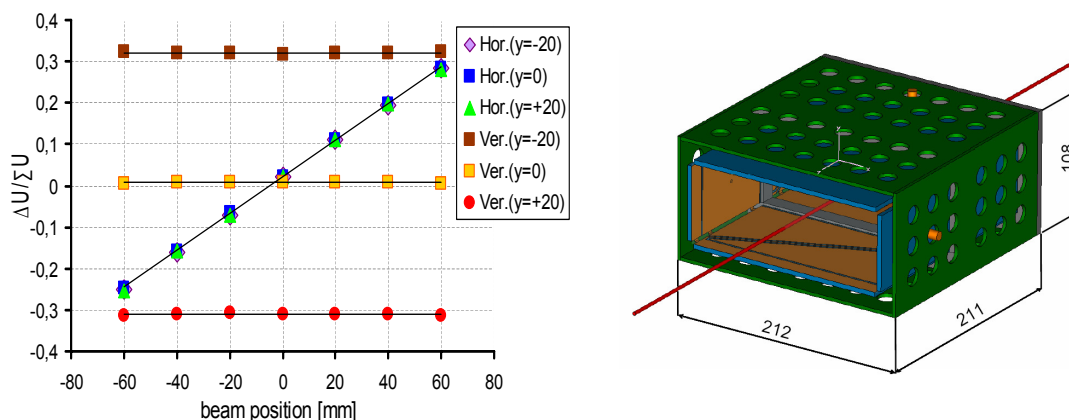


Fig. 89: Left: Numerical calculation of position reading, $\Delta U/\Sigma U$, as a function of beam displacement for the horizontal plane. The simulated beam is swept in the horizontal direction (curves with constant slope) and vertical direction (constant functions) and proves the decoupling of both planes [121]. Right: BPM geometry for these calculations, with horizontal half-aperture $a = 100$ mm, vertical half-aperture $b = 35$ mm and length 211 mm, comparable to the BPM shown in Fig 90.

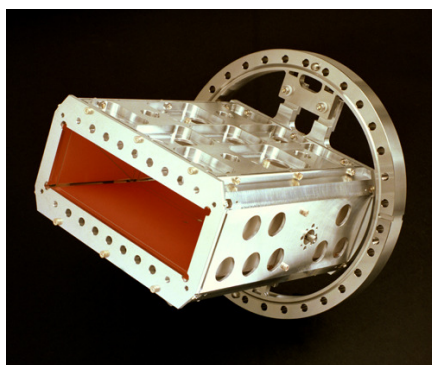


Fig. 90: Linear-cut position pick-up with an aperture limitation of $200 \times 70 \text{ mm}^2$, from the GSI synchrotron ring

Table 12: Simplified comparison of linear-cut and button BPMs

	Linear-cut BPM	Button BPM
Precaution	Bunches longer than BPM	Bunches comparable to BPM
Length (typical)	10–20 cm per plane	$\varnothing 0.5\text{--}5$ cm
Shape	Rectangular or cut cylinder	Orthogonal or planar orientation
Mechanical realization	Complex	Simple
Coupling	Often $1 \text{ M}\Omega$, sometimes 50Ω	50Ω
Capacitance (typical)	30–100 pF	3–10 pF
Cut-off frequency (typical)	1 kHz for $R = 1 \text{ M}\Omega$	0.3–3 GHz for $R = 50 \Omega$
Usable bandwidth (typical)	0.1–100 MHz	0.3–5 GHz
Linearity	Very linear, no $x\text{--}y$ coupling	Non-linear, $x\text{--}y$ coupling
x -position sensitivity	Good	Good
Usage	Proton synchrotron, $f_{\text{acc}} < 10 \text{ MHz}$	Proton linac, all electron accelerators $f_{\text{acc}} > 100 \text{ MHz}$

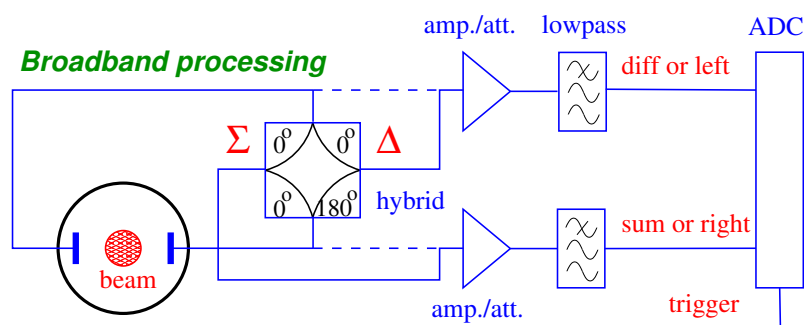
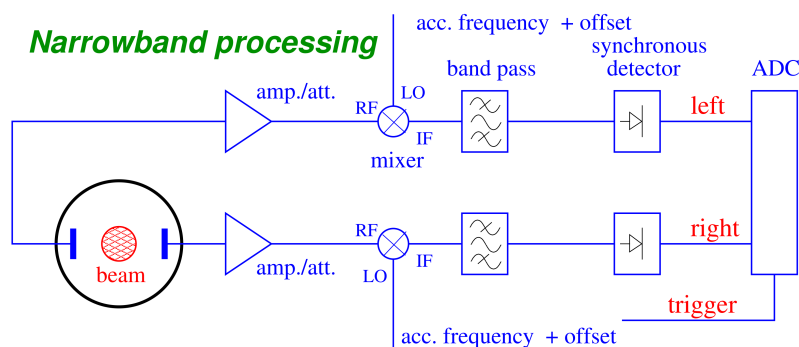
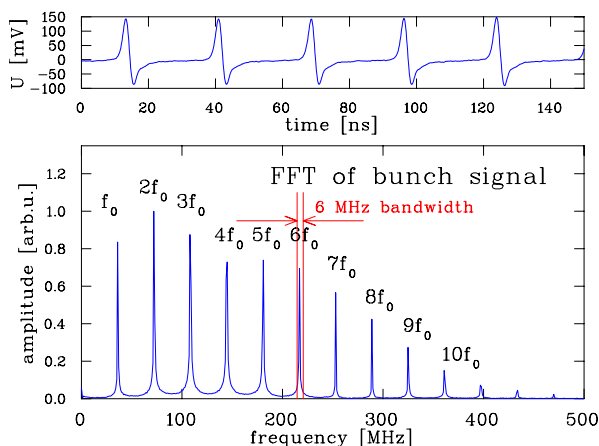


Fig. 91: Broadband signal processing. Plate signals are either fed directly to the amplifier (dashed line) or via a hybrid. The sum and difference signals are generated in an analogue manner (solid line).

have an effect. Therefore, a minimum bunch current is necessary for a reliable position measurement. Two different principles are commonly used, based on analogue electronics; so-called broadband and narrowband processing.

Broadband processing. In the broadband case, as shown in Fig. 91, the signals from the individual plates are amplified (or even attenuated) to adapt the signal strength to the ADC input level. The sum and difference signals are then calculated from the digitized values. For noise reduction and alias-product suppression, a low-pass filter is used, matched to the sample rate of the ADC. In older installations, fast sampling was not possible; an external trigger, generated from the bunch passage in an analogue manner, forced the digitalization. In many applications, the sum and difference voltages are analogously generated by a 180° hybrid or a differential transformer. Because these are purely passive devices, they can be mounted quite close to the BPM plates, even when there is high radiation. The resulting sum and difference signals are then stored in the ADC. The difference signal, which is normally smaller by at least a factor of ten, can be amplified by a larger amount than the sum signal to exploit the full ADC range. (An overview of standard RF components can be found in Ref. [126].) The analogue electronics are required to match the signal shape to the properties of the ADCs; an appropriate trigger is used for the digitalization. Modern installations do not use these types of analogue electronics; instead, the signal is digitized directly by fast ADCs or digital receivers, which are even commercially available [127]. With the help of high-speed digital signal processing, the bunch signal is then reduced to one value per bunch and the beam position is calculated from the sum and difference values, see, e.g., Ref. [128]. Broadband processing is less precise than narrowband processing. For electron machines, with small beam size, a resolution of $100\ \mu\text{m}$ can be achieved using broadband processing. The advantage is the possibility of performing bunch-by-bunch analysis (i.e., always measuring the position of the same bunch rotating in a synchrotron) using an appropriate trigger setting or precise digital signal processing. The broadband scheme is installed at transfer lines between synchrotrons, where only one or few bunches are transferred. A further modification is the use of logarithmic amplifiers, which are commercially available, e.g., Ref. [11], and which are often installed at transfer lines; in these, an order-of-magnitude increase of input signal is converted to a linear increase of the output signal. For the typical button BPM arrangement, a good linearity for the position sensitivity is attained, as depicted in Fig. 85. The advantage is that a large dynamic range can be covered by a single amplifier stage without range switching. The disadvantage is the smaller achievable accuracy, which is often acceptable at transfer lines.

Narrowband processing. Narrowband processing is used to obtain a higher precision of the position reading, attaining $1\ \mu\text{m}$ in electron machines using the electronics scheme shown in Fig. 92. The better signal-to-noise ratio is achieved by reducing the bandwidth of the signal processing by several orders of magnitude. As an illustrative example, the Fourier transform of the signal from the GSI linac pick-up is shown in Fig. 93. The spectral power of the signal is mainly available at the bunch repetition harmonics nf_0 . The position evaluation uses only this large signal power within the frequency band


Fig. 92: Signal analysis for narrowband treatment

Fig. 93: Bunch signal (top) and its Fourier transform (bottom) at the GSI linac of a 1.4 MeV/u beam. In the Fourier spectrum, each line corresponds to the indicated harmonic of the 36 MHz accelerating frequency. The position is evaluated at $6f_0 = 216.8$ MHz using 6 MHz narrowband processing, as indicated by the red lines.

Δf , while the thermal noise is reduced as $U_{\text{eff}} \propto \sqrt{\Delta f}$. Technically, the pick-up signal is mixed with the accelerating frequency, e.g., using RF components described in Ref. [126]. The resulting quasi-d.c. signal is then digitized by an ADC and the position calculated via software. In general, this technique is called heterodyne mixing; the same principle is used in a spectrum analyser. The mixing is equivalent to an average over many bunches, leading to much greater precision in the position reading, but does not allow turn-by-turn observation. This method can also be applied for a synchrotron with varying acceleration frequency, e.g., a proton synchrotron for non-relativistic velocities, because the varying accelerating frequency changes in phase with the bunch signal, resulting in a constant intermediate frequency. Such a system is commercially available [11]. Moreover, for a synchrotron, such narrowband processing is applied at linacs or behind cyclotrons with a pulse length greater than 10 μs as, e.g., used for multiturn injection into a synchrotron. If only one or few bunches are transferred, e.g., between two synchrotrons, narrowband processing cannot be applied.

These methods are used to perform BPM signal conditioning in an analogue manner; for most cases, this leads to a small-bandwidth output, which is then digitized with a slow sampling ADC. Motivated by their intensive use in telecommunication, the sampling rate and voltage resolution of ADCs have significantly improved over the last decade; an overview of ADC technology can be found in Ref. [129]. Moreover, digital signal processing capabilities have been enhanced. The tendency of modern technologies is to digitize the signal at an early stage in the signal path and replace the analogue conditioning with digital signal processing, e.g., performing the narrowband treatment in the digital domain.

In most cases, the required parallel processing is realized using a field programmable gate array to ensure fast, real-time, response. On this digital basis, versatile treatments can be implemented without hardware exchange [127, 130], leading to higher flexibility for the application. An example is the filtering of one data set with different bandwidths to match different requirements for position and time resolution; such digitalization and processing units are commercially available [127]. Related methods, compared with analogue treatment, are reviewed in Ref. [125].

6.6 Trajectory measurement

The trajectory indicates the position of a single bunch during its transport through the accelerator; this gives basic information of the initial alignment of the accelerator setting. Because the single-bunch position is monitored, broadband processing is used for the BPM electronics; the reduced position resolution is of minor concern for this measurement.

Figure 94 shows, schematically, typical instrumentation for a transfer line between synchrotrons. It is assumed that this transfer line comprises an entry section, a long central section, with a more or less periodic arrangement of several focusing-defocusing (FODO) cells equipped with a quadrupole and a steerer for each direction, and an exit section with more flexible matching control. The main goal during operation is steering correction of the beam using the BPM readings as inputs. In the optimal case, the correction should be performed independently for the horizontal and vertical directions. Each section has a different task and related instrumentation.

- *Entry section.* The position and angle of the beam are gained from two BPMs spaced a certain distance to achieve good resolution for both parameters. Steering control is most often achieved by changing the values for the septa within the synchrotron. In addition, a profile measurement is foreseen to estimate the validity of the assumed transverse matching and the expectation with respect to the transverse emittance.
- *Central section.* Steering control in the central part can be performed incrementally by modifying the settings of the dipole steerers, which are often installed close to the corresponding focusing quadrupole and separated for the horizontal and vertical directions. The kick produced by an individual steerer is monitored by a BPM, which should be mounted so as to have a betatron phase advance of about $\mu_\beta \simeq 90^\circ$ to transfer the steerer's kick to an offset at the BPM.
- *Exit section.* Beside beam control via a dipole steerer, transverse matching to the closed orbit requirements of the synchrotron is performed by a doublet or even triplet quadrupole, arranged for flexibility, and is checked with a BPM and, additionally, profile measurement. For a fixed target following the transfer line, the same arrangement is chosen in many cases.

In addition to position determination, the sum signal of the BPM can be used for relative estimation of the beam current. Nevertheless, for the absolute current determination, transformers must be installed, at least at the entrance and exit sections, as well as behind possible aperture limits (not depicted in Fig. 94). Beam loss monitors can assist in transmission optimization and are therefore installed at the entrance and exit sections, as well as at possible acceptance limits. In the central section, the possibility of emittance measurement, using the method of quadrupole variation and an additional profile monitor, is normally considered, see Section 5.3.

As an example of a measurement, Fig. 95 depicts the measurement of the trajectory of a single bunch injected into the LHC in the first days of its commissioning [131]. The position reading at each of the 530 BPMs on the 27 km long synchrotron is displayed showing some oscillations caused by mismatched injection parameters, which could be aligned later on with the help of the diagnostics. In this respect, the LHC is treated as a transfer line.

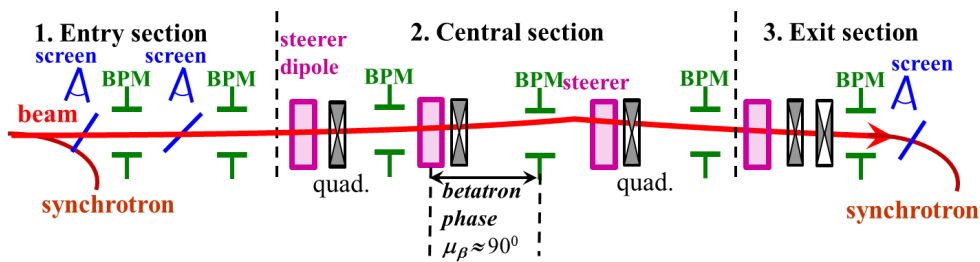


Fig. 94: Typical arrangement of diagnostics in a transfer line for bunched beam transfer between synchrotrons

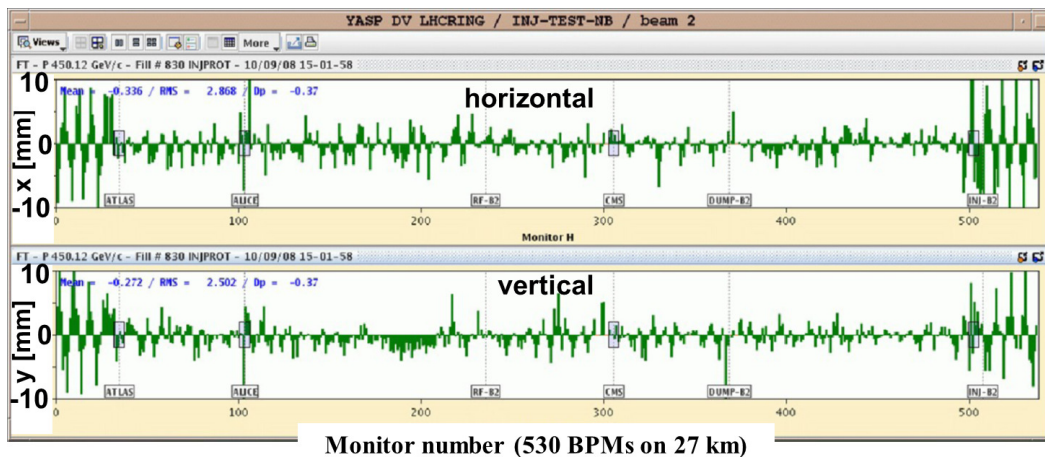


Fig. 95: Measurement of the trajectory of a single bunch injected in the LHC with a position display at the 530 BPMs around the synchrotron [131]. Image from R. Jones (private communication).

6.7 Closed orbit measurement at a synchrotron

It is important, for operation, to match the beam centre from the transfer line to the reference orbit inside the synchrotron. For proton synchrotrons in particular, the reference orbit must be determined to ensure stable storage of the beam without emittance enlargement. The closed orbit is defined by averaging the position over many turns; the required accuracy is of the order of $10\ \mu\text{m}$ for proton accelerators and less than $1\ \mu\text{m}$ for synchrotron light sources. In a synchrotron, several BPMs are installed to determine the closed orbit. As a rule of thumb, a good choice is to have four BPMs per tune value separated by about $\mu_\beta \simeq 90^\circ$ betatron phase advance. The closed orbit is the central beam path along the machine, taking existing imperfections into account. The closed orbit might differ from the ideal path, defined by the centre of the quadrupole magnets. Only for a good alignment does the real beam behave as expected from beam optics calculations, e.g., no beam steering by the quadrupole magnets occurs. An example of the use of position measurement during the acceleration in the GSI synchrotron is given in Fig. 96.

The position reading of the BPMs around the ring can be used as the input of a feedback loop for active beam correction to compensate for systematic and temporal uncertainties, see, e.g., Ref. [132]. Such a feedback system is installed in most synchrotrons. Using the results of the position measurement, various beam parameters for a beam stored in a synchrotron can be determined, such as the tune, chromaticity, and beta function at the BPM location; see Refs. [1–7, 133, 134] for an introduction to those measurements. Comparable methods for beta functions and dispersion determination can be applied to transfer lines as, e.g., described in Ref. [135, 136]. A detailed description is beyond the scope of this contribution.

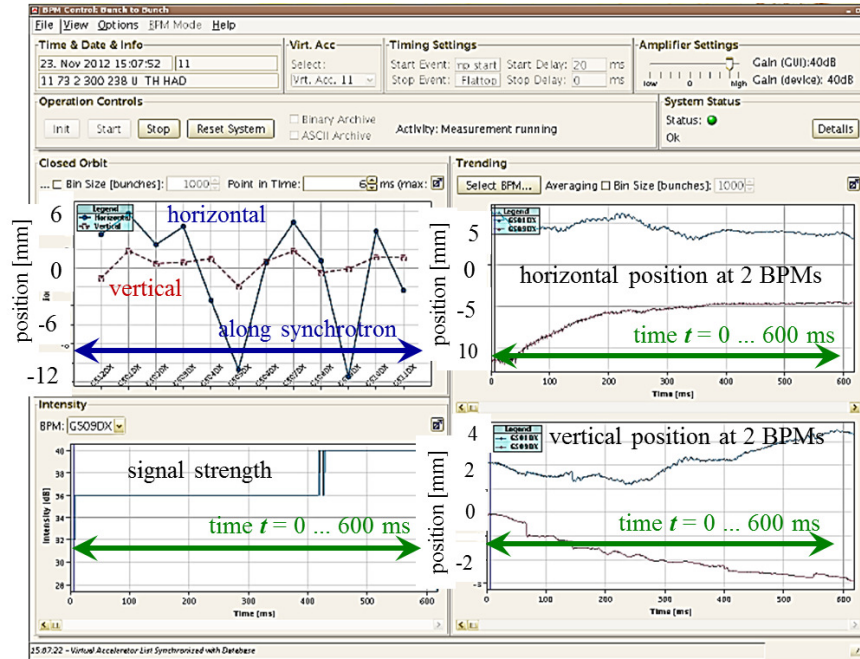


Fig. 96: Position measurement at the GSI synchrotron of a partly misaligned beam during a 0.6 s acceleration. Top left plot: Position around the ring at 12 locations at the beginning of the ramp. Top right plot: Horizontal position during acceleration ramp for two BPM locations. Bottom right plot: Vertical position for these BPMs. Bottom left plot: Signal power $\propto U_S^2$ during ramp for a single BPM. The panel at the top is used to control pre-amplifiers and timing.

7 Measurement of longitudinal parameters

Longitudinal parameters are as important as transverse ones. The longitudinal phase space is spanned by the longitudinal spread and the momentum spread.

- The longitudinal spread of the bunch l is given in units of length (millimetres), time (nanoseconds) or phase (degrees with respect to accelerating frequency), see Fig. 97. The mean value is the centre of the bunch relative to the RF or relative to the ideal reference particle. The corresponding transverse value is the transverse beam profile. For an unbunched d.c. beam, e.g., in a proton storage ring, the quantity has no meaning.
- The momentum spread $\delta = \Delta p/p$ is the deviation relative to the momentum p of the ideal reference particle. Instead of momentum, it is sometimes common in proton or ion linacs and cyclotrons to record the quantity beam energy $\Delta E_{\text{kin}}/E_{\text{kin}}$ or even only ΔE_{kin} . The corresponding transverse value is the beam divergence.

The value of emittance ϵ_{long} is given by the product of the two quantities,

$$\epsilon_{\text{long}} = \frac{1}{\pi} \int_A dl d\delta, \quad (73)$$

where A is the area of the phase space occupied by the beam particles (see Fig. 97). Linear transformations can be applied in the same way as for the transverse case; see Section 5.1. The normalized longitudinal emittance

$$\epsilon_{\text{long}}^{\text{norm}} = \frac{v_s}{c} \gamma_{\text{rel}} \cdot \epsilon_{\text{long}} \quad (74)$$

is preserved under ideal conditions, where v_s is the longitudinal velocity and γ_{rel} is the relativistic Lorentz factor.

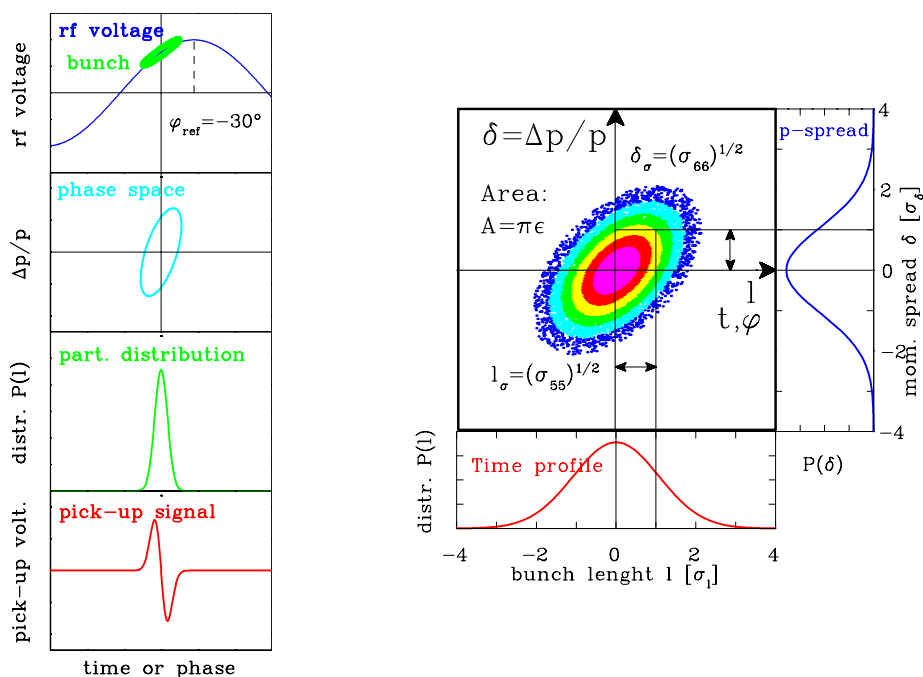


Fig. 97: Left: Relation between accelerating voltage and longitudinal emittance, as well as time distribution of the bunches, as measured with the differentiated pick-up signal. Right: Longitudinal phase space plot of Gaussian distribution.

Using a pick-up or a fast current transformer, the projection of the phase space on the time axis could be determined for some beam parameters, giving the bunch position and width. Determination of the emittance by linear transformation is possible. Some conditions must be fulfilled for a pick-up or transformer to guarantee an adequate bunch shape measurement. Firstly, the signal from the pick-up or transformer must reflect the bunch shape, i.e., the frequency spectrum of the bunch must fit in the bandwidth of the recording electronics; for short bunches, e.g., at high-energy electron accelerators, this might not be the case, see Section 7.7. Secondly, the bunch must be much longer in the longitudinal direction than the pick-up. For bunches with a length comparable to the pick-up, a further condition is that the beam must be sufficiently relativistic that the beam's electric field is essentially transverse. For the transverse electric field component \vec{E}_\perp , Lorentz transformation results in an enhancement in the laboratory frame, compared with the rest-frame of the moving charge, by

$$E_{\perp,\text{lab}}(t_{\text{lab}}) \simeq \gamma \cdot E_{\perp,\text{rest}}(t_{\text{rest}}); \quad (75)$$

see the more detailed discussion in Section 7.1 concerning the transformation of t_{rest} to t_{lab} , which is important for low-energy, non-relativistic particles, e.g., at proton linacs. In the case of a slow beam from a proton linac, the last condition is not fulfilled and other methods must be applied. For bunches shorter than the pick-up, the signal does not reflect the longitudinal bunch shape. For electron beams, the bunch length is so short that the bunch structure is smeared out by integration over the pick-up capacitance, i.e., is expressed in terms of electrical parameters by the limited bandwidth. Here, synchrotron radiation is monitored in connection with the fast optical method using streak cameras, see Section 7.7.

Measurement of the energy or momentum spread $\delta = \Delta p/p$ is not discussed in detail here. A magnetic spectrometer can be used for this purpose, giving point-to-point focus in connection with small slits located at appropriate locations. This is discussed in textbooks on beam optics, e.g., Ref. [137].

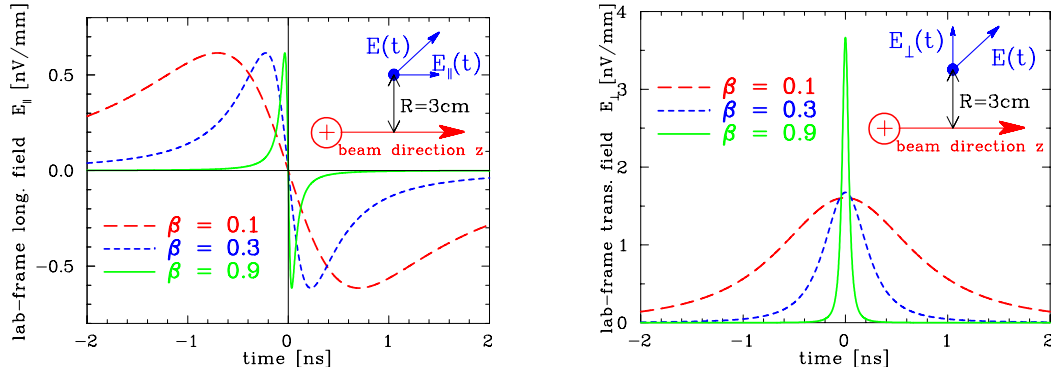


Fig. 98: Effect of advanced electric field at an observation point $R = 30$ mm from the beam axis for different velocities of a point-like charge. Left: longitudinal electric field. Right: Transverse electric field. The closest approach is reached for $t_{\text{rest}} = t_{\text{lab}} = 0$.

7.1 Electric fields of a relativistic charge

Owing to the finite velocity of light, the electric field of a moving charge is modified, as given by the Lorentz transformation. This effect for different velocities β of the moving charge is shown in Fig. 98, which shows the longitudinal electrical field $E_{\parallel}(t)$ in the laboratory frame calculated for a single particle with a charge of e travelling in empty space, according to the time in the laboratory frame, i.e., $t_{\text{lab}} \equiv t$. It is calculated by the relativistic Lorentz boost, including the transformation of the time co-ordinate [18], as

$$E_{\parallel,\text{lab}}(t) = -\frac{e}{4\pi\epsilon_0} \cdot \frac{\gamma\beta ct}{\left[R^2 + (\gamma\beta ct)^2\right]^{3/2}}, \quad (76)$$

where R is the distance of closest approach and

$$\gamma = (1 - \beta^2)^{-1/2}$$

is the relativistic Lorentz factor. The transverse field component E_{\perp} in the laboratory frame is given by

$$E_{\perp,\text{lab}}(t) = \frac{e}{4\pi\epsilon_0} \cdot \frac{\gamma R}{\left[R^2 + (\gamma\beta ct)^2\right]^{3/2}}. \quad (77)$$

These formulae are valid for a free particle and are modified by the boundary condition of the metallic surface, e.g., of the beam pipe or the pick-up plates. A beam bunch consists of many particles distributed within a certain volume; to calculate the accompanying electric field, one must integrate over the bunch volume. For small velocities, the electric field arrives earlier at the pick-up and does not reflect the charge distribution of the bunch; see Section 7.6 for more details.

7.2 Determination of phase position

To match successive linac modules, the right phase relation between accelerating frequency and bunch arrival must be determined using a beam-based measurement. A typical plot is shown in Fig. 99 for a slow MeV/u ion beam recorded by a button pick-up. Owing to the differentiated beam signal, the centre of the bunch is well-determined. There is an arbitrary, but fixed, phase shift between the signal for the pick-up and the accelerating frequency f_{RF} , owing to the different cable lengths. The corresponding quantity concerning the transverse beam position is the centre of mass of a bunch relative to the accelerating RF sine wave.

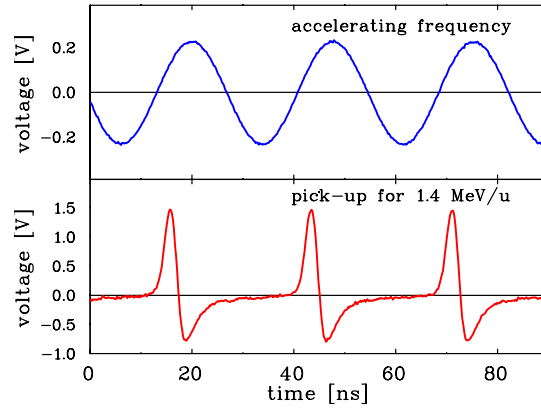


Fig. 99: Top: Linac module accelerating frequency for determination of bunch zero-crossing from a 1.4 MeV/u ion beam. Bottom: Corresponding pick-up signal, recorded using a capacitive pick-up.

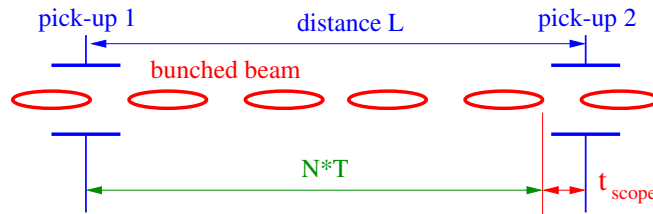


Fig. 100: Principle of time-of-flight measurement using two pick-ups

7.3 Determination of non-relativistic mean energy

The final energy of a linac module is sensitive to the actual setting of the RF amplitude and the phase relative to the preceding modules. Non-relativistic energies can be measured using two pick-ups separated by a distance L and a time-of-flight measurement, see, e.g., Refs. [77, 78, 138]. As displayed in Fig. 100, two pick-ups are installed in a straight section, typically separated by several metres. This distance L must be known precisely, typically to within 1 mm. The centre of mass of the bunch can be read from the oscilloscope, or the correlation function between the two signals can be calculated. A typical measurement is displayed in Fig. 101. As shown in the schematic, there are several bunches between the pick-ups and a coarse estimate of the velocity is needed. This is normally known, but in case of trouble, a third pick-up must be installed much closer to one of the other two. The velocity is calculated for the measured time t_{scope} via

$$\beta c = \frac{L}{NT + t_{\text{scope}}} \quad (78)$$

with N bunches between the pick-ups and a bunch repetition time of $T = 1/f_{\text{RF}}$.

The accuracy of such a velocity measurement $\Delta\beta/\beta$ is given by the uncertainty of the distance ΔL and the scope reading Δt as

$$\frac{\Delta\beta}{\beta} = \sqrt{\left(\frac{\Delta L}{L}\right)^2 + \left(\frac{\Delta t}{NT + t_{\text{scope}}}\right)^2}. \quad (79)$$

An accuracy better than 0.1% for the energy spread $\Delta E_{\text{kin}}/E_{\text{kin}} = 2\Delta\beta/\beta$ can be obtained, assuming an accuracy for the distance of $\Delta L = 1$ mm and for the time measurement of $\Delta t = 100$ ps; the parameters used at the GSI linac are summarized in Table 13.

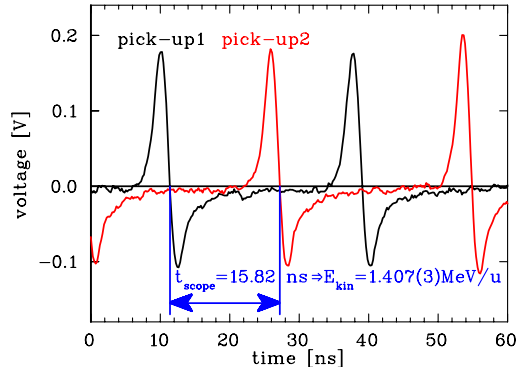


Fig. 101: Time-of-flight signal from two pick-ups with $E_{\text{kin}} \simeq 1.4$ MeV/u at the GSI linac; $f_{\text{RF}} = 36.136$ MHz $\Leftrightarrow T = 1/f_{\text{RF}} = 27.673$ ns. For a distance $L = 1.629$ m between the pick-ups, there are $N = 3$ bunches between the pick-ups. Inserting a time difference $t_{\text{scope}} = 15.82$ ns in Eq. 78, the velocity $\beta = 0.05497(7)$ and corresponding beam energy $E_{\text{kin}} = 1.407(3)$ MeV/u are calculated. The error is given by Eq. 79, inserting uncertainties of $\Delta t = 0.1$ ns and $\Delta L = 1$ mm.

Table 13: Energy resolution for time-of-flight measurement with pick-up distance of 3.25 m for some GSI linac modules (internal linac module names are given). The RF frequency is $f_{\text{RF}} = 36.14$ MHz and the assumed time accuracy is 100 ps.

Physical parameter	Unit	RFQ	IH1	IH2	AL4
Energy, W	MeV/u	0.12	0.75	1.4	11.4
Velocity, β	%	1.6	4.0	5.5	15.5
Total time of flight	ns	677	271	197	70
Bunch spacing, $\beta c/f_{\text{RF}}$	cm	13	33	45	129
Resolution, $\Delta W/W$	%	0.07	0.10	0.12	0.22

The final energy of an ion beam in a linac module depends on the applied amplitude and phase of the accelerating RF. This is depicted in Fig. 102 for an ion beam of 1.400 MeV/u nominal energy. This nominal energy is achieved only in a small interval; for the displayed case, the allowed amplitude range is less than $\pm 2\%$ and the phase should be aligned within $\pm 10^\circ$. This corresponds to a relatively small range; it calls for precise beam alignment and a large accuracy in the time-of-flight measurement, as demonstrated by the small error bars in Fig. 102. Matching the nominal beam energy of a linac module is an important task, because the energy acceptance of the following module is typically restricted within several percent and a sufficient beam transmission through a chain of linac modules is only achieved if all modules produce the correct energy increase. Moreover, the longitudinal emittance depends strongly on the correct RF amplitude and phase setting.

Even though the time-of-flight method is commonly called energy measurement, it is basically a velocity determination. This method cannot be applied for electron beams, because electrons are relativistic after the first linac modules. Acceleration of electrons is related more to an increase in their momentum; therefore, energy determination by the bending of a dipole magnet is more appropriate in this case. Because of the dependence of the bending radius on the particle momentum Δp with respect to a reference particle of momentum p_0 , the momentum distribution is transferred to a distribution in the horizontal plane. This is described by the optical parameter dispersion $D(s)$, as the additional beam offset is $\Delta x(s) = D(s) \cdot \Delta p/p_0$. However, the resulting profile is a mixture of the transverse and longitudinal parameters and transverse collimation is required at the entrance of the optical system, see discussions in textbooks on beam optics, e.g., Ref. [137].

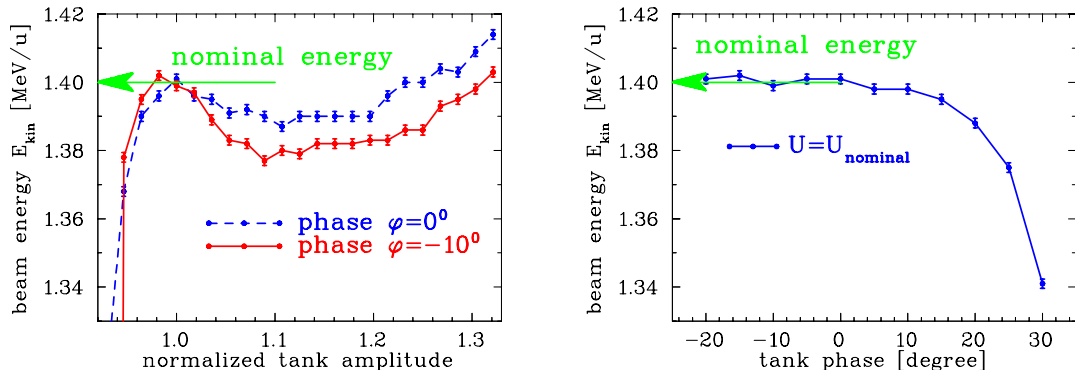


Fig. 102: Left: Output energy of the GSI linac, depicted as a function of the applied RF amplitude inside the tank, as displayed in Fig. 101. Right: Phase for nominal amplitude. The required energy of this module is 1.400 MeV/u. The distance between the pick-ups in this case is $L = 1.97$ m with $N = 4$ bunches between pick-ups.

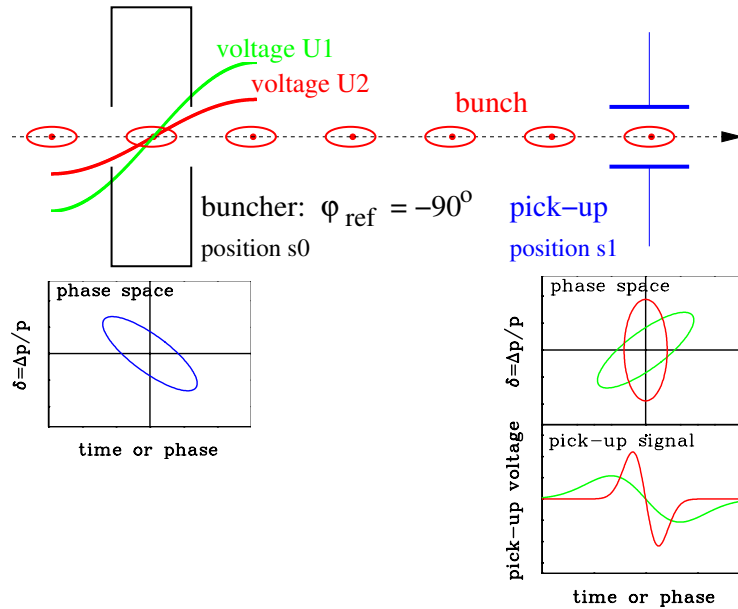


Fig. 103: Longitudinal emittance measurement using a buncher and one bunch shape monitor

7.4 Longitudinal emittance from linear transformation

Longitudinal emittance can be determined from linear transformation, as in the transverse case described in Sections 5.3 and 5.4. The quadrupole variation corresponds to the change in longitudinal focusing performed by a buncher, see Fig. 103. The phase of a buncher is adjusted to 0° , so no acceleration is present. By varying the amplitude, the bunch can be longitudinally focused, i.e., compressed at the measurement location or de-focused, i.e., lengthened. The action is described in the longitudinal sub-space $(l, \delta = \Delta p/p)$, which is a part of the full six-dimensional phase space describing both transverse and longitudinal planes. (The six-dimensional phase space is spanned by the vector $\vec{x}^t = (x, x', y, y', l, \delta)$; the linear behaviour of the accelerator, including the coupling between the horizontal, vertical, and longitudinal degree of freedom, can be described with the help of the 6×6 transport matrices \mathbf{R} . For the formula used here, the bunch length l is given in units of spatial length (metres) to have the same units for all three degrees of freedom.)

The general transfer matrices \mathbf{R} for the transverse and longitudinal phase space have 6×6 elements, as does the beam matrix σ . Disregarding any transverse–longitudinal coupling (e.g., by a dipole

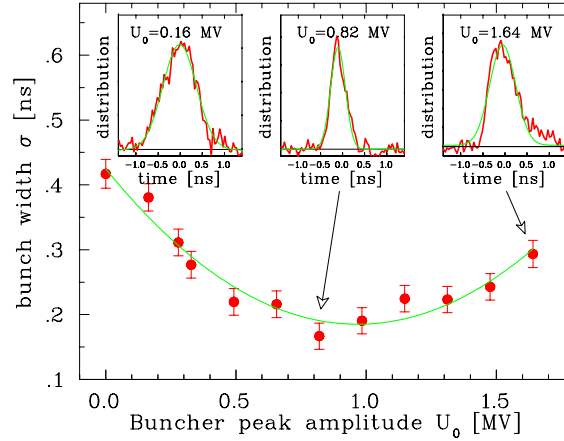


Fig. 104: Measurement of bunch width (one standard deviation) as a function of the buncher voltage 31 m upstream. The bunch shape is not measured by a pick-up, but by a specially designed monitor for low-energy beams [139].

magnet), the longitudinal phase space corresponds to the ‘lower right’ part of the full 6×6 matrices, having the indices 5 and 6. The reduced 2×2 transfer matrix of a buncher, $\mathbf{R}_{\text{buncher}}$, is given in a thin-lens approximation by

$$\mathbf{R}_{\text{buncher}} = \begin{pmatrix} 1 & 0 \\ -1/f & 1 \end{pmatrix}, \quad (80)$$

for the focal length f

$$\frac{1}{f} = \frac{2\pi q U_0 f_{\text{RF}}}{A p v^2} \quad (81)$$

and the voltage amplitude U_0 of the accelerating frequency f_{RF} for a particle of charge q and mass number A with velocity v and momentum p . The transfer matrix for a drift space of length L is given by

$$\mathbf{R}_{\text{drift}} = \begin{pmatrix} 1 & L/\gamma_{\text{rel}}^2 \\ 0 & 1 \end{pmatrix}, \quad (82)$$

where γ_{rel} is the relativistic Lorentz factor. For the transverse case, the emittance can be determined by an amplitude variation U_0 of the buncher, leading to different longitudinal focusing. The bunch length must be measured at the pick-up location s_1 for at least three settings of the buncher. The beam matrix $\sigma(0)$ must be determined at the buncher location s_0 . For bunch width $l_{\text{max}}(1, f_k) = \sqrt{\sigma_{55}(1, f_k)}$ at pick-up location s_1 , a system of linear equations for $\sigma_{ij}(0)$ of the form

$$\begin{aligned} \sigma_{55}(1, f_1) &= R_{55}^2(f_1) \cdot \sigma_{55}(0) + 2R_{55}(f_1)R_{56}(f_1) \cdot \sigma_{56}(0) + R_{56}^2(f_1) \cdot \sigma_{66}(0), & \text{focusing } f_1 \\ \sigma_{55}(1, f_2) &= R_{55}^2(f_2) \cdot \sigma_{55}(0) + 2R_{55}(f_2)R_{56}(f_2) \cdot \sigma_{56}(0) + R_{56}^2(f_2) \cdot \sigma_{66}(0), & \text{focusing } f_2 \\ &\vdots \\ \sigma_{55}(1, f_n) &= R_{55}^2(f_n) \cdot \sigma_{55}(0) + 2R_{55}(f_n)R_{56}(f_n) \cdot \sigma_{56}(0) + R_{56}^2(f_n) \cdot \sigma_{66}(0), & \text{focusing } f_n \end{aligned} \quad (83)$$

is obtained for $k = 1, 2, \dots, n$ measurements with $f_k = f_1, f_2, \dots, f_n$ different settings of the buncher. This redundant system of linear equations must be solved, as discussed in Section 5.3. A measurement is shown in Fig. 104. For the method, it is of no importance which device is used for determination, as long as it reflects the actual bunch shape of the beam.

As discussed for the transverse case, the restrictions are the presence of simple, e.g., Gaussian, phase space distributions, linear beam manipulations, and the lack of non-linear space charge forces.

In addition, one should emphasize that this method is only used at linacs; in most cases, the pick-up resolution is insufficient and special detectors are used, as discussed in Section 7.6 for proton beams and Section 7.7 for electron beams.

A method corresponding to the ‘three-grid method’ for the transverse emittance (Section 5.4), i.e., determination of the bunch shape at several locations, is seldom applied. This is because a special monitor for bunch length determination must be used at proton linac facilities, and, in most cases, is only installed at a few locations.

For beams extracted from a synchrotron, the variation of the bunch length within the beam transfer line is negligible in most cases, owing to the small momentum spread $\Delta p/p$ of the circulating beam and the short flight time t_{drift} to the target of a further synchrotron, as the increase of the bunch length is $\Delta t = \Delta p/p \cdot t_{\text{drift}}$. As an example, the following numbers can be inserted. For a relativistic beam of velocity $\beta \simeq 1$ and a distance of $L = 100$ m from the synchrotron to the target, the drift time $t_{\text{drift}} = L/\beta c = 333$ ns; assuming a momentum spread of $\Delta p/p = 10^{-3}$, the resulting lengthening of the bunch is $\Delta t = \Delta p/p \cdot t_{\text{drift}} = 0.3$ ns, which is shorter than the typical bunch length of $\sigma_{\text{bunch}} > 10$ ns in a proton synchrotron. Therefore, measurement inside the synchrotron is sufficient and the current transformer mounted in the synchrotron can be used for monitoring.

7.5 Longitudinal emittance using tomographic reconstruction

In a proton synchrotron, the bunch length is much longer than the typical size of a pick-up or a current transformer. This enables a true image of the bunch shape to be recorded. Observation and control of the longitudinal behaviour at injection, acceleration, and possibly bunch manipulations, such as combining or splitting of bunches, can be performed.

An innovative analysis method has been developed at CERN [140–142] to determine the longitudinal phase space distribution and hence the emittance from a measurement of the bunch shape on a turn-by-turn basis. The idea is based on the well-known tomographic reconstruction used as an imaging technique in medicine for X-ray tomography and nuclear magnetic resonance tomography and described in textbooks on medical physics.

The underlying principle of tomography is to combine the information from a sufficiently large number of projections to unambiguously construct a more complete picture with the extra dimension reinstated. The application of tomography to longitudinal phase space in an accelerator becomes obvious once it is realized that a bunch of particles performing synchrotron motion is analogous to a patient rotating in a stationary body scanner. On each turn around the machine, a longitudinal pick-up provides a ‘snapshot’ of the bunch projected at a slightly different ‘angle’, i.e., the oscillation of the bunch shape, as given by the inverse of the synchrotron frequency f_{synch} , is, in nearly all cases, much smaller than the revolution frequency $f_{\text{rev}} \gg f_{\text{synch}}$. It suffices to combine such profiles tomographically to obtain a two-dimensional picture of the phase space density. Non-linear emittance growth can also be included [140–142]. A general, well-fulfilled condition is that the synchrotron frequency is much smaller than the revolution frequency. At least half a synchrotron period must be recorded, corresponding to a 180° image of the patient body in the medical application.

The general idea behind tomography is based on algebraic reconstruction techniques (described in textbooks on medical physics), as depicted in Fig. 105 from Refs. [140–142]. The contents of the bins of a one-dimensional histogram are redistributed over the two-dimensional array of cells that comprises the reconstructed image. Assuming no a-priori knowledge of the original two-dimensional distribution, the contents of one bin are spread over all the cells that could have contributed to that bin. The back-projection of all bins of all profiles yields a first approximation of the original distribution. Back-projection of the bin-by-bin difference between the original set of profiles and a new set yields an improved approximation. Further iterations converge more rapidly if any cell whose contents have become negative is reset to zero. A more detailed description is found in Refs. [140–142].

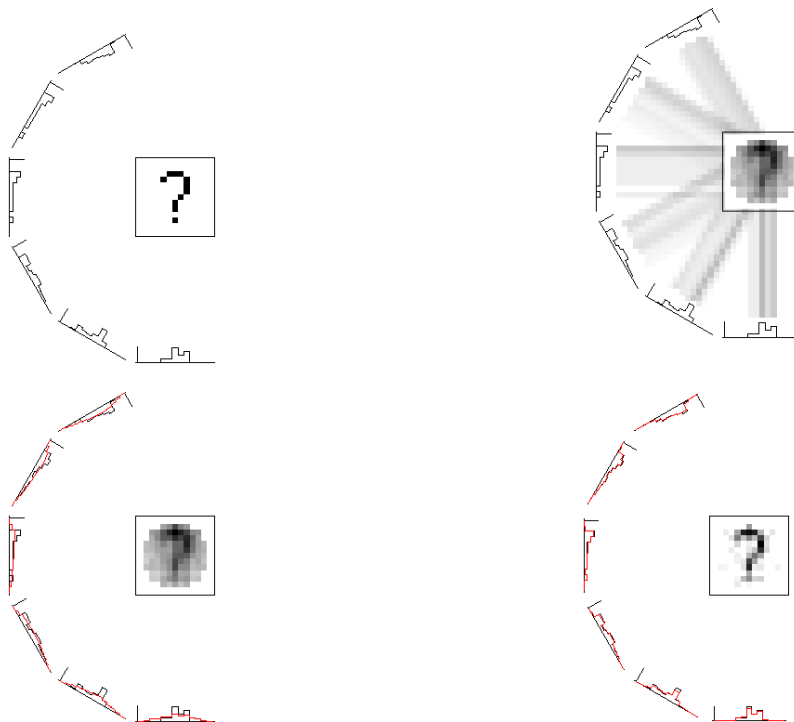


Fig. 105: Schematic plots for tomographic reconstruction [140–142]. Top left: Original two-dimensional image and one-dimensional projections. Top right: First back-projection. Bottom left: First iteration step for the generation of differences in the projected data. Bottom right: After ~ 50 iterations, the original image can be reconstructed.

Two examples demonstrate the analytical power of tomography [142, 143]. The first, illustrated in Fig. 106, is the recording of a standard, constant bunch shape using a digital scope. Reconstruction of the first time slice shows good filling of the bucket. The second, illustrated in Fig. 107, is related to a special bunch manipulation. In phase space (as shown for a small bunch width), the distribution rotates at the synchrotron frequency, resulting in varying bunch shapes as a function of time. This type of short bunch is created to fulfil the demands of the user, who wants to use a short bunch for dedicated experiments. Reconstruction of the beam shape inside the synchrotron gives the advantage of observing the entire creation process of the so-called bunch rotation and enabling correct trigger timing for extraction of the bunch.

7.6 Bunch structure for non-relativistic energies using secondary electrons

For beams of non-relativistic velocities, the electric field of a bunch has a significant longitudinal component, as calculated for Fig. 98. This longitudinal field is seen by the pick-up, leading to a smearing of the signal. The structure of a bunch cannot be monitored with a pick-up, as demonstrated in Fig. 108 for a 1.4 MeV/u ion beam corresponding to $\beta = 5.5\%$. In addition, the required resolution of 1° in phase, or less than 50 ps in time, corresponds to a bandwidth of more than 10 GHz, which is hardly achieved by RF technologies. Other methods must be applied for such a measurement. The result is important for the adjustment of linac modules, including bunchers for injection to subsequent accelerators, and the comparison of measurements and beam dynamics calculations, as, e.g., required during a commissioning phase of a new accelerator. The bunch width and structure enter numerical codes in the same manner as the transverse parameters, e.g., for the estimation of emittance growth by space charge forces. Moreover, as is shown next, a Gaussian distribution is not a good approximation of the bunch structure at these low energies.

MEASUREMENT TECHNIQUES FOR TRANSFER LINES AND BEAM INSTRUMENTATION

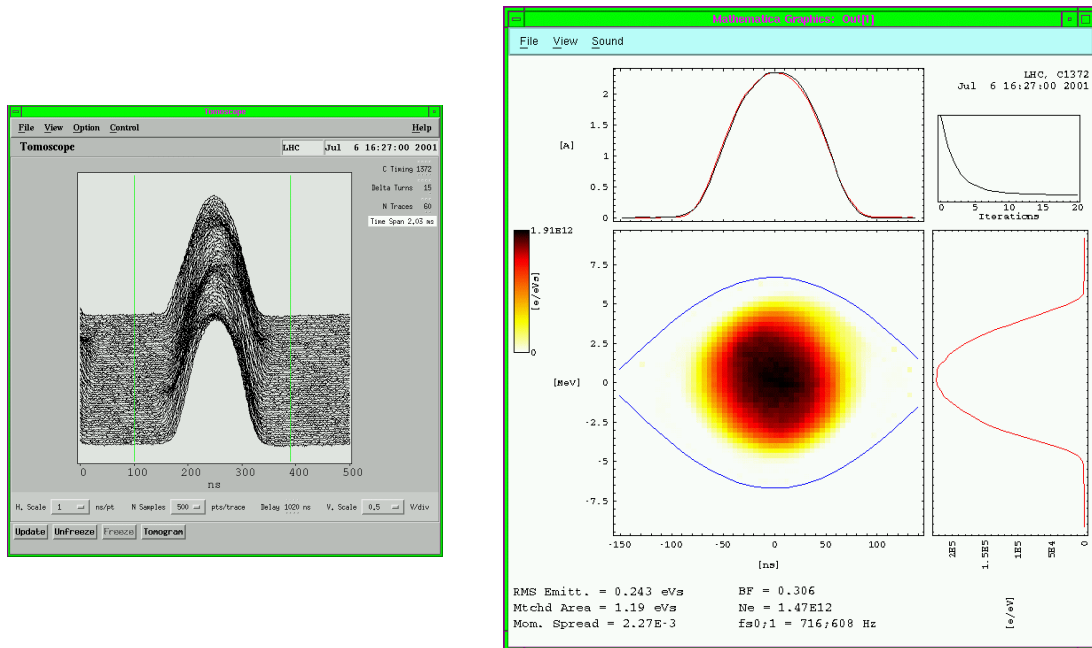


Fig. 106: Left: Bunch shape recorded at CERN PS using a resistive wall current monitor for 500 turns. Right: Reconstructed longitudinal phase space. The bucket size is shown in the phase space and the projections to the time axis (top) and energy (right) are displayed [142, 143].

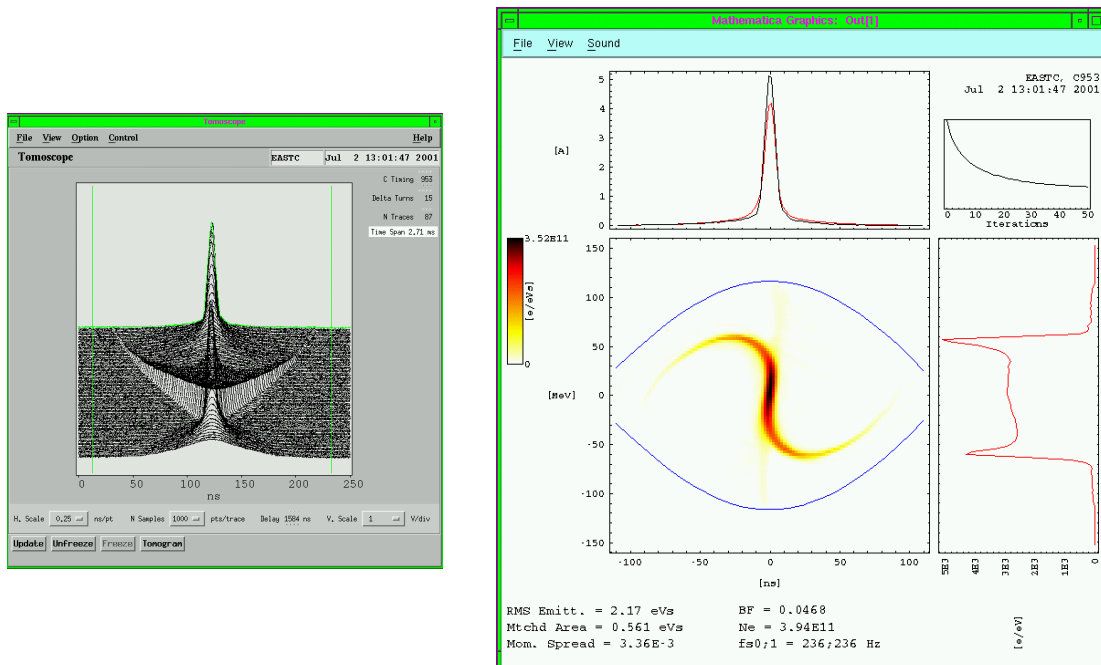


Fig. 107: Figure 106 except for a mismatched bunch. Left: Complex rotation of the bunch width for a specific time slice. Right: Reconstructed phase space density for the same time slice. The filamented distribution rotates to yield varying bunch shapes [142, 143].

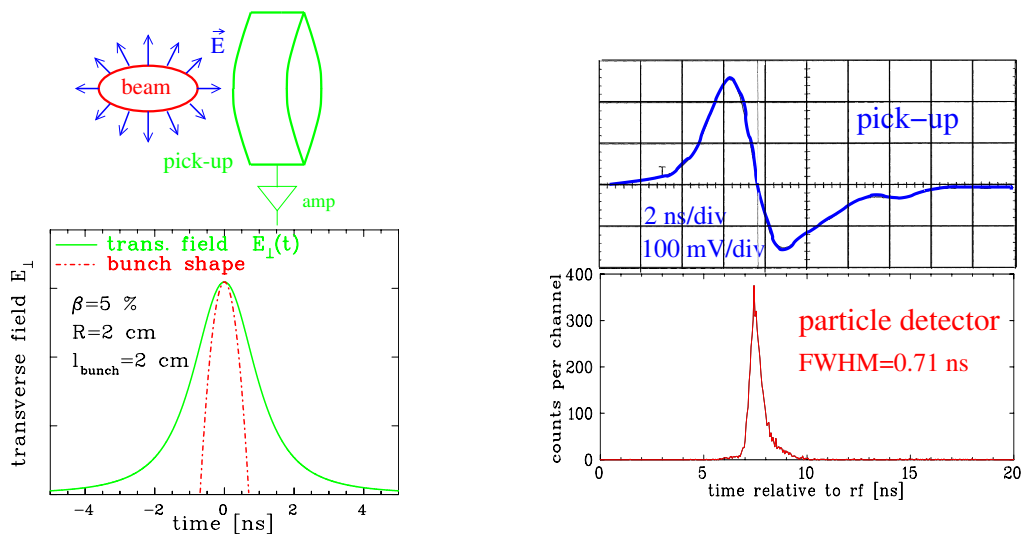


Fig. 108: Left: Simulation of time evolution of transverse electric field, as seen by the pick-up, for a bunch with \cos^2 distribution. Right: Comparison of pick-up signal with bunch structure, as measured using a particle detector at the GSI linac with 1.4 MeV/u. Broadening of the pick-up signal due to the longitudinal field component is clearly visible.

At most low-energy proton or ion linac facilities, a device for bunch structure observation, the so-called bunch structure monitor, is installed, based on the observation of secondary electrons liberated from a single wire intersecting the beam, as shown in Figs. 109 and 110 and reviewed in Refs. [144,145]. The beam hits a wire, which is held at a negative potential of typically -10 kV. The liberated secondary electrons are accelerated by the related electric field towards a thin slit in the side of the vacuum chamber. Here, they pass a pair of plates, across which an RF field with the same frequency as the accelerating RF, or a higher harmonic of it, is applied. This field deflects the electrons; the differences in arrival times are transformed via varying deflection angles to differences in space, i.e., this deflector acts as a ‘time-to-space converter’. (The same principle is used in an analogue oscilloscope.) After a drift of typically 0.5 m, the electrons are detected using a Faraday cup or secondary electron multiplier with a small slit in front. For a fixed slit position, the phase of the deflecting RF relative to the accelerating RF can be changed to transmit electrons representing different time slots of the beam bunches, giving a full image of the bunch structure.

The resolution of this device is better than 1° in phase, independent of the frequency of the RF, up to several hundred megahertz. It is known that the emission of secondary electrons is a fast process, with a time difference of less than 10 ps between the hit of the beam particle and electron emission, i.e., much faster than the required resolution. The RF deflector is built as a resonator to produce an electric field high enough for typically 100 mrad deflection to have an appropriate separation at the detector of ~ 0.5 m. In addition, the electrons must be focused transversally. A constant d.c. voltage applied to the deflector plates serves as an electrostatic lens.

A typical measurement behind a low-energy linac module is shown in Fig. 111, which also acts as an example of the probable non-Gaussian shape typically created in high-current proton or ion linacs. The two measurements for high (top) and low (bottom) currents show quite different bunch shapes. A larger width, corresponding to a filamented phase space distribution, is observed for the low-current case. Particle-tracking calculation for this case confirms the strong ion current dependence of the longitudinal emittance. The applied RF power in the cavity counteracts the space charge force for a high-current beam. For a low current, filamentation occurs as the result of the missing damping by the space charge, which must be corrected by a smaller RF power. This shows that matching of the amplitude and phase for

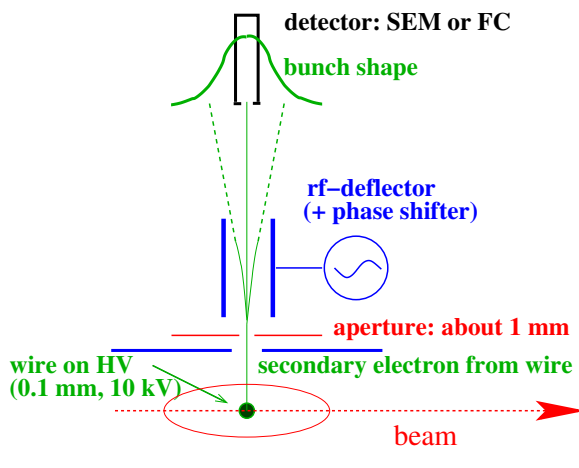


Fig. 109: Principle of deflector technique for bunch structure observation by bunch shape monitor. FC, Faraday cup; HV, high voltage; SEM, secondary electron multiplier.

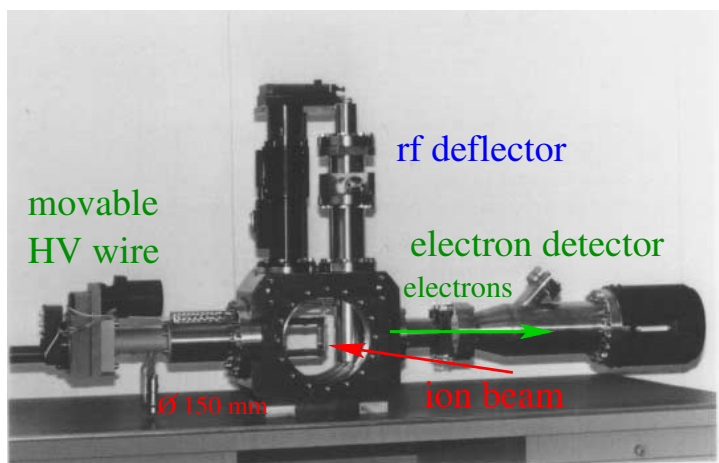


Fig. 110: Bunch structure monitor installed at CERN linac 2 [144, 145]. The vacuum feed-through on the left-hand side is the support for the high-voltage wire. The RF deflector is installed on the vertical flange. The detector is mounted at the right.

a linac cavity is of great influence on the longitudinal beam emittance and must therefore be measured and controlled to preserve beam quality.

7.7 Bunch structure for relativistic electron beams

In most cases, pick-ups are not used for longitudinal diagnostics at electron accelerators, although, owing to the relativistic velocities, this would be possible. However, the bunch length, e.g., at a synchrotron light source, is typically only of the order of several tens of picoseconds, so that even a pick-up bandwidth of several gigahertz is insufficient to reproduce the detailed bunch structure. Here we profit from the emission of synchrotron light at a dipole or, preferably, from an insertion device. A review of this technique is given in Ref. [147].

The principle of such a measurement is shown in Fig. 112. It uses a streak camera as a commercially available device [149], which allows visible light observations with a time resolution down to, typically, 1 ps. Synchrotron light in the optical to ultraviolet wavelength range emitted by the bent elec-

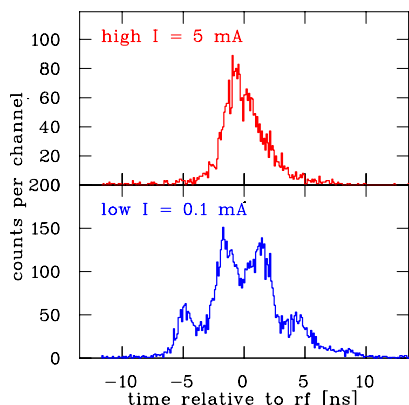


Fig. 111: Bunch structure measured at the GSI linac with a 120 keV/u Ar¹⁺ beam for different currents inside the RFQ [146]; one RF period is shown.

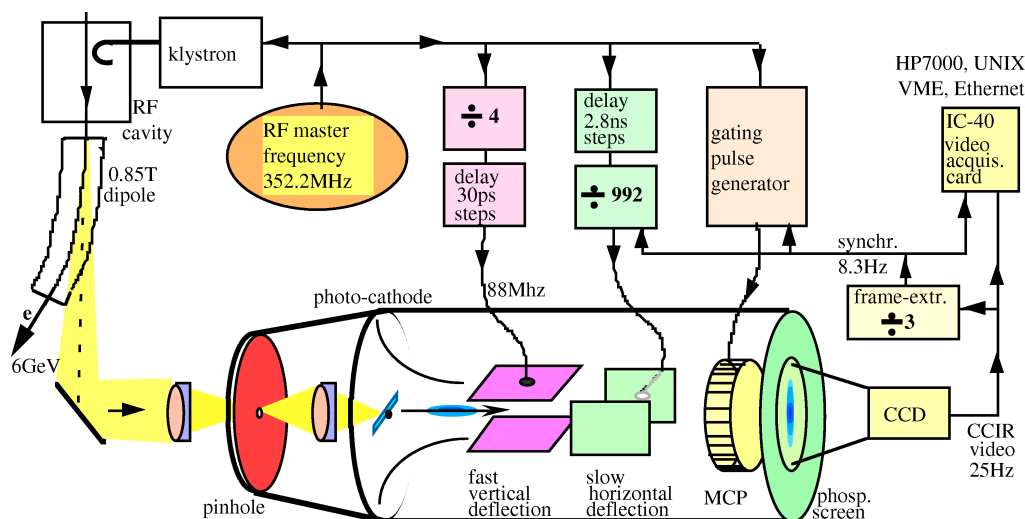


Fig. 112: Principle of streak camera measurement for bunch width determination at ESRF electron accelerator [148].

tron beam is used. It is focused and scraped by a pinhole onto the photocathode of a streak camera. The secondary electrons from the photocathode are accelerated and pass a fast deflector driven by a frequency in the range 50–300 MHz, which is locked to the accelerating frequency for synchronization. The general scheme is similar to the ‘time-to-space converter’ discussed in Section 7.6. After a certain drift space, the electrons are amplified by a multichannel plate and converted to photons by a phosphor screen. The image from the phosphor is captured using a standard CCD camera. The different arrival times of the synchrotron light, and therefore the bunch structure, are converted to differences in space, with a typical full scale of several 100 ps and a resolution in the picosecond range. A second, perpendicular, pair of plates is driven at a much lower frequency to separate the images from the individual bunches.

An example of a bunch length measurement, as collected using synchrotron radiation from a dipole, is depicted in Fig. 113 [150]. The slow scan for the separation of the individual bunches is displayed along the horizontal axis. The vertical axis has a full scale of 360 ps; the bunch width is only $\sigma \simeq 40$ ps, demonstrating the high resolution of such a system. Short bunches are needed by synchrotron radiation users for time-resolved spectroscopy. A large voltage is applied to the synchrotron RF cavities to produce and maintain these short bunches. In Fig. 114, the bunch width is plotted for different RF voltages. As displayed, the achievable bunch length depends on the stored electron current. Counter-

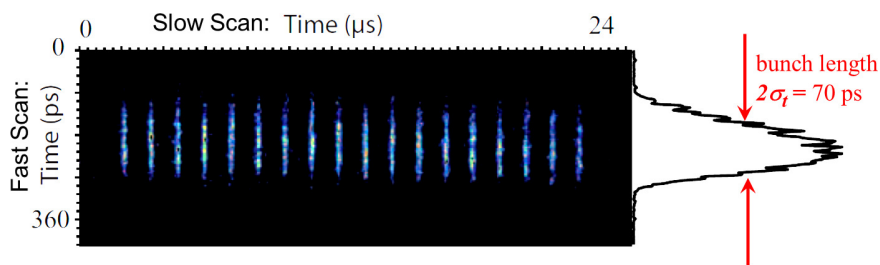


Fig. 113: Bunch length measurement with a streak camera, using synchrotron light from individual bunches emitted by passage through a dipole at SOLEIL [150]. The horizontal axis scaling is 24 μs full scale for the bunch repetition (slow scan direction); the vertical axis is 360 ps full scale for the bunch structure (fast scan direction).

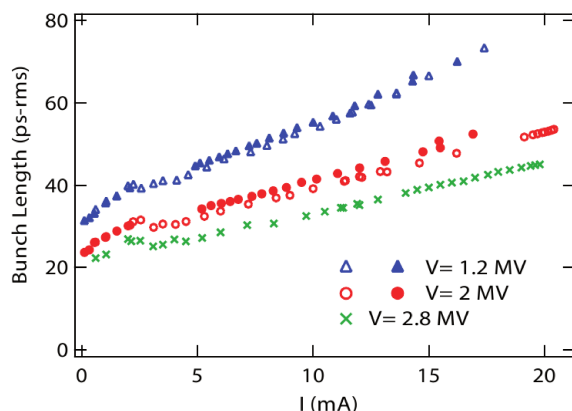


Fig. 114: Example of the use of a streak camera at the SOLEIL synchrotron light facility achieved from measurements like the one depicted in Fig. 113. For different accelerating voltages, the bunch length is recorded as a function of the beam current stored in the synchrotron [150].

acting the RF bunching force, the incidence of non-linear processes, such as wakefields and instabilities, increases for higher currents. Such effects as head–tail oscillations or longitudinal bunch oscillation due to coupled bunch instabilities are also made visible with the help of streak camera measurements; see, e.g., Ref. [147].

The longitudinal properties of the bunch injected to the storage ring from the booster ring of a synchrotron light facility can be monitored using a streak camera to enable adequate correction. The results of such a measurement, made at ALS (Berkeley) [151, 152], for injection into an empty storage ring, are depicted in Fig. 115, with injection energy $E_{\text{kin}} = 1.5$ GeV, revolution time $t_{\text{rev}} = 656$ ns, accelerating frequency $f_{\text{acc}} = 499.7$ MHz and, for the chosen RF amplitude, synchrotron frequency $f_{\text{synch}} = 11.4$ kHz, corresponding to a synchrotron tune $Q_{\text{synch}} = t_{\text{rev}} \cdot f_{\text{synch}} = 0.0075$, i.e., a longitudinal repetition of the oscillations every $n = 1/Q_{\text{synch}} = 133$ turns. The longitudinal damping time is about 10 ms, i.e., much longer than the depicted observation. In the first displayed case, a single bunch is injected with a phase error, i.e., the bunch centre does not pass the RF cavity during the zero-crossing of the sine wave. The particles execute coherent synchrotron oscillations, which correspond to a rotation in the longitudinal phase space that is measurable via a variation of the bunch centre. The projection along the time axis of the bunch distribution is a function of the longitudinal forces; this is measured as a variation in bunch length. The same movement occurs when the bunch is injected with an incorrect energy, except that a phase change of the synchrotron oscillation of 90° is visible for the bunch central position (middle part of Fig. 115). The remedy for these mismatches is a proper adjustment of the RF phase relation between the booster and the storage ring in the first case and a realignment of the storage ring energy in the second case. This is important to prevent emittance enlargement by filamentation in

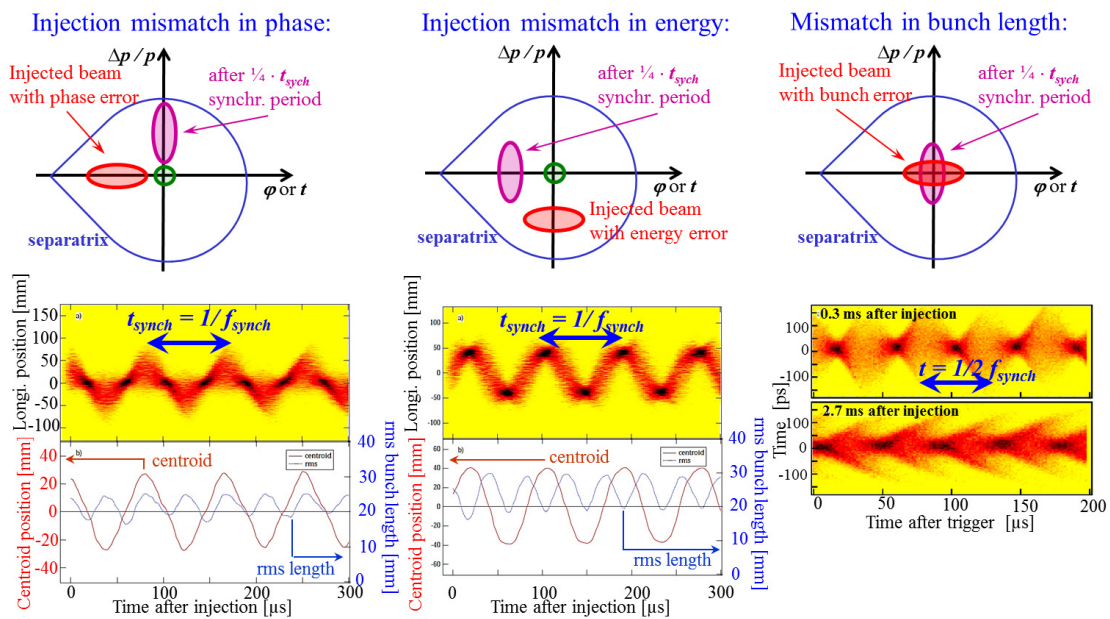


Fig. 115: Measurement of longitudinal injection mismatch at the ALS light source. Top: Schemes of injection mismatch in phase, energy, and bunch length. Bottom: Bunch observation using streak camera with evaluated bunch centre and width for each case. Data and plots are from Refs. [151, 152].

phase space for long storage times, which is not completely compensated by longitudinal damping and influences the circulating beam properties if a top-up injection scheme is used. The right-hand panel of Fig. 115 shows the case of an injection with correct phase and energy but unmatched bunch length. The synchrotron movement leads to variation of the symmetrical bunch distribution except with double frequency, $2 \cdot f_{\text{synch}}$. After some storage time, the bunch shape changes, owing to non-linear forces created by the RF wave, leading to filamentation in phase space, as shown for the observations at 0.3 ms and 2.7 ms after injection. More details on this instructive example, as well as a comparison with simulations, are given in Refs. [151, 152]. A streak camera is used to monitor the short bunches present at a synchrotron light facility, in the display case of $\sigma_{\text{bunch}} = 30\text{--}100$ ps. For a hadron synchrotron with a bunch length of typically $\sigma_{\text{bunch}} = 1\text{--}100$ ns, a comparable behaviour could be observed using a fast current transformer.

8 Conclusion

The functionality of various beam monitoring instruments has been described and the applicability for different beam parameters has been discussed. For regular operation of a transfer line, current, transverse profile, and beam position measurements are mainly used for possible manual or automated beam alignment. It is an advantage if the measurement is non-destructive for the beam, as this enables simultaneous measurement at several locations. This is, e.g., realized by current transformers, if the beam parameters allow for their usage. For smaller currents, e.g., for beams extracted slowly from a synchrotron, destructive detectors must be used; these are based on the energy loss of the particles in a gas or metal. For profile measurements, various techniques are applied; scintillation and optical transition radiation screens are favoured techniques for regular operation, owing to their reproduction of the two-dimensional distribution. Both SEM grids and wire scanners are also often used, owing to their robustness and large dynamic range. For bunched beams, the transverse centre position can be recorded using BPMs, which serve as the most frequently used signal source for beam alignment. Owing to their principle, BPMs are non-destructive but require a minimum beam current and are not suited for unbunched beams, e.g.,

for slow extraction. At transport lines behind a linac or a cyclotron, more complex parameters must be determined, in particular, transverse and longitudinal emittances. The related measurements are, in many cases, made by experts during dedicated machine development times; this allows for more complex instruments and methods. Alignment in the injection process involves using beam instrumentation installed in the synchrotron. An example is the control of proper timing by observing the beam current and its time structure, in the transfer line and the stored beam, using current transformers. A further example is the observation of transverse or longitudinal profiles and their evolution during storage. The long observation time during storage enables precise determination of several beam parameters and the control of such injection settings as steering, focusing by transfer line magnets and the timing properties of the injection devices. The beam's parameters are also determined prior to extraction of a beam from a synchrotron. In many facilities, beam loss monitors are installed to ensure correct accelerator functionality on an online basis; an interlock is generated if there is any malfunction. Owing to their sensitivity, beam loss monitors can also be used to optimize beam transmission during regular operation, serving as an alternative to current transformers.

Acknowledgements

Valuable discussions with A. Reiter and R. Singh from GSI, Darmstadt, and M. Schuh from KIT, Karlsruhe, as well as the careful review of the paper by S. Mirza from GSI, are warmly acknowledged.

References

- [1] V. Smaluk, *Particle Beam Diagnostics for Accelerators: Instruments and Methods* (VDM Verlag Dr. Müller, Saarbrücken, 2009).
- [2] Beam diagnostics for accelerators, in Proceedings of the CAS-CERN Accelerator School: Course on Beam Diagnostics, Dourdan, France, 28 May-6 Jun 2008, edited by D. Brandt, CERN-2009-005, (CERN, Geneva, 2009), <https://doi.org/10.5170/CERN-2009-005>.
- [3] P. Strehl, *Beam Instrumentation and Diagnostics* (Springer Verlag, Berlin, 2006).
- [4] M.G. Minty and F. Zimmermann, *Measurement and Control of Charged Particle Beams* (Springer Verlag, Berlin, 2003).
- [5] S-I. Kurokawa *et al.* (Eds.), Proc. School on Beam Measurement, Proceeding Montreux (World Scientific, Singapore, 1999).
- [6] J.M. Month and S. Turner (Eds.), *Frontiers in Particle Beams; Observation, Diagnosis and Correction* (Springer Verlag, Berlin, 1988).
- [7] P. Forck *JUAS Lecture Notes on Beam Instrumentation and Diagnostics*, www.gsi.de/work/gesamtprojektleitung_fair/commons/beam_instrumentation/research_and_development_lobird/veroeffentlichungen.htm
- [8] D. Lipka *et al.*, Proc. IBIC 16, Barcelona, 2016, p. 14.
- [9] V. Schlott *et al.*, Proc. IBIC 15, Melbourne, 2015, p. 12.
- [10] H. Loos, Proc. IBIC 14, Monterey, 2014, p. 475.
- [11] www.bergoz.com
- [12] D. Belohrad, Proc. DIPAC 11, Hamburg, 2011, p. 564.
- [13] H. Reeg, Proc. DIPAC 01, Grenoble, 2001, p. 120.
- [14] R.C. Webber, Proc. BIW 94, Vancouver, 1994, p. 3.
- [15] K. Unser, *IEEE Trans. Nucl. Sci.* **NS-28** (1981) 2344, <https://doi.org/10.1109/TNS.1981.4331686>.
- [16] W.R. Leo, *Techniques for Nuclear and Particle Physics Experiments: A How-to Approach* (Springer Verlag, Berlin, 1994).
- [17] G.F. Knoll, *Radiation Detection and Measurement* (John Wiley, New York, 1999).

- [18] J.D. Jackson, *Classical Electrodynamics* (John Wiley & Sons, New York, 1998).
- [19] F. Ziegler *et al.* *The Stopping and Range of Ions in Solids (Stopping and Range of Ions in Matter, vol. 1)* (Pergamon Press, New York, 1985).
- [20] www.SRIM.org
- [21] lise.nsl.msui.edu/lise.html
- [22] <http://physics.nist.gov/PhysRefData/Star/Text/ESTAR.html>
- [23] A.F.D. Morgan, Proc. DIPAC 05, Lyon, 2005, p. 51.
- [24] E.J. Sternglass, *Phys. Rev.* **108** (1957) 1, <https://doi.org/10.1103/PhysRev.108.1>.
- [25] C.G. Drexler and R.D. DuBois, *Phys. Rev.* **A53** (1996) 1630, <https://doi.org/10.1103/PhysRevA.53.1630>.
- [26] P. Finocchiaro *et al.*, Proc. DIPAC 97, Frascati, 1997, p. 53.
- [27] P. Forck *et al.*, Proc. DIPAC 97, Frascati, 1997, p. 165.
- [28] P. Forck *et al.*, Proc. BIW 96, Argonne, 1996, p. 422.
- [29] P. Lecoq *et al.*, *Inorganic Scintillators for Detector Systems* (Springer Verlag, Berlin, 2006).
- [30] F. Sauli, Principle of operation of multiwire proportional and drift chambers, CERN-77-09 (CERN, Geneva, 1977), <https://doi.org/10.5170/CERN-1977-009>.
- [31] H. Reeg, Proc. DIPAC 99, Chester, 1999, p. 141.
- [32] C. Schömers *et al.*, *Nucl. Instrum Methods Phys. Res.* **A795** (2015) 92, <https://doi.org/10.1016/j.nima.2015.05.054>.
- [33] C. Schömers *et al.*, Proc. IPAC 11, San Sebastian, 2011, p. 2851.
- [34] C. Schömers *et al.*, Proc. IPAC 13, Shanghai, 2013, p. 2944.
- [35] G. Ferioli and R. Jung, Proc. DIPAC 97, Frascati, 1997, p. 168.
- [36] K. Wittenburg, Proc. EPAC 02, Paris, 2002, p. 109.
- [37] K. Wittenburg, in Proceedings of the CAS-CERN Accelerator School: Course on Beam Diagnostics, Dourdan, France, 28 May-6 Jun 2008, edited by D. Brandt, CERN-2009-005, (CERN, Geneva, 2009), pp. 249-280, <https://doi.org/10.5170/CERN-2009-005.249>.
- [38] A. Zhukov, Proc. BIW 10, Santa Fe, 2010, p. 553.
- [39] R.E. Shafer, Proc. BIW 02, Brookhaven AIP 648, 2002, p. 44.
- [40] A.H. Sullivan, *A Guide to Radiation and Radioactivity Level Near High Energy Particle Accelerators* (Nuclear Technology Publishing, Ashford, 1992).
- [41] S. Roesler *et al.*, in *Handbook of Acceleration Physics and Engineering*, Eds. A.W. Chao *et al.* (World Scientific, Singapore, 2013), p. 767.
- [42] P. Forck and T. Hoffmann, Proc. DIPAC 01, Grenoble, 2001, p. 129.
- [43] D. Kramer *et al.*, Proc. DIPAC 07, Venice, 2007, p. 313.
- [44] D. Kramer, Ph.D. thesis, Technical University of Liberec, 2008.
- [45] R.E. Shafer *et al.*, Proc. Intern. Conf. High Energy Acc., Batavia, 1983, p. 609.
- [46] D. Gassner *et al.*, Proc. BIW 00, Cambridge, 2000, p. 392.
- [47] B. Dehning, Proc. DIPAC 05, Lyon, 2005, p. 117.
- [48] E.B. Holzer *et al.*, Proc. EPAC 08, Genoa, 2008, p. 1134.
- [49] M. Stockner *et al.*, Proc. DIPAC 07, Venice, 2007, p. 328.
- [50] <http://wwwinfo.cern.ch/asd/geant4/>
- [51] A. Zhukov, Proc. PAC 13, Pasadena, 2013, p. 714.
- [52] R. Jung *et al.* Proc. DIPAC 03, Mainz, 2003, p. 28.
- [53] R. Jung, Proc. DIPAC 93, Montreux, 1993, p. 4.
- [54] B. Walasek-Höhne *et al.*, Proc. DIPAC 11, Hamburg, 2011, <http://www->

- bd.gsi.de/ssabd/index.html
- [55] E. Gütlich *et al.*, Proc. BIW 08, Lake Tahoe, 2008.
 - [56] E. Gütlich *et al.*, Proc. DIPAC 11, Hamburg, 2011, p. 179.
 - [57] G. Kube *et al.*, Proc. PAC 12, New Orleans, 2012, p. 2119.
 - [58] U. Iriso *et al.*, Proc. DIPAC 09, Basel, 2009, p. 200.
 - [59] R. Ischebeck *et al.*, Proc. IBIC 14, Monterey, 2014, p. 259.
 - [60] R. Ischebeck *et al.*, *Phys. Rev. S.T. Accel. Beams* **18** (2015) 082802, <https://doi.org/10.1103/PhysRevSTAB.18.082802>.
 - [61] T.J. Shea *et al.*, Proc. PAC 97, Vancouver, 1997, p. 2215.
 - [62] P. Forck *et al.*, Proc. IPAC 14, Dresden, 2014, p. 3482.
 - [63] A. Lieberwirth *et al.*, *Nucl. Instrum. Methods Phys. Res.* **B365** (2015) 533. <https://doi.org/10.1016/j.nimb.2015.07.111>
 - [64] P. Forck *et al.*, Proc. DIPAC 11, Hamburg, 2011, p. 170.
 - [65] R. Haseitl *et al.*, Proc. PCaPAC 2008, Ljubljana, 2008, p. 180.
 - [66] M. Plum, Proc. BIW 04, Knoxville, 2004, p. 23.
 - [67] S. Burger *et al.*, Proc. DIPAC 03, Mainz, 2003, p. 122.
 - [68] C. Fischer *et al.*, Proc. EPAC08, Rome, 1988, p. 1081.
 - [69] U. Raich, Proc. DIPAC 05, Lyon, 2005, p. 1.
 - [70] R.J. Colchester and R. Jung, Proc. PAC 97, Vancouver, 1985, p.1917.
 - [71] C. Field, *Nucl. Instrum. Methods Phys. Res.* **A360** (1995) 467, [https://doi.org/10.1016/0168-9002\(95\)00077-1](https://doi.org/10.1016/0168-9002(95)00077-1).
 - [72] M. Matoba *et al.*, *IEEE Trans. Nucl. Sci.* **NS-32** (1985) 541, <https://doi.org/10.1109/TNS.1985.4336890>.
 - [73] P. Forck, Proc. IPAC 10, Kyoto, 2010, p. 1261.
 - [74] P. Forck *et al.*, Proc. DIPAC 05, Lyon, 2005, p. 221.
 - [75] T. Giacomini *et al.*, Proc. BIW 04, Knoxville, 2004, p. 286.
 - [76] T. Giacomini *et al.*, Proc. DIPAC 05, Lyon, 2005, p. 150.
 - [77] P. Forck and P. Strehl, Proc. DIPAC 99, Chester, 1999, p. 42.
 - [78] P. Forck *et al.*, Proc. BIW 00, Cambridge AIP 546, 2000, p. 606.
 - [79] R. Connolly *et al.*, Proc. BIW 00, Cambridge AIP 546, 2000, p. 330.
 - [80] G. Ferioli *et al.*, Proc. DIPAC 01, Grenoble, 2001, p. 201.
 - [81] M. Benedikt *et al.*, Proc. DIPAC 01, Grenoble, 2001, p. 189.
 - [82] C. Bovet *et al.*, Proc. EPAC 98, Stockholm, 1998, p. 1488.
 - [83] K. Satou *et al.*, Proc. High Brightness Hadron Beam Conf. HB 10, Morschach, 2010, p. 506.
 - [84] K. Satou *et al.*, Proc. EPAC 08, Genoa, 2008, p. 1275.
 - [85] T. Schottmann, Thesis DESY HERA 93-09, 1993.
 - [86] K. Satou, Proc. IBIC 17, Grand Rapids, 2017.
 - [87] D. Vilsmeier *et al.*, Proc. IBIC 17, Grand Rapids, 2017.
 - [88] M. Sapinski *et al.*, Proc. IBIC 16, 2016, p. 520.
 - [89] A. Allisy (Ed.), Secondary electron spectra from charged particle interaction, International Commission on Radiation Units and Measurement Report No. 55 (1996).
 - [90] L. Wartski *et al.*, *J. Appl. Phys.* **46** (1975) 3644, <https://doi.org/10.1063/1.322092>.
 - [91] J. Bossert *et al.*, *Nucl. Instrum. Methods Phys. Res.* **A 238** (1985) 45, [https://doi.org/10.1016/0168-9002\(85\)91025-3](https://doi.org/10.1016/0168-9002(85)91025-3).

- [92] C. Bovet *et al.*, Proc. DIPAC 99, Chester, 1999, p. 90.
- [93] V.E. Scarpine *et al.*, Proc. PAC 07, Albuquerque, 2007, p. 2639.
- [94] G. Kube, Proc. DIPAC 07, Venice, 2007, p. 6.
- [95] M. Wilke, Proc. BIW 94, Vancouver, 1994, p. 128.
- [96] C. Bovet *et al.*, Proc. PAC 91, San Francisco, 1991, p. 1160.
- [97] B.X. Yang *et al.*, Proc. PAC 97, Vancouver, 1997, p. 2215.
- [98] B.K. Scheidt, Proc. DIPAC 05, Lyon, 2005, p. 24.
- [99] M. Pont *et al.*, Proc. IPAC 11, San Sebastian, 2011, p. 3023.
- [100] G. Benedetti *et al.*, Proc. IPAC 11, San Sebastian, 2011, p. 2059.
- [101] T. Mitsuhashi, Beam size measurement by use of SR interferometers, Proc. School on Beam Measurement, Montreux, p. 399 (World Scientific, Singapore, 1999).
- [102] T. Mitsuhashi, Proc. BIW 04, Knoxville, 2004, p. 3.
- [103] J.M. Stockli, Proc. BIW 06, Batavia, 2006, p. 25.
- [104] M. Reiser, *Theory and Design of Charged Particle Beams* (J. Wiley Publishing, New York, 1994).
- [105] K.T. McDonald and D.P. Russell, in *Frontiers of Particle Beams; Observation, Diagnosis and Correction*, Eds. M. Month and S. Turner (Springer Verlag, Berlin, 1988), p. 122.
- [106] G. Riehl *et al.*, Proc. DIPAC 95, Travemünde, DESY M9507, 1995, p. 6.
- [107] G. Penco *et al.*, Proc. EPAC 08, Genoa, 2008, p. 1236.
- [108] M.E. Schulze *et al.*, Proc. LINAC 00, Monterey, 2000, p. 575.
- [109] V.A. Dimov *et al.*, Proc. High Brightness Hadron Beam Conf. HB 16, Malmö, 2016, p. 433.
- [110] R.E. Shafer, Proc. BIW 89, Upton, 1989, p. 26, www.bergoz.com/en/mx-bpmf.
- [111] S.R. Smith, Proc. BIW 96, Argonne AIP 390, 1996, p. 50.
- [112] P. Forck, in Proceedings of the CAS-CERN Accelerator School: Course on Beam Diagnostics, Dourdan, France, 28 May-6 Jun 2008, edited by D. Brandt, CERN-2009-005, (CERN, Geneva, 2009), pp. 187-228, <https://doi.org/10.5170/CERN-2009-005.187>.
- [113] M. Wendt, Proc. DIPAC 11, Hamburg, 2011, p. 18.
- [114] G. Kube and M. Werner, Proc. DIPAC 07, Venice, 2007, p. 105.
- [115] B.G. Pine, CARE-ABI Workshop, Lüneburg, 2006, adweb.desy.de/mdi/CARE/Lueneburg/ABI-Lueneburg.htm.
- [116] R.E. Shafer, Proc. BIW 93, Santa Fe, 1993, p. 303.
- [117] C. Simon *et al.*, Proc. IBIC 14, Monterey, 2014, p. 303.
- [118] M. Almaki *et al.*, Proc. IBIC 14, Barcelona, 2016, p. 319.
- [119] C. Boccard, CARE-ABI Workshop, Lüneburg, 2006, adweb.desy.de/mdi/CARE/Lueneburg/ABI-Lueneburg.htm.
- [120] E. Calvo-Giraldo *et al.*, Proc. DIPAC 03, Mainz, 2003, p. 187.
- [121] P. Kowina *et al.*, Proc. DIPAC 05, Lyon, 2005, p. 114.
- [122] R. Lorenz, Proc. BIW 98, Stanford AIP 451, 1998, p. 53.
- [123] G. Vismara, Proc. BIW 00, Cambridge AIP 546, 2000, p. 36.
- [124] G. Vismara, Proc. DIPAC 99, Chester, 1999, p. 11.
- [125] M. Wendt, Proc. IBIC 14, Monterey, 2014, p. 468.
- [126] R. Garoby, Low level RF building blocks, CERN Acc. School, CERN 93-03, 1992, p. 428.
- [127] www.i-tech.si
- [128] J.M. Belleman, Proc. DIPAC 05, Lyon, 2005, p. 137.
- [129] J. Belleman, in Proceedings of the CAS-CERN Accelerator School: Course on Beam Diagnostics,

- Dourdan, France, 28 May-6 Jun 2008, edited by D. Brandt, CERN-2009-005, (CERN, Geneva, 2009), pp. 281-316, <https://doi.org/10.5170/CERN-2009-005.281>.
- [130] V. Schlott *et al.*, Proc. EPAC 00, Vienna, 2000, p. 1809.
- [131] R. Jones, Proc. BIW 10, Santa Fe, 2010, p. 22.
- [132] J.D. Fox and E. Kikuzani, Bunch feedback system and signal processing, Proc. School on Beam Measurement, Montreux (World Scientific Singapore, 1999), p. 579.
- [133] R. Steinhagen, in Proceedings of the CAS-CERN Accelerator School: Course on Beam Diagnostics, Dourdan, France, 28 May-6 Jun 2008, edited by D. Brandt, CERN-2009-005, (CERN, Geneva, 2009), pp. 317-360, <https://doi.org/10.5170/CERN-2009-005.317>.
- [134] J. Wenninger, in Proceedings of the CAS-CERN Accelerator School: Course on Beam Diagnostics, Dourdan, France, 28 May-6 Jun 2008, edited by D. Brandt, CERN-2009-005, (CERN, Geneva, 2009), pp. 361-376, <https://doi.org/10.5170/CERN-2009-005.361>.
- [135] K. Fuchsberger *et al.*, Proc. IPAC 10, Kyoto, 2010, p. 462.
- [136] M. Meddahi *et al.*, Proc. IPAC 10, Kyoto, 2010, p. 1680.
- [137] H. Wollnik, *Optics of Charged Particles* (Academic Press, Orlando, 1987).
- [138] J.C. Dooling *et al.*, Proc. LINAC 00, Monterey, 2000, p. 193.
- [139] P. Forck *et al.*, Proc. DIPAC 05, Lyon, 2005, p. 48.
- [140] S. Hancock *et al.*, *Phys. Rev. Special Topics Accel. Beams* **3** (2000) 124202, <https://doi.org/10.1103/PhysRevSTAB.3.124202>.
- [141] CERN-PS-2000-068-OP (CERN, Geneva, 2000).
- [142] <http://cern.ch/tomography>
- [143] S. Hancock *et al.*, CERN PS/RF Note 2001-010 (CERN, Geneva, 2001).
- [144] A. Feschenko, Proc. PAC 01, Chicago, 2001, p. 517.
- [145] A. Feschenko, Proc. RuPAC 12, Saint Petersburg, 2012, p. 181.
- [146] P. Forck *et al.*, Proc. LINAC 00, Monterey, 2000, p. 166.
- [147] K. Scheidt, Proc. EPAC 00, Vienna, 2000, p. 182.
- [148] K. Scheidt, Proc. EPAC 96, Sitges, 1996, p. 1624.
- [149] www.hamamatsu.com
- [150] M. Labat *et al.*, Proc. DIPAC 07, Venice, 2007, p. 241.
- [151] J.M. Byrd *et al.*, Proc. PAC 99, New York, 1999, p. 382.
- [152] J.M. Byrd and S. De Santis, Longitudinal injection transients in an electron storage ring, 2001, <http://escholarship.org/uc/item/8k6677nw>.